

VRIJE UNIVERSITEIT

Implementation, Calculation and Interpretation of Vibrational Circular Dichroism Spectra

ACADEMISCH PROEFSCHRIFT

ter verkrijging van de graad Doctor aan
de Vrije Universiteit Amsterdam,
op gezag van de rector magnificus
prof.dr. L.M. Bouter,
in het openbaar te verdedigen
ten overstaan van de promotiecommissie
van de faculteit der Exacte Wetenschappen
op donderdag 2 april 2009 om 13.45 uur
in de aula van de universiteit,
De Boelelaan 1105

door

Valentin Paul Nicu

geboren te Sibiu, Roemenië

promotor: prof. dr. E. J. Baerends


to my mother

“Here’s to the Crazy Ones. The misfits. The rebels. The troublemakers. The round pegs in the square holes. The ones who see things differently. They’re not fond of rules. And they have no respect for the status quo. You can quote them, disagree with them, disbelieve them, glorify or vilify them. About the only thing that you can’t do, is ignore them. Because they change things. They invent. They imagine. They heal. They explore. They create. They inspire. They push the human race forward. Maybe they have to be crazy. How else can you stare at an empty canvas and see a work of art? Or, sit in silence and hear a song that hasn’t been written? Or, gaze at a red planet and see a laboratory on wheels? We make tools for these kinds of people. While some may see them as the crazy ones, we see genius. Because the ones who are crazy enough to think that they can change the world, are the ones who do.

Apple Computers “Think Different” ad campaign.

Computer time provided by the Dutch National Computing Facilities (NCF) is gratefully acknowledged.

The printing of this thesis was partially supported by:

Solvay Pharmaceuticals		www.solvaypharmaceuticals.nl
Scientific Computing & Modelling		www.scm.com

Cover design by wrinkly pea  www.wrinklypea.com

The picture Whirlpool Galaxy M51 used on the front cover is a property of NASA, ESA, and The Hubble Heritage Team (STScI/AURA) <http://heritage.stsci.edu>.

The picture of the M. Escher's Drawing Hands painting used on page 10 is a property of The M.C. Escher Company - the Netherlands www.mcescher.com.

ISBN 978-90-9024038-1

Contents

1	Introduction	1
1.1	Chirality	1
1.1.1	Generalities	1
1.1.2	Optical activity: a historical overview	2
1.1.3	Chirality in chemistry	3
1.1.4	Chirality in biology and drug industry	8
1.1.5	Chirality in literature and art	9
1.2	Spectroscopy and absolute configuration	10
1.3	Vibrational Circular Dichroism	12
1.4	This thesis	13
2	Theory	15
2.1	Rotational strength	15
2.1.1	Transition rates	15
2.1.2	Interaction with circularly polarized light	16
2.1.3	Circular dichroism intensities	19
2.1.4	Properties of rotational strength	21
2.2	Stephens' equations for VCD	24
2.2.1	Born-Oppenheimer approximation	24
2.2.2	Beyond the Born-Oppenheimer approximation	30
2.2.3	Electronic contribution of the atomic axial tensor	33
2.2.4	The harmonic approximation	36
2.2.5	Stephens' equations for VCD: summary	40
3	Implementation of Stephens' equations for VCD in the ADF program package	43
3.1	Introduction	43
3.2	Implementation	44
3.2.1	Expression for the atomic axial tensor	45
3.2.2	Expression for the atomic polar tensor	47

3.2.3	Calculation of the $\mathbf{U}^{(1),\mathbf{R}_{\lambda\alpha}}$ matrix	48
3.2.4	Calculation of the $\mathbf{U}^{(1),\mathbf{H}_{\beta}}$ matrix	49
3.2.5	Contributions to the AATs from the occ–occ blocks of the $\mathbf{U}^{(1),\mathbf{H}_{\beta}}$ and $\mathbf{U}^{(1),\mathbf{R}_{\lambda\alpha}}$ matrices	49
3.3	Validation for a set of benchmark molecules	52
3.3.1	The Atomic Axial Tensors	53
3.3.2	The rotational strengths	56
3.4	Conclusions	62
4	Effects of complex formation on VCD spectra	65
5	Robust Normal Modes in VCD Spectra	67
5.1	Introduction	67
5.2	Theory	69
5.3	Method	71
5.4	Results and Discussions	74
5.4.1	Characterization of robust modes	74
5.4.2	Molecules with symmetry	79
5.4.3	Molecules without symmetry	82
5.5	Summary and conclusions	85
6	Enhancement of IR and VCD intensities due to charge transfer	89
6.1	Introduction	89
6.2	Theory	93
6.3	Computational Details	94
6.4	Results and Discussions	95
6.4.1	Normal mode analysis	99
6.4.2	The enhancement of IR/VCD intensity	101
6.4.3	The charge transfer	106
6.5	Summary and Conclusions	111
7	Summary and Conclusions	113
	Samenvatting	119
	Bibliography	125
	Acknowledgements	136
	Publications	140

Curriculum Vitae	143
-------------------------	------------

Chapter 1

Introduction

1.1 Chirality

1.1.1 Generalities

"I call any geometrical figure, or group of points, chiral, and say it has chirality, if its image in a plane mirror, ideally realized, cannot be brought to coincide with itself."

This definition stated by Lord Kelvin in 1904, in his Baltimore Lectures on Molecular Dynamics and the Wave Theory of Light is universally accepted as the definition of chirality. The term *chirality*, meaning handness, is derived from the greek word for hand, i.e. $\chi\epsilon\iota\rho$ (cheir), as the human hands are the most universally recognized example of chirality.

The objects that can be brought to coincide with their mirror image are called *achiral*. Kelvin's definition is basically the definition of achirality. Chirality is a dichotomous property, i.e. the chiral objects are the objects that fail to be achiral.

Chirality is a purely geometrical property, as Lord Kelvin clearly stated in his definition, i.e. "geometrical figure, or group of points". A first consequence is that the symmetry of a geometrical object determines whether it is chiral or not. Chirality excludes improper symmetry elements, i.e. center of inversion, mirror-planes, and rotation-reflexion axes. However, chiral figures are not necessary asymmetric, that is lack of all symmetry elements, since they may possess one or more proper rotation axes. Hence chirality is supported by the point groups comprising only proper rotations, i.e. C_n , D_n , O , T . A second consequence is that chirality is not related in any particular way to chemistry or biology. In fact, chirality is a property that is very common throughout our universe. It can be found in molecular, macromolecular and supramolecular system, cells and living

organisms but also in cosmic objects, e.g. spiral galaxies.

1.1.2 Optical activity: a historical overview

The ability of certain materials to rotate the polarization plane of a plane-polarized electromagnetic field as the field passes through the material is called *optical activity*.

Optical activity was observed for the first time in 1811 by French physicist Francois Jean Dominique Arago (1786–1853) in the form of colors in sunlight that had passed along the optic axis of a quartz crystal placed between crossed polarizers. Around this same time (1812), Jean Baptiste Biot (1774–1862) also observed the effect in liquids and gases of organic substances such as turpentine. Subsequent experiments by Biot established that the colours were due to two distinct effects: *optical rotation*, that is the rotation of the plane of polarization of a linearly polarized light beam; and *optical rotatory dispersion*, that is the unequal rotation of the plane of polarization of light of different wavelengths. Biot also discovered a second form of quartz which rotated the plane of polarization in the opposite direction and also recognized (1818) that for a fixed path length through the quartz the rotation angle was inversely proportional to the square of the light wavelength.

In 1822, the English astronomer Sir J. F.W. Herschel (1792–1871) noted a correlation between optical rotation and crystal *hemihedrism*. The hemihedrism phenomenon, i.e. the arrangement of the facets of a crystal that produces non-superimposable mirror images, was discovered by crystallographer Rene-Just Haüy (1743–1822) in 1801 who noticed it in quartz crystals. (The term *enantiomorphous*, i.e. in opposite shape, was created to describe the macroscopic relationships between non-superimposable, mirror-image crystalline forms.)

All these discoveries culminated in 1848 with Louis Pasteur's great achievement, i.e. the separation of a racemic mixture of tartrate crystals into its optical antipodes (levorotatory tartaric acid was unknown up to that time). Observing that the tartrate crystals have facets inclining to the right or left, i.e. the hemihedrism of the tartrate crystals (which is not usually observed for crystals of optically active substances), Pasteur was able to mechanically (manually) separate the two crystal forms and achieve the first resolution. Then, by dissolving the two kinds of crystals separately, he determined their optical activity to be identical and of opposite sign. Finally, by extending the concept of hemihedric faces observed in crystals to molecules, Pasteur provided a reasonably satisfactory explanation for his (also previous) experiments.

In 1874, Jacobus Henricus van't Hoff and Joseph Achille Le Bel independently

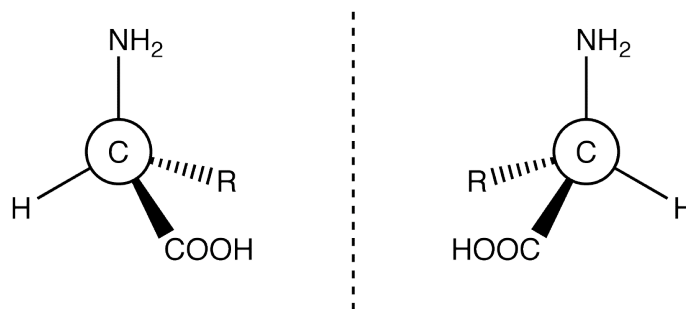


Figure 1.1: Point Chirality. The enantiomers of a generic amino acid.

proposed that the phenomenon of optical activity could be explained by assuming that the chemical bonds between carbon atoms and their neighbors were directed towards the corners of a regular tetrahedron. This led to a better understanding of the three-dimensional nature of molecules.

1.1.3 Chirality in chemistry

Nomenclature

In chemistry the study of chirality falls in the domain of stereochemistry which unites the traditionally-defined sub-disciplines of inorganic chemistry, organic chemistry and physical chemistry.

The two non-superimposable, mirror-image forms of chiral molecules are referred to as *enantiomers*. Since the enantiomers of a chiral molecule exhibit optical activity of different signs and equal magnitude they are also called optical isomers.

A mixture of equal amounts of two enantiomers of a chiral compound is called a *racemic* mixture. The word “racemic” is derived from the Latin word for grape, the origins of the word being related to the fact that Pasteur isolated racemic tartaric acid from wine. Racemic mixtures do not exhibit optical activity.

Most chiral molecules exhibit *point chirality*. The chiral center is usually an atom (though it does not necessarily have to be an atom), most often a carbon atom having four different substituents. This is the case of chiral amino acids where the α -carbon is the stereogenic centre, having point chirality (see Fig. 1.1). It should be noted that even isotopic differences must be considered when examining chirality.

It is also possible for a molecule to have multiple chiral centers without being chiral overall, if there is a symmetry element (mirror plane or inversion center) which relates those chiral centers. Such compounds are referred to as *meso* com-

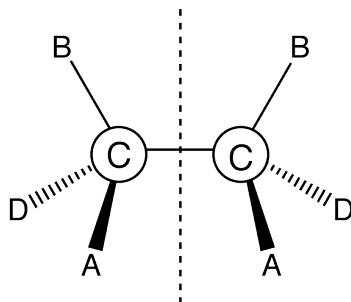


Figure 1.2: Schematic representation of a meso compound.

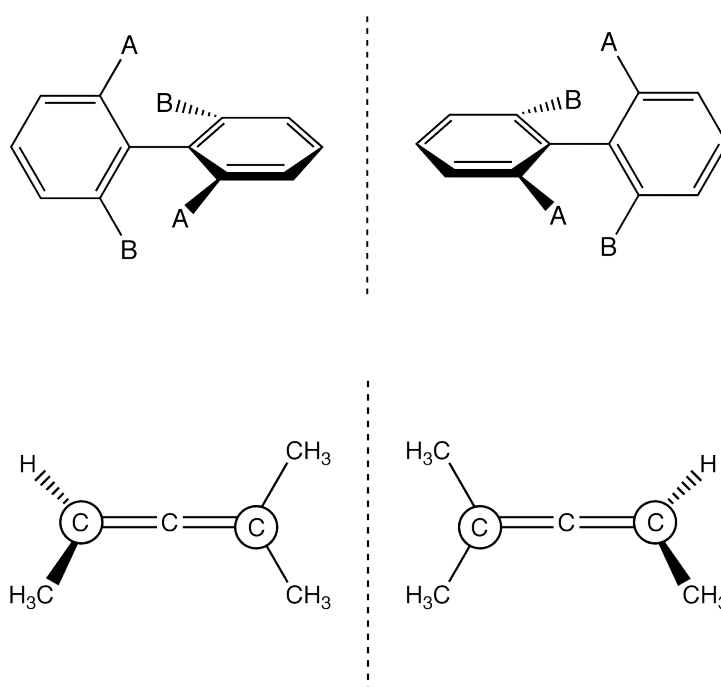


Figure 1.3: Axial Chirality. Schematic representations of the enantiomers of chiral allenes (lower panel) and biphenyls (upper panel).

pounds (see Fig. 1.2).

There are also chiral molecules that do not have a chiral center. Thus, one can distinguish between *axial chirality* (Fig. 1.3), *helical chirality* (Fig. 1.4), and *planar chirality* (Fig. 1.5).

Many coordination compounds are also chiral. For example, Fig. 1.6 shows the well-known tris(ethylenediaminato) cobalt(III) complex, $[\text{Co}(\text{en})_3]^{3+}$. The $[\text{Co}(\text{en})_3]^{3+}$ complex has point chirality, with the Co atom being the stereogenic centre. It is also important to note that $[\text{Co}(\text{en})_3]^{3+}$ is highly symmetric, it has

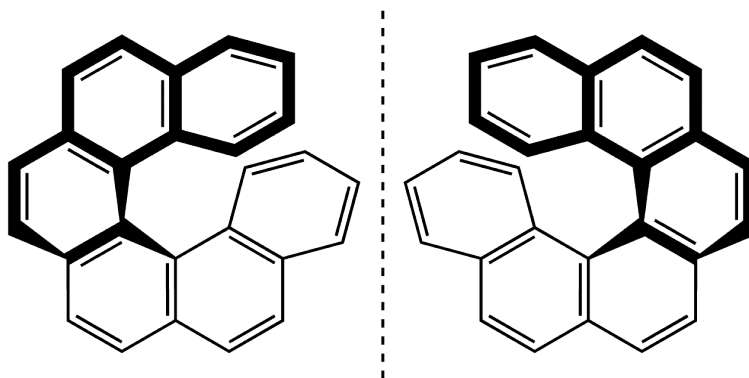


Figure 1.4: Helical Chirality. Schematic representation of the enantiomers of hexa-helicene.

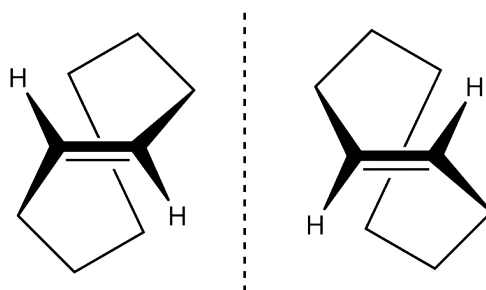


Figure 1.5: Planar chirality. Schematic representation of the enantiomers of trans-cyclooctane.

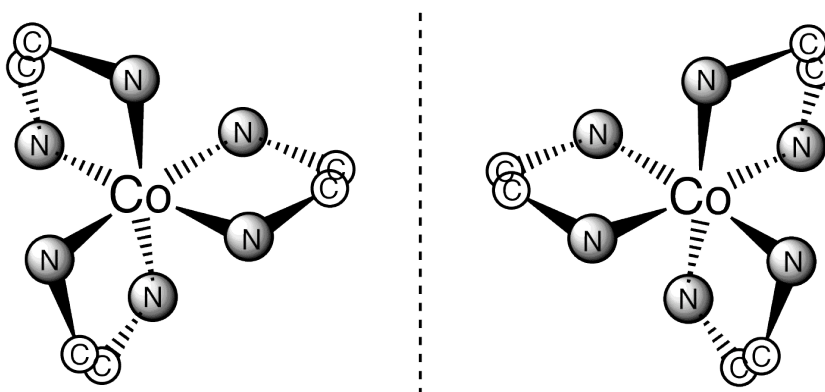


Figure 1.6: Schematic representation of the enantiomers of $[\text{Co}(\text{en})_3]^{3+}$. A coordination compound with point chirality and high symmetry (D_3).

D_3 symmetry, i.e. it has one C_3 symmetry axis and three C_2 symmetry axes (perpendicular to the axis C_3).

In the gas phase or when dissolved in solution, molecules are usually very flexible and therefore may adopt a variety of different conformations. These various conformations are themselves almost always chiral. One must make a clear distinction between conformation and configuration when discussing chirality in a molecular context. Thus, two molecules which differ only by rotations around single bonds are said to be two different conformations of the same molecule. Whereas, two molecules which have the same chemical composition but can only be made identical, i.e. superimposable, by breaking and reforming bonds are said to be two configurations of the same set of atoms.

Naming conventions

The arrangement in space of the substituents of a stereogenic unit, i.e. a chirality center, a chirality plane or a chirality axis, is called absolute configuration (AC). Enantiomers have opposite absolute configurations.

In 1906 M. A. Rosanoff proposed the D/L nomenclature system for denoting enantiomers. He arbitrarily assigned the dextrorotatory (dextro = right) (+)-glyceraldehyde to the D configuration, and the levorotatory (levo = left) (-)-glyceraldehyde to the L configuration. Since certain chemical manipulations can be performed on glyceraldehyde without affecting its configuration, the enantiomers of a molecule are named D or L depending from which isomer of glyceraldehyde they can be obtained from chemical reactions that did not change any bond at a stereogenic unit.

Because the D/L system is not unequivocal in all cases and cannot easily be applied to all families of compounds, in the early sixties, R. S. Cahn, C. K. Ingold, and V. Prelog introduced a new system, the R/S system.

For chemists, the R/S system is the most important nomenclature system for denoting enantiomers. The R/S system is more general than the D/L system since it does not involve a reference molecule such as glyceraldehyde and can also be extended to molecules without a chiral center. Moreover, it can also label, for example, an (R,R) isomer versus an (R,S) diastereomer, i.e. isomers that have opposite configurations at one or more of the chiral centers but are not mirror images of each other.

In the R/S system, one labels first each chiral center (as R or S) based on its atomic number according to the Cahn Ingold Prelog (CIP) priority rules (given below). Then, by orientating the chiral center so that the lowest-priority of the four is pointed away from a viewer, there are two possibilities: 1) if the priority

of the remaining three substituents decreases in clockwise direction, it is labeled R (for Rectus), and 2) if it decreases in counterclockwise direction, it is S (for Sinister).

The Cahn Ingold Prelog (CIP) priority rules:

Rule 1: The four substituents of a tetrahedral chirality center are ranked in order of decreasing atomic number of the atoms directly bonded to the chirality center. Isotopes of the same chemical element are listed in order of decreasing atomic mass.

Rule 2: Where two or more atoms bonded to the chirality center have the same atomic number, the second atoms are used to rank the substituents. If the second atoms are also the same, the third are used, and so on.

It should be noted that there is no fixed connection between the R/S and D/L systems, i.e. an R isomer can be either D or L. We also note that the D/L system remains in common use in certain areas of biochemistry, e.g. amino acid and carbohydrate chemistry, because it is convenient to have the same chiral label for all of the commonly occurring structures of a given type of structure in higher organisms, e.g. in the D/L system all such structures are L, whereas in the R/S system they are mostly S but there are some common exceptions.

Finally, we note that enantiomers can also be named according to the direction in which they rotate the plane of polarized light. If it rotates the light clockwise (as seen by a viewer towards whom the light is traveling), that enantiomer is labeled (+), whereas its mirror-image is labeled (−). The (+) and (−) isomers have also been termed *d* and *l*, respectively, (for dextrorotatory and levorotatory). However, this labeling is easy to confuse with D and L. As before there are no direct fixed relations between the (+) and (−) system and the R/S and D/L systems.

Properties of enantiomers

Most physical properties do not depend on the absolute configuration. Thus, enantiomeric pairs have identical melting point, boiling point, color, hardness, density, solubility, etc. As a result, one can not distinguish the enantiomers of a chiral molecule by looking at these “ordinary” physical properties. However, enantiomers interact differently with other chiral objects, e.g. chiral molecules or circularly polarized electromagnetic fields. This can be illustrated by looking at how our hands and feet (both are chiral) interact with other achiral and chiral

objects. Thus, there are no differences between our left and right limbs when holding a drum stick or a pen in our hands, or when handling a ball with our hands or feet (drum sticks, pens and balls are achiral objects). Whereas, the differences between our left and right limbs are immediately apparent when trying to shake someone's left hand with our right hand or when trying to put our right foot in a left shoe (hands and shoes are chiral objects).

Enantiomers behave the same way, they interact differently with other chiral objects but not with achiral objects. For instance, enantiomers react at the same rate with achiral compounds, but at different rates with chiral compounds; they also exhibit different solution behaviour in pure chiral solvents. Optical activity, the interaction of chiral molecules with circularly polarized electromagnetic fields (which are chiral), is another example of non-equivalent enantiomeric interaction.

Due to their non-equivalent behavior in chiral media, enantiomers are highly selective reagents that can be used to induce enantio-selectivity, i.e. produce exclusively or predominantly one enantiomer at the expense of the other. In general, laboratory chemical reactions produce racemic mixtures. However, as mentioned, these racemic mixtures can be separated by using chiral reagents. As it will be discussed in the next two sections enantio-selectivity plays a crucial role in biology and drug industry.

1.1.4 Chirality in biology and drug industry

The amino acids (the building blocks of proteins) and sugars (which when combined with nucleic acids form the building blocks of DNA) are chiral. Interestingly, in living organisms, all amino acids are left-handed and all sugars are right-handed. That is, in living organisms amino acids and sugars exhibit homochirality. This homochirality of the amino acids and sugars leads to homochirality in higher-order structures such as the right-handed α -helix and the B-type DNA double helix.

Although the origin of homochirality in the biological systems is currently unknown, its consequences are immediately apparent. Thus, many biological processes are triggered by only one of the two possible enantiomers of a chiral molecule; enzymes (which are always chiral) often distinguish between the two enantiomers of a chiral substrate. This characteristic of biological processes is consistent with the non-equivalent interaction exhibited by enantiomers in chiral media discussed in the previous section. Consequently, since many drugs consist of chiral molecules, and since drugs interact with the organism at molecular level, often only one of the enantiomers has the desired pharmacological activity, the other enantiomer may be inactive, less active, or even toxic.

One such example is Thalidomide, a racemic drug that was administrated to pregnant women between 1956–1962. While one enantiomer is effective against morning sickness, which was the intended scope of the drug, the other one is teratogenic (roughly meaning causing malformations). The results of releasing the drug to the general public were catastrophic, more than twelve thousand (12000) infants were born with severe malformations, the most renowned being Phocomelia (meaning seal arms).

It should be noted that Thalidomide is just one of many racemic drugs that are potentially harmful. Similar example are Ethambutol (one enantiomer is used to treat tuberculosis, the other causes blindness) and Naproxen (one enantiomer is used to treat arthritis pain, but the other causes liver poisoning with no analgesic effect) to name but a few.

A less dramatic example that shows how differently the enantiomers of a compound are perceived by our organism is Limonene. Limonene is chiral, as are the smell receptor in our nose. While the R enantiomer of Limonene is associated to the smell of lemons, the S enantiomer is associated to the smell of oranges.

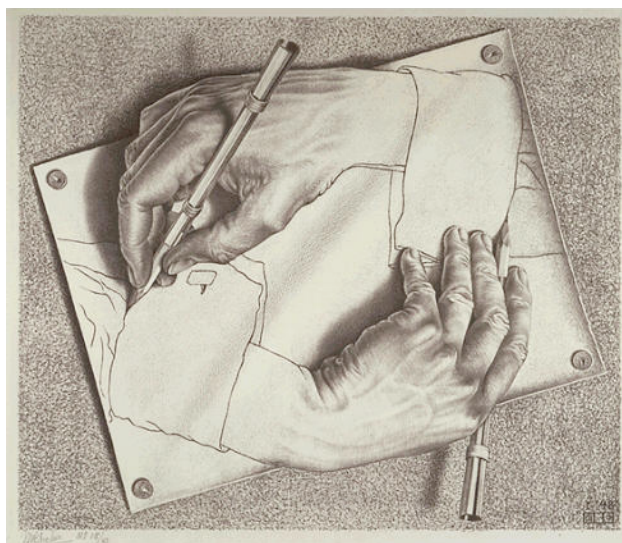
The above examples clearly show that in order to understand how chiral drugs interact with our organism it is crucial to know their absolute configuration. Consequently, there is an evident need for spectroscopic techniques that allow for reliable determinations of AC of chiral molecules. A short overview of the spectroscopic methods that can be used to determine the AC of chiral compounds is given in section 1.2.

1.1.5 Chirality in literature and art

The mirror image and the possibility of having non-identical mirror images have fascinated philosophers, writers and artists even before chirality or optical activity was discovered by scientists. Thus, the first discussion on handedness and its dependence on space dimensionality begins with Immanuel Kant, the famous Prussian philosopher, who was captivated by what he dubbed incongruent counterparts to describe the existence of two nonsuperimposable mirror-image objects [1]:

“What can more resemble my hand or my ear, and be more equal in all points, than its image in the mirror? And yet I cannot put such a hand as is seen in the mirror in the place of its original ...”

Although little was known about chemical chirality in the time of Lewis Carroll, his work “Through the Looking-glass and what Alice found there” (1871) contains a reference to the differing biological activities of enantiomeric drugs: “Perhaps Looking-glass milk isn’t good to drink,” Alice said to her cat.



M.C. Escher's "Drawing Hands"

(c) 2009 The M.C. Escher Company - the Netherlands.

All rights reserved. Used by permission. www.mcescher.com

Figure 1.7: Drawing Hands painting by M.C. Escher

The English novelist Edwin A. Abbott (1838–1926) explained in the satire entitled “Flatland” (1884) that in two dimensions (flatland) two equal scalene triangles that are orientated differently can not be brought into coincidence by translation or rotation but only by reflexions across a straight line (the mirror in flatland). The fantastic story written by Abbott was preceded by a more rigorous mathematical study of A. F. Möbius (1790–1868). August F. Möbius after whom the Möbius strip is named, proved that two non-superimposable objects in three-dimensional space become identical when one of them is rotated in a fourth dimension [2].

Finally, we should also mention the dutch engraver Maurits C. Escher (1898–1972) who took admirable advantage of symmetry in his the extraordinary drawings. Figure 1.7 shows the famous etching Drawing Hands.

1.2 Spectroscopy and absolute configuration

Before 1951 no spectroscopic techniques capable of determining the absolute configuration of chiral molecules were available. Although it was possible to distinguish between the (pure) enantiomers of a compound by using optical activity, it was impossible to make a direct correlation between the optical activity of a compound and its absolute configuration. As a result the standard method was to use Rosanoff’s D/L nomenclature system, i.e. the absolute configuration

Methode	Advantage	Disadvantage
XRD	- reliable	- not applicable to solutions since single crystal samples are required - measurements are not always readily doable since many organic and bio-organic compounds are difficult to crystalize
NMR	- straightforward measurements	- requires chiral shift reagents, chiral additives or derivatization
ECD	- straightforward measurements - can predict solutions conformation	- spectra consist of few signals - solvent dependent signal sign - requires computation of excited states - requires presence of chromophores
ORD	- straightforward measurements	- is a property of the bulk sample, there is no direct relation between spectra and the molecular structure of the sample - requires computation of excited states
VCD	- straightforward calculations - can predict solutions conformation	- although practical, measurements are somewhat difficult because VCD signals have weak intensities
VROA	- measurements can be performed for a wide frequency range	- the computation of VROA spectra are still expensive

Table 1.1: Summary of the advantages and disadvantages of spectroscopic techniques that are able to determine the absolute configuration of chiral molecules.

of a compound was related to the absolute configuration of glyceraldehyde (as discussed in section 1.1.3).

In 1951, the Dutch chemist and crystallographer J. M. Bijvoet, invented a new special x-ray crystallography technique, called anomalous x-ray dispersion (XRD), which enabled him to determine for the first time the absolute configuration of a chemical compound, i.e. sodium rubidium tartrate [3]. Using his technique, Bijvoet has shown that the dextrorotatory (+)-tartaric acid has L configuration. Then, by comparing L-(+)-tartaric acid and (+)-glyceraldehyde he determined that (+)-glyceraldehyde should be definitely assigned to the D configuration. Once the absolute configuration of (+)-glyceraldehyde was known, the absolute configuration of all the compounds (thousands) that have been related to (+)-glyceraldehyde by chemical reactions before 1951 was known.

Gradually, more spectroscopic techniques capable of determining the absolute configuration of chiral molecules have been developed, e.g. electronic circular dichroism (ECD), optical rotatory dispersion (ORD), and more recently, vibrational circular dichroism (VCD) and vibrational Raman optical activity (VROA). The main advantages and disadvantages of these spectroscopic techniques are summarized in Table 1.1.

As can be seen in Table 1.1 each method has its own disadvantages. Conse-

quently, depending on the situation at hand one method may be more suitable than the other methods, i.e. may reveal additional information, or alternately, may be less ambiguous. Furthermore, given how important it is in pharmaceutical industry to assign correctly the absolute configuration of chiral drugs, it is always prudent to use more than one method for a given compound. Thus, even though each of these methods is suitable for determining the three-dimensional molecular structure, cross verification of the conclusions obtained with individual methods should be mandatory when the employed methods are stretched to their limits.

1.3 Vibrational Circular Dichroism

Vibrational circular dichroism (VCD), i.e. the differential absorption of left and right circularly polarized light for a vibrational transition, is the central topic of this thesis.

The first VCD investigations began in the late 1960 and early 1970 with the theoretical studies of Moscovitz et al. [4, 5], Holzwarth et al. [6] and Schellman [7, 8]. These studies have estimated that VCD signals are strong enough to be observed experimentally. (Normally, VCD intensities are approximatively 4 orders of magnitude lower than the IR intensities.)

The first experimental observation of VCD was reported by Holzwarth et al. in 1973 [9, 10]. Then, in 1975 Stephens et al. have reported the implementation of a more flexible and sensitive VCD spectrometer [11] and VCD experimental spectra as well. Critical for these new measurements was the use of a ZnSe photoelastic modulator and of a newly invented method called polarization scrambling (invented by Stephens' post doc Jack Cheng) that allowed for a significant reduction of the so called pseudo-CD signals, i.e. experimental artifacts that are unrelated to the CD of the sample. Further developments of the VCD instrumentations were made by Nafie et al. in 1979 with the implementation of the Fourier-transform VCD spectrometer [12]. However, in spite of all these developments the applicability of VCD spectroscopy was still limited since the absolute configuration of a compound can not be assigned based on its experimental VCD spectrum alone. As in the case of optical activity, no direct correlation can be made between the absolute configuration of a compound and its experimental VCD spectrum.

Since the VCD spectra of enantiomeric pairs have equal magnitudes but opposite signs, the most direct and elegant approach for determining the absolute configuration of a chiral compound would be by comparing its experimental VCD

spectrum to a calculated VCD spectrum. If the main features of the experimental and calculated VCD spectra have the same sign, the experimental sample has the same AC as the enantiomer used in the simulation (which is known), whereas if the signs are different so is the AC. It is therefore clear that accurate determinations of AC using VCD require reliable computation of VCD spectra.

Historically, computation of VCD spectra was a challenge. The VCD intensity of a vibrational transition is given by the rotational strength (R) of that transition, that is, the inner product between the electric and magnetic dipole transition moments associated to the respective transition. While the calculation of the electric dipole transition moment (EDTM) is straightforward, the electronic contribution to the magnetic dipole transition moment (MDTM) is exactly zero within the Born-Oppenheimer (BO) approximation.

The most natural approach that can be employed to remedy this problem is to use wave functions of higher accuracy, e.g. corrected BO wave functions obtained by mixing BO wave functions of the excited states into the ground-state eigenfunction. However, as it turned out, the expression obtained for the electronic component of the MDTMs is a sum over all excited states. Thus, although the electronic component of the MDTM does not vanish anymore, calculations are still impractical without resorting to truncations.

The solution to this problem was given by P. J. Stephens in 1984, who showed that the sum over states can be reduced exactly, the obtained expression depending only on the adiabatic wave function of the ground electronic state [13]. As a result of this breakthrough, accurate calculations of vibrational MDTM became readily possible. The final step that made VCD spectroscopy routinely applicable and established it as the method of choice for the determination of the absolute configuration of gas phase molecules, molecules in solution, neat liquids, powder solids and dispersions, was the DFT implementation of Stephens' equations of VCD (using London-atomic orbitals) in the Gaussian program package by Jim Cheeseman [14].

1.4 This thesis

The main topic of this thesis is the interpretation of VCD spectra, the scope being a better understanding of the differences between experimental and calculated VCD spectra. Knowledge and understanding of the mechanisms responsible for these differences is crucial for: 1) successful determination of absolute configuration of chiral compounds, 2) understanding the limitations of the technique, and 3) the further development of the technique.

The thesis is organized as follows. Chapter 2 presents the general theory of optical activity, and the derivation of Stephens' equations for VCD. Chapter 3 describes the implementation of Stephens' equations in the Amsterdam Density Functional (ADF) program package, and the validation of our VCD implementation. In Chapter 4 we investigate the effects induced by complex formation on VCD spectra. Chapter 4 is the core of this thesis, the fundamental concepts introduced in this chapter being the subjects of the remaining chapters of the thesis. Thus, in chapter 5 the concept of *robust modes* introduced in chapter 4 is further investigated and validated by studying the distributions of the angles ξ , i.e. the angle between the electric and magnetic dipole transition moments, using a test set of 27 molecules. Then, in chapter 6 the analysis of the mechanisms responsible for the enhancements of the IR and VCD intensities due donor-acceptor interaction (also introduced in chapter 4), are further extended and validated by direct comparisons to experimental data using the complex $[\text{Co}(\text{en})_3]^{3+} \cdots 2\text{Cl}^-$ as an example. Finally, the thesis is summarized with some concluding remarks.

Chapter 2

Theory

In this chapter the theory of vibrational circular dichroism is presented. Since in the case of VCD one is interested only in the absorption of electromagnetic radiation by the molecular system, a semi-classical description of the interaction between light and molecules can be assumed. That is, we consider the molecules as being quantum mechanical objects perturbed by classical electromagnetic fields.

A rigorous description of the light–matter interaction requires the use of quantum electrodynamics, i.e. both the molecules and the radiation should be treated as quantum mechanical objects. However, as shown in references [15–18], the semiclassical approach predicts correctly the results we need, but in a more direct manner. A quantum electrodynamics treatment of the light–matter interaction can be found in reference [19].

First, we derive a quantum mechanical expression for the circular dichroism intensity, i.e. rotational strengths, using Fermi’s golden rule and the interaction hamiltonians for left and right circularly polarized light. Then, we look at the properties of rotational strength. Finally, implementable expressions for the VCD intensities are obtained, the so called Stephens’ equations for VCD, by using first order corrections to the Born-Oppenheimer wave function and the harmonic approximation.

2.1 Rotational strength

2.1.1 Transition rates

We consider a molecule \mathcal{M} having N_λ nuclei and N_e electrons interacting with a classical electromagnetic field. The energy exchange between the molecule and the field induces transitions between the various molecular states. The intensities of the molecular spectra depend on the rate of energy transfer between the

molecule and the radiation field. Thus, the spectral intensities are proportional to the transition rates (W), i.e. the rate at which the probability of being in an empty state changes:

$$W = \frac{dP_f(t)}{dt} \quad (2.1)$$

where $P_f(t)$ is the probability to find the system in a state $|f\rangle$.

The radiation beam used in IR spectroscopy is not monochromatic, i.e. it contains a continuous range of frequencies. As a result, the observed spectral intensities are the integral over the signals resulting from all transitions that can be induced by the perturbing electromagnetic field. This means that instead of considering all the transitions to a single final state $|f\rangle$, one needs to consider all the transition to a group of final states $|f'\rangle$ that have energies in an energy range $(E_f - \mu, E_f + \mu)$ (E_f is the energy of a final state $|f\rangle$).

From standard time-dependent perturbation theory the transition rate for transitions from an initial state $|i\rangle$ (e.g. the ground state) to a “continuum” of states $|f'\rangle$ is given by Fermi’s golden rule [15]. Thus, by denoting the density of states $|f'\rangle$ per unit of energy with $\rho(E)$, the Fermi’s golden rule is given by the following equation [15]:

$$W = \frac{2\pi}{\hbar} |V_{fi}|^2 \rho(\Delta E_{fi}) \quad (2.2)$$

where $\rho(\Delta E_{fi})$ is the density of states $\rho(E)$ evaluated at $\Delta E_{fi} = E_f - E_i$ and \hbar is Planck’s constant divided by 2π . For a time-dependent perturbation Hamiltonian of the form $H^{(1)}(t) = A(e^{i\Phi t} + e^{-i\Phi t}) + B(e^{i\Phi t} - e^{-i\Phi t})$, the term V_{fi} is determined by the time independent parts of the hamiltonian [15, 16], i.e. $V = A + B$:

$$V_{fi} = \langle f|A + B|i\rangle \quad (2.3)$$

where $|i\rangle$ and $|f\rangle$ are solutions of the unperturbed time-independent Schrödinger equations. We note that the wave functions $|i\rangle$ and $|f\rangle$ are both real since they are eigenfunctions of the unperturbed Hamiltonian which is real.

2.1.2 Interaction with circularly polarized light

The electric (\vec{E}) and magnetic (\vec{M}) vectors associated to a circularly polarized electromagnetic field, can be written as a sum of two phase shifted electric and magnetic, respectively, vector components along the x and y axis [15, 16]. Thus, for a electromagnetic field propagating along the z direction we have:

$$\vec{E}_{\pm}(t) = 2E_0 \left\{ \vec{e}_x \cos \left[\omega \left(t - \frac{z}{c} \right) \right] \pm \vec{e}_y \sin \left[\omega \left(t - \frac{z}{c} \right) \right] \right\} \quad (2.4)$$

$$\vec{B}_{\pm}(t) = -2B_0 \left\{ \pm \vec{e}_x \sin \left[\omega \left(t - \frac{z}{c} \right) \right] - \vec{e}_y \cos \left[\omega \left(t - \frac{z}{c} \right) \right] \right\} \quad (2.5)$$

where \vec{e}_x and \vec{e}_y are the unit vectors of the x and y axis, respectively, the indexes \pm represents the handedness of the two fields: “+” labels the left circularly polarized fields and “−” labels the right circularly polarized fields, E_0 and B_0 are the time independent amplitudes of the two fields, t represents the time coordinate, c the velocity of light in vacuum, ω is the angular frequency of the fields, and z is a spatial coordinate.

The magnetic interaction is approximately two orders of magnitude smaller than the electric one [18] and as a result very often it is neglected. However, as will be shown below, in order to explain optical activity it is crucial to consider both the electric and the magnetic interactions. Thus, the perturbation hamiltonian for an electromagnetic field is:

$$H^{(1)} = -\vec{\mu}_E \cdot \vec{E} - \vec{\mu}_M \cdot \vec{B} \quad (2.6)$$

where $\vec{\mu}_E$ and $\vec{\mu}_M$ are the electric and magnetic dipole operators. The vector operators $\vec{\mu}_E$ and $\vec{\mu}_M$ have electronic and nuclear contributions. For a molecule with N_λ nuclei and N_e electrons they are defined as follows [20]:

$$\vec{\mu}_E = \vec{\mu}_E^{el} + \vec{\mu}_E^{nuc} \quad \text{with} \quad \vec{\mu}_E^{el} = -\sum_a e_a \vec{r}_a, \quad \vec{\mu}_E^{nuc} = \sum_\lambda e Z_\lambda \vec{R}_\lambda \quad (2.7)$$

$$\vec{\mu}_M = \vec{\mu}_M^{el} + \vec{\mu}_M^{nuc} \quad \text{with} \quad \vec{\mu}_M^{el} = -\frac{e}{2mc} \sum_a \vec{r}_a \times \vec{p}_a, \quad \vec{\mu}_M^{nuc} = \sum_\lambda \frac{e Z_\lambda}{2M_\lambda c} \vec{R}_\lambda \times \vec{P}_\lambda \quad (2.8)$$

In Eqs. (2.7) and (2.8) the superscripts *el* and *nuc* label electronic and nuclear contributions, respectively, the summation indexes a and λ run over all electrons and nuclei, respectively, \vec{r}_a and \vec{R}_λ are the position vector of the a^{th} electron and of the λ^{th} nucleus, respectively, \vec{p}_a and \vec{P}_λ are the momentum vectors of the a^{th} electron and of the λ^{th} nucleus, respectively, c is the velocity of light in vacuum, e is the electronic charge, m is the mass of an electron, and M_λ is the mass of the λ^{th} nucleus.

Introducing Eqs. (2.7) and (2.8) into Eq. (2.6) we obtain:

$$H_{\pm}^{(1)}(t) = -2E_0 [(\mu_E)_x \cos \Phi t \pm (\mu_E)_y \sin \Phi t] + 2B_0 [\pm (\mu_M)_x \sin \Phi t - (\mu_M)_y \cos \Phi t] \quad (2.9)$$

where $(\mu_E)_k$ and $(\mu_M)_k$ ($k = x, y$) are the Cartesian components of the electric and magnetic dipole moment operators, and $\Phi t = \omega \left(t - \frac{z}{c}\right)$.

As can be seen from Eq. (2.9), the left and right circularly polarized radiation interacts differently with matter.

Substituting in Eq. (2.9) $\cos \Phi t$ and $\sin \Phi t$ with $\frac{1}{2} (e^{i\Phi t} + e^{-i\Phi t})$ and

$-\frac{i}{2}(e^{i\Phi t} - e^{-i\Phi t})$, respectively, we obtain:

$$H_{\pm}^{(1)}(t) = -E_0 [(\mu_E)_x (e^{i\Phi t} + e^{-i\Phi t}) \pm i(\mu_E)_y (e^{i\Phi t} - e^{-i\Phi t})] + B_0 [\pm i(\mu_M)_x (e^{i\Phi t} - e^{-i\Phi t}) - (\mu_M)_y (e^{i\Phi t} + e^{-i\Phi t})] \quad (2.10)$$

From Eq. (2.10), the time-independent parts of the $H_{\pm}^{(1)}(t)$ required to calculate transition rates are:

$$V_{\pm} = -E_0 [(\mu_E)_x \pm i(\mu_E)_y] + B_0 [\pm i(\mu_M)_x - (\mu_M)_y] \quad (2.11)$$

The matrix elements $\langle f|V_{\pm}|i\rangle$ are then written:

$$\langle f|V_{\pm}|i\rangle = -E_0 (E_{fi}^x \pm iE_{fi}^y) + B_0 (\pm iM_{fi}^x - M_{fi}^y) \quad (2.12)$$

where $E_{fi}^k = \langle f|(\mu_E)_k|i\rangle$ and $M_{fi}^k = \langle f|(\mu_M)_k|i\rangle$ with $k = x, y$.

To evaluate Eq. (2.2) we need the square of $\langle f|V_{\pm}|i\rangle$. Thus, from Eq. (2.12) we have:

$$|\langle f|V_{\pm}|i\rangle|^2 = \left\{ -E_0 (E_{fi}^x \pm iE_{fi}^y) + B_0 [\pm iM_{fi}^x - M_{fi}^y] \right\} \times \left\{ -E_0 (E_{fi}^x \pm iE_{fi}^y) + B_0 (\pm iM_{fi}^x - M_{fi}^y) \right\}^* \quad (2.13)$$

At this point it is important to realize that the wave functions $|i\rangle$ and $|f\rangle$, and the operator $\vec{\mu}_E$ are real, whereas the operator $\vec{\mu}_M$ is purely imaginary. Using the hermiticity of the $\vec{\mu}_E$ and $\vec{\mu}_M$ operators, we can write:

$$E_{if}^k = (E_{fi}^k)^* \quad \text{and} \quad M_{if}^k = (M_{fi}^k)^* \quad (2.14)$$

Then, since $\vec{\mu}_E$ is real and $\vec{\mu}_M$ is purely imaginary, we have:

$$E_{if}^k = E_{fi}^k \quad \text{and} \quad M_{if}^k = -M_{fi}^k \quad (2.15)$$

where $k = (x, y, z)$.

Using Eqs. (2.15), Eq. (2.13) becomes:

$$|\langle f|V_{\pm}|i\rangle|^2 = E_0^2 (|E_{fi}^x|^2 + |E_{fi}^y|^2) + B_0^2 (|M_{fi}^x|^2 + |M_{fi}^y|^2) \pm 2iE_0B_0 (E_{fi}^x M_{if}^x + E_{fi}^y M_{if}^y) \quad (2.16)$$

Introducing Eq. (2.16) in Eq. (2.2) we obtain:

$$W_{\pm} = \frac{2\pi}{\hbar} [E_0^2 (|E_{fi}^x|^2 + |E_{fi}^y|^2) + B_0^2 (|M_{fi}^x|^2 + |M_{fi}^y|^2)] \rho(\Delta E_{fi}) \pm \frac{2\pi}{\hbar} [2iE_0B_0 (E_{fi}^x M_{if}^x + E_{fi}^y M_{if}^y)] \rho(\Delta E_{fi}) \quad (2.17)$$

For isotropic samples we need to average over all orientations. Thus, the terms $|E_{if}^k|^2$, $|M_{if}^k|^2$ and $E_{fi}^k M_{if}^k$ in Eq. (2.17) must be replaced by $\frac{1}{3}|\vec{E}_{if}|^2$, $\frac{1}{3}|\vec{M}_{if}|^2$ and $\frac{1}{3}\vec{E}_{if} \cdot \vec{M}_{if}$ respectively [15, 17]. Furthermore, the terms E_0^2 , B_0^2 and $E_0 B_0$ in Eq. (2.16) can be related to the energy of the electromagnetic field [15]. Thus, as shown in [16], Eq. (2.16) can be further written:

$$W_{\pm} = \frac{2\pi}{3\hbar^2} \left(|\vec{E}_{fi}|^2 + |\vec{M}_{fi}|^2 \pm 2i\vec{E}_{fi} \cdot \vec{M}_{fi} \right) \rho_{rad}(\Delta E_{fi}) \quad (2.18)$$

where $\rho_{rad}(\Delta E_{fi})$ is the energy density of radiation states [15].

Finally, we note that the experimental spectral intensities, and therefore also the transition rate (W), are proportional to the energy density of the radiation field. As a result, W can be expressed also using the Einstein coefficient of stimulated absorption (B_{fi}) [15]:

$$W_{\pm} = B_{fi}^{\pm} \rho_{rad}(\Delta E_{fi}) \quad (2.19)$$

By comparing Eqs. (2.18) and (2.19), we obtain the following expression of the coefficients B_{fi}^{\pm} :

$$B_{fi}^{\pm} = \frac{2\pi}{3\hbar^2} \left(|\vec{E}_{fi}|^2 + |\vec{M}_{fi}|^2 \pm 2i\vec{E}_{fi} \cdot \vec{M}_{fi} \right) \quad (2.20)$$

2.1.3 Circular dichroism intensities

The Beer-Lambert law states that the transmitted intensity $I(\nu)$, i.e the intensity observed after a beam of initial intensity $I_0(\nu)$ has passed through an experimental sample, depends on the length of the sample, l , the concentration of the sample, C_0 , and the molar absorption coefficient $\epsilon(\nu)$:

$$I(\nu) = I_0(\nu) e^{-\epsilon(\nu)C_0 l} \quad (2.21)$$

The Beer-Lambert law is an empirical law, however, it can be derived also from theoretical considerations [15]. As shown in reference [15], the experimental parameter $\epsilon(\nu)$ (molar absorption) can be related to theoretical parameter B_{if} (Einstein coefficient of stimulated absorption):

$$\int \epsilon(\nu) d\nu = \frac{h\nu_{fi}}{c} N_A B_{if} \quad (2.22)$$

where N_A is Avogadro's number and $\nu_{fi} = \frac{\Delta E_{fi}}{h}$.

The integral on the left side of Eq. (2.22) is called the integrated absorption coefficient (A) and represents the area under the experimental absorption band, i.e. the experimental intensity. Thus, we have:

$$A = \frac{h\nu_{fi}}{c} N_A B_{if} \quad (2.23)$$

By definition, the circular dichroism intensities are given by the difference between the integrated absorption coefficients (A) for left and right circularly polarized light, i.e. the differential absorption coefficient (ΔA):

$$\Delta A = A_+ - A_- = \frac{h\nu_{fi}}{c} N_A (B_{if}^+ - B_{if}^-) \quad (2.24)$$

Using Eq. (2.20), Eq. (2.24) becomes:

$$\Delta A = \left(\frac{32\pi^3}{3} \right) \left(\frac{\nu_{fi} N_A}{hc} \right) \text{Im} [E_{fi} M_{if}] \quad (2.25)$$

The term $\text{Im} [E_{fi} M_{if}]$ that appears in Eq. (2.25) is called rotational strength and is labeled R_{if} . As can be seen, R_{if} is defined as the imaginary part of the inner product between the electric and magnetic dipole transition moments:

$$R_{if} = \text{Im} [\vec{E}_{fi} \cdot \vec{M}_{if}] = \text{Im} [\langle i | \vec{\mu}_E | f \rangle \cdot \langle f | \vec{\mu}_M | i \rangle] \quad (2.26)$$

Equation (2.25) is called Rosenfeld equation, it states that the experimental circular dichroism intensity of a transition $|i\rangle \rightarrow |f\rangle$ is proportional to the rotational strength associated to that transition. When R_{if} is expressed in units of esu^2cm^2 , and ΔA in cm/mol , Eq. (2.25) can be written [16]:

$$\Delta A = 100.38 \bar{\nu}_{fi} R_{if} \times 10^{40} \quad (2.27)$$

where the band center $\bar{\nu}_{fi}$ is in units of $1/\text{cm}$.

It should be noted that R_{if} is a real quantity since as already mentioned \vec{M}_{if} is a purely imaginary vector. Furthermore, since ΔA depends on R_{if} alone, which in turn depends on both electric and magnetic dipole transition moments, it is clear that the magnetic interaction must not be neglected in order to obtain non-zero circular dichroism intensities.

Finally, we note that when the transition $|i\rangle \rightarrow |f\rangle$ represents an electronic transition we have electronic circular dichroism (ECD), whereas for a vibrational transition we have vibrational circular dichroism (VCD).

2.1.4 Properties of rotational strength

In this section two very important properties of rotational strength will be deduced by investigating the transformation law for rotational strength under an improper rotation (S_N).

When discussing the effects of a symmetry transformation in connection to a physical problem, it is possible to adopt two different points of view. Thus, when the so-called “passive” approach is used, one transforms the axes of the coordinate system while keeping fixed the physical system (the molecule in our case). The second approach, also called the “active”, consists in keeping the axes fixed and transforming the molecule. Although the two approaches are equivalent, i.e. yield identical results, the mathematical form of the equations describing the physical phenomena depend on the approach used. Thus, one should always mention which approach is used. In what follows we will consider the “active” approach, i.e. the symmetry operations transform the molecule (the system of coordinates remains unchanged).

The rotational strength associated to the $|i\rangle \rightarrow |f\rangle$ transition of molecule \mathcal{M} is given by Eq. (2.26):

$$R_{if}(\mathcal{M}) = \text{Im} [\langle i | \vec{\mu}_E | f \rangle \cdot \langle f | \vec{\mu}_M | i \rangle] \quad (2.28)$$

The operators $\vec{\mu}_E$ and $\vec{\mu}_M$, defined in Eqs. (2.7) and (2.8), can be written as:

$$\vec{\mu}_E = \vec{\mu}_E^{el} + \vec{\mu}_E^{nuc} = - \sum_a e_a \vec{r}_a + \sum_\lambda e Z_\lambda \vec{R}_\lambda = \sum_\alpha \vec{r}(\alpha) \quad (2.29)$$

$$\vec{\mu}_M = \vec{\mu}_M^{el} + \vec{\mu}_M^{nuc} = - \frac{e}{2mc} \sum_a \vec{r}_a \times \vec{p}_a + \sum_\lambda \frac{e Z_\lambda}{2M_\lambda c} \vec{R}_\lambda \times \vec{P}_\lambda = \sum_\alpha \vec{r}(\alpha) \times \vec{p}(\alpha) \quad (2.30)$$

In Eqs. (2.29) and (2.30) the summation index α runs over both electrons and nuclei; for $\alpha = a$ (a labels electrons) $\vec{r}(\alpha) = -e_a \vec{r}_a$ and $\vec{p}(\alpha) = (2mc)^{-1} \vec{p}_a$, whereas for $\alpha = \lambda$ (λ labels nuclei), $\vec{r}(\alpha) = e Z_\lambda \vec{R}_\lambda$ and $\vec{p}(\alpha) = (2M_\lambda c)^{-1} \vec{P}_\lambda$. Since the constants e , $e Z_\lambda$, $(2mc)^{-1}$ and $(2M_\lambda c)^{-1}$ do not depend on the coordinate system used, the “generalized” position $\vec{r}(\alpha)$ and momentum $\vec{p}(\alpha)$ vector operators defined above, transform under symmetry operation exactly like the “ordinary” position and momentum vector operators, respectively.

Using Eqs. (2.29) and (2.30), Eq. (2.28) becomes:

$$\begin{aligned} R_{if}(\mathcal{M}) &= \text{Im} \sum_{\alpha, \beta} \langle i | \vec{r}(\alpha) | f \rangle \langle f | \vec{r}(\beta) \times \vec{p}(\beta) | i \rangle \\ &= \text{Im} \sum_{\alpha, \beta} \sum_{k, l, m} \epsilon_{klm} \langle i | r_k(\alpha) | f \rangle \langle f | r_l(\beta) p_m(\beta) | i \rangle \end{aligned} \quad (2.31)$$

where ϵ_{klm} is the Levi-Civita tensor.

By acting with S_N on the molecule \mathcal{M} we obtain a new molecule \mathcal{M}' :

$$S_N \mathcal{M} = \mathcal{M}' \quad (2.32)$$

For the moment we will consider that \mathcal{M} and \mathcal{M}' are two different molecules. After obtaining the transformation law for the rotational strength under S_N we will also discuss the case when \mathcal{M} and \mathcal{M}' are identical.

The wave functions $|i'\rangle$ and $|f'\rangle$ of \mathcal{M}' associated to the states $|i\rangle$ and $|f\rangle$, respectively, of \mathcal{M} are given by relations similar to Eq. (2.32):

$$S_N |i\rangle = |i'\rangle, \quad S_N |f\rangle = |f'\rangle \quad (2.33)$$

The rotational strength associated to the $|i'\rangle \rightarrow |f'\rangle$ transition of \mathcal{M}' , is given by:

$$\begin{aligned} R_{if}(\mathcal{M}') &= \text{Im} [\langle i' | \vec{\mu}_E | f' \rangle \cdot \langle f' | \vec{\mu}_M | i' \rangle] \\ &= \text{Im} \sum_{\alpha, \beta} \sum_{k, l, m} \epsilon_{klm} \langle i' | r_k(\alpha) | f' \rangle \langle f' | r_l(\beta) p_m(\beta) | i' \rangle \end{aligned} \quad (2.34)$$

Using Eq. (2.33), Eq. (2.34) becomes:

$$\begin{aligned} R_{if}(\mathcal{M}') &= \\ &= \text{Im} \sum_{\alpha, \beta} \sum_{k, l, m} \epsilon_{klm} \langle i S_N^+ | r_k(\alpha) | S_N f \rangle \langle f S_N^+ | r_l(\beta) p_m(\beta) | S_N i \rangle \\ &= \text{Im} \sum_{\alpha, \beta} \sum_{k, l, m} \epsilon_{klm} \langle i | S_N^+ r_k(\alpha) S_N | f \rangle \langle f | S_N^+ r_l(\beta) S_N S_N^+ p_m(\beta) S_N | i \rangle \end{aligned} \quad (2.35)$$

The term $S_N^+ r_k(\alpha) S_N$, $S_N^+ r_l(\beta) S_N$ and $S_N^+ p_m(\beta) S_N$ in Eq. (2.35) represents the transformation law for the components of the vector operators $\vec{r}(\alpha)$, $\vec{r}(\beta)$ and $\vec{p}(\beta)$, respectively, upon a transformation of the molecule \mathcal{M} under the S_N symmetry operation. Therefore, in order to develop further Eq. (2.35) we need to introduce the transformation law for the components of a vector operator under a symmetry operation.

Considering a vector operator \vec{O} and a symmetry operation \mathcal{T} , and let \vec{O}' be the vector operator obtained from \vec{O} by applying \mathcal{T} , we have [21]:

$$O'_k \equiv \mathcal{T} O_k \mathcal{T}^+ = \sum_a \Gamma_{ak}(\mathcal{T}) O_a \quad (2.36)$$

where O_k and O'_k are the Cartesian components of \vec{O} and \vec{O}' , respectively, and $\Gamma(\mathcal{T})$ is the matrix representation of the \mathcal{T} operator in the basis spanned by the Cartesian components of the vector operator \vec{O} .

For the case when $\mathcal{T} = S_N^+$, Eq. (2.36) becomes:

$$O'_k \equiv S_N^+ O_k (S_N^+)^+ = S_N^+ O_k S_N = \sum_a \Gamma_{ak} (S_N^+) O_a \quad (2.37)$$

By writing the Eq. (2.37) for the vector components $r_k(\alpha)$, $r_l(\beta)$ and $p_m(\beta)$, and then introducing the obtained equations in Eq. (2.35), we obtain:

$$R_{if}(\mathcal{M}') = \text{Im} \sum_{\alpha, \beta} \sum_{a, b, c} \left[\sum_{k, l, m} \Gamma_{ak} \Gamma_{bl} \Gamma_{cm} \epsilon_{klm} \right] \langle i | r_a(\alpha) | f \rangle \langle f | r_b(\beta) p_c(\beta) | i \rangle \quad (2.38)$$

where Γ_{ak} , Γ_{bl} and Γ_{cm} are elements of the matrix representation $\Gamma(S_N^+)$ of the S_N^+ operator (the inverse of S_N) in the three dimensional (x, y, z) Cartesian basis.

Further, the term $\sum_{k, l, m} \Gamma_{ak} \Gamma_{bl} \Gamma_{cm} \epsilon_{klm}$ in Eq. (2.38) represents the transformation law for the third rank tensor ϵ_{klm} under the S_N^+ symmetry transformation. The Levi-Civita tensor ϵ_{klm} is an axial tensor (also called pseudo-tensor) of third rank. Thus, we have [17]:

$$\epsilon'_{abc} = \det [\Gamma(S_N^+)] \sum_{k, l, m} \Gamma_{ak} \Gamma_{bl} \Gamma_{cm} \epsilon_{klm} = - \sum_{k, l, m} \Gamma_{ak} \Gamma_{bl} \Gamma_{cm} \epsilon_{klm} \quad (2.39)$$

where $\det [\Gamma(S_N^+)] = -1$ is the determinant of the $\Gamma(S_N^+)$ matrix, ϵ_{klm} is the Levi-Civita tensor in the initial coordinate system $Oxyz$, and ϵ'_{abc} is the Levi-Civita tensor in the coordinate system $OXYZ$ that is obtained from $Oxyz$ by applying the operator S_N . Since S_N^+ (also S_N) is an improper rotations, the coordinate systems $Oxyz$ and $OXYZ$ have opposite handedness, e.g. if $Oxyz$ is right handed $OXYZ$ is left handed.

Using Eq. (2.39), Eq. (2.38) becomes:

$$R_{if}(\mathcal{M}') = -\text{Im} \sum_{\alpha, \beta} \sum_{a, b, c} \epsilon'_{abc} \langle i | r_a(\alpha) | f \rangle \langle f | r_b(\beta) p_c(\beta) | i \rangle \quad (2.40)$$

Since for a given combination of the k , l and m indices, the ϵ_{klm} and ϵ'_{klm} symbols take the same values, ϵ'_{klm} can be substituted with ϵ_{klm} in Eqs. (2.40). Then, by also substituting the summation indices a , b and c with k , l and m , respectively, Eq. (2.40) becomes:

$$R_{if}(\mathcal{M}') = -\text{Im} \sum_{\alpha, \beta} \sum_{k, l, m} \epsilon_{klm} \langle i | r_k(\alpha) | f \rangle \langle f | r_l(\beta) p_m(\beta) | i \rangle \quad (2.41)$$

A comparison of the Eqs. (2.31) and (2.41) shows that the molecules \mathcal{M} and \mathcal{M}' have rotational strengths of equal magnitude but opposite sign:

$$R_{if}(\mathcal{M}') = -R_{if}(\mathcal{M}) \quad (2.42)$$

Chiral molecules are molecules that lack an axis of improper rotation (S_N). As a result, the molecules \mathcal{M} and \mathcal{M}' are not identical, they are enantiomers. Thus, Eq. (2.42) states the well known fact that the enantiomers of a chiral molecule (e.g. \mathcal{M} and \mathcal{M}') have rotational strengths of equal magnitude and different signs.

Achiral molecules, on the other hand, have an axis of improper rotation (S_N). As a result, the molecules \mathcal{M} and \mathcal{M}' are identical. Thus, from Eqs. (2.41) it results that achiral molecules have zero rotational strengths, $R = -R = 0$.

Finally, we note that the sign of the rotational strength is determined by the angle ξ between the electric and magnetic dipole transition moments:

$$\cos \xi = \frac{\langle i | \vec{\mu}_E | f \rangle \cdot \text{Im} [\langle f | \vec{\mu}_M | i \rangle]}{|\langle i | \vec{\mu}_E | f \rangle| \cdot |\text{Im} [\langle f | \vec{\mu}_M | i \rangle]|} \quad (2.43)$$

where $|\langle i | \vec{\mu}_E | f \rangle|$ and $|\text{Im} [\langle f | \vec{\mu}_M | i \rangle]|$ are the lengths of the electric and magnetic dipole transition moment vectors, respectively. Thus, $R(i) > 0$ for $\xi < 90^\circ$, whereas for $\xi > 90^\circ$ we have $R(i) < 0$.

In terms of the angle ξ , the two properties of R demonstrated above are written:

$$\mathcal{M} = \text{achiral} \Rightarrow R = 0 \iff \cos \xi_{\text{achiral}} = 0 \Rightarrow \xi_{\text{achiral}} = 90^\circ \quad (2.44)$$

and

$$\mathcal{M} = \text{chiral} \Rightarrow R_R = -R_S \iff \cos \xi_R = -\cos \xi_S \Rightarrow \xi_R = 180^\circ - \xi_S \quad (2.45)$$

where $\xi_R(i)$ and $\xi_S(i)$ are the angles ξ associated with the R and S enantiomers.

Thus, in achiral molecules the total electric and magnetic dipole transition moments are perpendicular, i.e. $\xi = 90^\circ$, whereas in chiral molecules they are in general not perpendicular, i.e. $\xi \neq 90^\circ$.

2.2 Stephens' equations for VCD

As discussed in section 1.3 the determination of absolute configuration of chiral compounds using VCD requires theoretical calculation of VCD spectra. In this section we present a detailed derivation of Stephens' equations for VCD. The approach adopted follows closely Stephen's original derivation [13].

2.2.1 Born-Oppenheimer approximation

The Hamiltonian of an isolated molecule is:

$$H(\vec{r}, \vec{R}) = H_{el}(\vec{r}, \vec{R}) + T_N(\vec{R}) \quad (2.46)$$

where \vec{r} and \vec{R} are electronic and nuclear coordinates, respectively, $H_{el}(\vec{r}, \vec{R})$ is the electronic Hamiltonian, and $T_N(\vec{R})$ is the nuclear kinetic energy operator. The electronic Hamiltonian can be further decomposed in:

$$H_{el}(\vec{r}, \vec{R}) = T_{el}(\vec{r}) + V(\vec{r}, \vec{R}) \quad (2.47)$$

where $T_{el}(\vec{r})$ is the electronic kinetic energy operator, and $V(\vec{r}, \vec{R})$ is the Coulomb potential energy containing the electronic repulsion, the attraction between electrons and nuclei, and the nuclear repulsion.

The Schrödinger equation associated with the Hamiltonian defined in Eq. (2.46) is:

$$H(\vec{r}, \vec{R})\Psi_{Kk}(\vec{r}, \vec{R}) = E_{Kk}\Psi_{Kk}(\vec{r}, \vec{R}) \quad (2.48)$$

where the indexes K and k label electronic and nuclear states, respectively.

Unfortunately, Eq. (2.48) can not be solved analytically even for the simplest molecules, i.e H_2^+ . Thus, simplifying approximations must be introduced in order to carry out a quantum-mechanical treatment of the molecular structures.

The basic approximation, on which the majority of the quantum molecular studies rely, is the Born-Oppenheimer (BO) approximation. The starting point of the BO approximation (BOA) is the large difference between the nuclear and electronic masses, e.g. in the case of the hydrogen atom the ratio of the two is 1837. Consequently, the electrons move much faster than the nuclei and as a result we can separate the electronic and nuclear coordinates by writing the molecular wave function $\Psi_{Kk}(\vec{r}, \vec{R})$ as:

$$\Psi_{Kk}(\vec{r}, \vec{R}) = \psi_K(\vec{r}, \vec{R})\chi_{Kk}(\vec{R}) \quad (2.49)$$

where $\psi_K(\vec{r}, \vec{R})$ is the so-called electronic wave function, and $\chi_{Kk}(\vec{R})$ the so called nuclear wave function. The electronic wave function $\psi_K(\vec{r}, \vec{R})$ describes the electron motion for a fix set of nuclear coordinates R , i.e. $\psi_K(\vec{r}, \vec{R})$ is the solution of the electronic Schrödinger equation:

$$H_{el}(\vec{r}, \vec{R})\psi_K(\vec{r}, \vec{R}) = W_K(\vec{R})\psi_K(\vec{r}, \vec{R}) \quad (2.50)$$

To obtain an equation for the nuclear wave function $\chi_{Kk}(\vec{R})$ we examine the result obtained when acting with the nuclear kinetic-energy operator $T_N(\vec{R})$ on the wave function $\Psi_{Kk}(\vec{r}, \vec{R})$:

$$\begin{aligned} T_N|\Psi_{Kk}\rangle &= -\frac{\hbar^2}{2} \sum_{\lambda} \frac{1}{M_{\lambda}} \nabla_{\lambda}^2 |\psi_K\rangle |\chi_{Kk}\rangle \\ &= -\frac{\hbar^2}{2} \sum_{\lambda} \frac{1}{M_{\lambda}} [|\chi_{Kk}\rangle \nabla_{\lambda}^2 |\psi_K\rangle + 2\nabla_{\lambda} |\psi_K\rangle \nabla_{\lambda} |\chi_{Kk}\rangle + |\psi_K\rangle \nabla_{\lambda}^2 |\chi_{Kk}\rangle] \end{aligned} \quad (2.51)$$

As can be seen in Eq. (2.51), for wave functions $\Psi_{Kk}(\vec{r}, \vec{R})$ that satisfy Eq. (2.49), the nuclear kinetic-energy operator $T_N(\vec{R})$ can be formally written:

$$T_N \equiv -\frac{\hbar^2}{2} \sum_{\lambda} \frac{1}{M_{\lambda}} [\nabla_{\lambda}^2(E) + 2\nabla_{\lambda}(E)\nabla_{\lambda}(N) + \nabla_{\lambda}^2(N)] \quad (2.52)$$

where the index E indicates that the operators ∇_{λ}^2 and ∇_{λ} act on the electronic wave function $\psi_K(\vec{r})$, whereas the index N indicates that the two operators act on the nuclear wave function $\chi_{Kk}(\vec{R})$.

Since the electrons move much faster than the nuclei, we can assume that the electrons readjust their positions instantaneously in response to the nuclear motion, i.e. every instantaneous (fixed) position of the nuclei corresponds to a stationary electronic state. Thus, the first two terms in Eqs. (2.51) and (2.52) can be neglected. As a result the nuclear kinetic energy operator $T_N(\vec{R})$ can be approximated by:

$$T_N(\vec{R}) \simeq T_N^{(0)}(\vec{R}) = -\frac{\hbar^2}{2} \sum_{\lambda} \frac{1}{M_{\lambda}} \nabla_{\lambda}^2(N) \quad (2.53)$$

Using Eqs. (2.46), (2.49) and (2.53) the Schrödinger equation, Eq. (2.48), becomes:

$$[H_{el}(\vec{r}, \vec{R}) + T_N^{(0)}(\vec{R})]\psi_K(\vec{r}, \vec{R})\chi_{Kk}(\vec{R}) = E'_{Kk}(\vec{r}, \vec{R})\psi_K(\vec{r}, \vec{R})\chi_{Kk}(\vec{R}) \quad (2.54)$$

where $E'_{Kk}(\vec{r}, \vec{R})$ is an approximation of the exact eigenvalue E_{Kk} of $H(\vec{r}, \vec{R})$.

Then, using Eqs. (2.50), Eq. (2.54), becomes:

$$\left[T_N^{(0)}(\vec{R}) + W_K(\vec{R})\right]\chi_{Kk}(\vec{R}) = E'_{Kk}(\vec{r}, \vec{R})\chi_{Kk}(\vec{R}) \quad (2.55)$$

Thus, the nuclear wave function $\chi_{Kk}(\vec{R})$ is a solution of Eq. (2.55).

To sum up, the BO approximation is defined by the Eqs. (2.46), (2.49), (2.50) and (2.55), and it consists in solving the Schrödinger equation in two stages. First, we solve the electronic Schrödinger equation obtained by ignoring the nuclear motion, i.e Eq. (2.50). Then, using the average electronic energy obtained in the previous step as the potential for the nuclear motion, the nuclear Schrödinger equation, i.e. Eq. (2.55), is solved.

Vibrational electric and magnetic dipole transition moments

Using the BO wave function, Eq. (2.49), the electric and magnetic dipole transition moments (EDTM and MDTM) of a transition between two vibrational

states, g and e of a non-degenerate electronic state G ($\Psi_{Gg} \rightarrow \Psi_{Ge}$) are:

$$\langle \Psi_{Gg} | \vec{\mu}_E | \Psi_{Ge} \rangle = \langle \chi_{Gg} | \langle \psi_G | \vec{\mu}_E | \psi_G \rangle | \chi_{Ge} \rangle = \langle \chi_{Gg} | \langle \psi_G | \vec{\mu}_E^{el} | \psi_G \rangle + \vec{\mu}_E^{nuc} | \chi_{Ge} \rangle \quad (2.56)$$

$$\langle \Psi_{Gg} | \vec{\mu}_M | \Psi_{Ge} \rangle = \langle \chi_{Gg} | \langle \psi_G | \vec{\mu}_M | \psi_G \rangle | \chi_{Ge} \rangle = \langle \chi_{Gg} | \langle \psi_G | \vec{\mu}_M^{el} | \psi_G \rangle + \vec{\mu}_M^{nuc} | \chi_{Ge} \rangle \quad (2.57)$$

with the operators $\vec{\mu}_E$ and $\vec{\mu}_M$ defined by Eqs. (2.29) and (2.30), respectively.

Since the operator $\vec{\mu}_M^{el}$ is hermitian, the electronic contribution in Eq. (2.57) can be written:

$$\langle \psi_G | \vec{\mu}_M^{el} | \psi_G \rangle = \langle (\vec{\mu}_M^{el})^+ \psi_G | \psi_G \rangle = \langle \vec{\mu}_M^{el} \psi_G | \psi_G \rangle = \langle \psi_G | \vec{\mu}_M^{el} | \psi_G \rangle^* \quad (2.58)$$

The operator $\vec{\mu}_M^{el}$ is purely imaginary, whereas the wave functions Ψ_{Gg} and Ψ_{Ge} may be chosen real. Thus, Eq. (2.58) becomes:

$$\langle \psi_G | \vec{\mu}_M^{el} | \psi_G \rangle = -\langle \psi_G | \vec{\mu}_M^{el} | \psi_G \rangle = 0 \quad (2.59)$$

Thus, as already mentioned, within the BO approximation the electronic contribution to the MDTM is zero. In order to acquire a non-zero contribution from the electrons, it is necessary to use wave functions beyond the adiabatic BO approximations. This will be discussed in section 2.2.2.

The rest of the components of the two dipole transition moments, i.e. electronic and nuclear EDTM, and the nuclear MDTM, do not vanish in the adiabatic BO approximation. As a result, they will be calculated using BO wave functions.

Electronic contribution to the vibrational electric dipole transition moment

We continue with the calculation of the electronic contribution of EDTM. From Eq. (2.56), the β Cartesian component of the electronic contribution of the EDTM is:

$$\langle \Psi_{Gg} | (\vec{\mu}_E^{el})_\beta | \Psi_{Ge} \rangle = \langle \chi_{Gg} | \langle \psi_G | \vec{\mu}_E^{el} | \psi_G \rangle | \chi_{Ge} \rangle \quad (2.60)$$

Expanding the integrand in a Taylor series around the equilibrium position of the nuclei (R^0), we obtain:

$$\langle \psi_G | (\vec{\mu}_E^{el})_\beta | \psi_G \rangle = \langle \psi_G | (\vec{\mu}_E^{el})_\beta | \psi_G \rangle_{R^0} + \sum_{\lambda\alpha} \left(\frac{\partial \langle \psi_G | (\vec{\mu}_E^{el})_\beta | \psi_G \rangle}{\partial R_{\lambda\alpha}} \right)_{R_\lambda^0} (R_{\lambda\alpha} - R_{\lambda\alpha}^0) + \dots \quad (2.61)$$

Introducing Eq. (2.61) in Eq. (2.60), we obtain:

$$\langle \Psi_{Gg} | (\vec{\mu}_E^{el})_\beta | \Psi_{Ge} \rangle = \sum_{\lambda\alpha} \left(\frac{\partial \langle \psi_G | (\vec{\mu}_E^{el})_\beta | \psi_G \rangle}{\partial R_{\lambda\alpha}} \right)_{R_\lambda^0} \langle \chi_{Gg} | (R_{\lambda\alpha} - R_{\lambda\alpha}^0) | \chi_{Ge} \rangle \quad (2.62)$$

where $R_{\lambda\alpha}^0$ is α Cartesian component of the equilibrium position of the nucleus λ . To obtain Eq. (2.62) we made use of the orthogonality of the nuclear wave functions χ_{Gg} and χ_{Ge} .

Eq. (2.62) can be written in a more compact form by introducing the atomic polar tensor (APT). The APT is defined per atom and has electronic and nuclear contributions. The electronic contribution to the APT is defined as:

$$E_{\alpha\beta}^\lambda = \left(\frac{\partial \langle \psi_G | (\vec{\mu}_E^{el})_\beta | \psi_G \rangle}{\partial R_{\lambda\alpha}} \right)_{R_\lambda^0} \quad (2.63)$$

Thus, Eq. (2.62) becomes:

$$\langle \Psi_{Gg} | (\vec{\mu}_E^{el})_\beta | \Psi_{Ge} \rangle = \sum_{\lambda\alpha} E_{\alpha\beta}^\lambda \langle \chi_{Gg} | (R_{\lambda\alpha} - R_{\lambda\alpha}^0) | \chi_{Ge} \rangle \quad (2.64)$$

Nuclear contribution to the vibrational electric dipole transition moments

From Eq. (2.56), the β Cartesian component of the nuclear contribution of the EDTM is given by:

$$\langle \Psi_{Gg} | (\vec{\mu}_E^{nuc})_\beta | \Psi_{Ge} \rangle = \langle \chi_{Gg} | (\vec{\mu}_E^{nuc})_\beta | \chi_{Ge} \rangle \quad (2.65)$$

Expanding $(\vec{\mu}_E^{nuc})_\beta$ in a Taylor series around the equilibrium position of the nuclei (R^0), we obtain:

$$(\vec{\mu}_E^{nuc})_\beta = [(\vec{\mu}_E^{nuc})_\beta]_{R^0} + \sum_{\lambda\alpha} \left[\frac{\partial (\vec{\mu}_E^{nuc})_\beta}{\partial R_{\lambda\alpha}} \right]_{R_\lambda^0} (R_{\lambda\alpha} - R_{\lambda\alpha}^0) + \dots \quad (2.66)$$

Introducing Eq. (2.66) in Eq. (2.65), we obtain:

$$\langle \Psi_{Gg} | (\vec{\mu}_E^{nuc})_\beta | \Psi_{Ge} \rangle = \sum_{\lambda\alpha} \left[\frac{\partial (\vec{\mu}_E^{nuc})_\beta}{\partial R_{\lambda\alpha}} \right]_{R_\lambda^0} \langle \chi_{Gg} | (R_{\lambda\alpha} - R_{\lambda\alpha}^0) | \chi_{Ge} \rangle \quad (2.67)$$

Then, by introducing the nuclear contribution to the APT

$$N_{\alpha\beta}^\lambda = \left[\frac{\partial (\vec{\mu}_E^{nuc})_\beta}{\partial R_{\lambda\alpha}} \right]_{R_\lambda^0} = eZ_\lambda \delta_{\alpha\beta} \quad (2.68)$$

we obtain the following expression for the nuclear contribution of the EDTM:

$$\langle \Psi_{Gg} | (\vec{\mu}_E^{nuc})_\beta | \Psi_{Ge} \rangle = \sum_{\lambda\alpha} N_{\alpha\beta}^\lambda \langle \chi_{Gg} | (R_{\lambda\alpha} - R_{\lambda\alpha}^0) | \chi_{Ge} \rangle \quad (2.69)$$

To obtain the result of Eq. (2.68) we have used the definition of $\vec{\mu}_E^{nuc}$, Eq. (2.7).

Nuclear contribution to the vibrational magnetic dipole transition moment

Unlike the electronic contribution, the nuclear contribution to the MDTM does not vanish within the BOA. Thus, From Eq. (2.57), the β Cartesian component of the nuclear contribution of the MDTM is given by:

$$\langle \Psi_{Gg} | \vec{\mu}_M^{nuc} | \Psi_{Ge} \rangle = \langle \chi_{Gg} | \vec{\mu}_M^{nuc} | \chi_{Ge} \rangle = \sum_{\lambda} \frac{eZ_{\lambda}}{2M_{\lambda}c} \langle \chi_{Gg} | \vec{R}_{\lambda} \times \vec{P}_{\lambda} | \chi_{Ge} \rangle \quad (2.70)$$

where we have used Eq. (2.8).

The nuclear position vector R_{λ} can be written:

$$\vec{R}_{\lambda} = \vec{R}_{\lambda} - \vec{R}_{\lambda}^0 + \vec{R}_{\lambda}^0 = \Delta \vec{R}_{\lambda} + \vec{R}_{\lambda}^0 \quad (2.71)$$

Using Eq. (2.71) the inner product $\vec{R}_{\lambda} \times \vec{P}_{\lambda}$ can be written:

$$\vec{R}_{\lambda} \times \vec{P}_{\lambda} = (\Delta \vec{R}_{\lambda} + \vec{R}_{\lambda}^0) \times \vec{P}_{\lambda} = \Delta \vec{R}_{\lambda} \times \vec{P}_{\lambda} + \vec{R}_{\lambda}^0 \times \vec{P}_{\lambda} = \vec{R}_{\lambda}^0 \times \vec{P}_{\lambda} \quad (2.72)$$

where $\Delta \vec{R}_{\lambda} \times \vec{P}_{\lambda} = 0$ since $\Delta \vec{R}_{\lambda}$ and \vec{P}_{λ} are parallel.

Using Eq. (2.72), Eq. (2.70) becomes:

$$\langle \Psi_{Gg} | \vec{\mu}_M^{nuc} | \Psi_{Ge} \rangle = \sum_{\lambda} \frac{eZ_{\lambda}}{2M_{\lambda}c} \langle \chi_{Gg} | \vec{R}_{\lambda}^0 \times \vec{P}_{\lambda} | \chi_{Ge} \rangle \quad (2.73)$$

Then, for β Cartesian component of $\vec{\mu}_M^{nuc}$, Eq. (2.73) is written:

$$\langle \Psi_{Gg} | (\vec{\mu}_M^{nuc})_{\beta} | \Psi_{Ge} \rangle = \sum_{\lambda\gamma\alpha} \frac{eZ_{\lambda}}{2M_{\lambda}c} \epsilon_{\beta\gamma\alpha} R_{\lambda\gamma}^0 \langle \chi_{Gg} | P_{\lambda\alpha} | \chi_{Ge} \rangle \quad (2.74)$$

where $\epsilon_{\beta\gamma\alpha}$ is the Levi-Civita third rank tensor, and $R_{\lambda\gamma}^0$ and $P_{\lambda\alpha}$ are the γ and α Cartesian components of the vectors \vec{R}_{λ}^0 and \vec{P}_{λ} , respectively.

Using the commutator of the operators $R_{\lambda\alpha}$ and T_N :

$$[R_{\lambda\alpha}, T_N] = R_{\lambda\alpha} T_N - T_N R_{\lambda\alpha} = \frac{\hbar^2}{M_{\lambda}} \nabla_{\lambda\alpha} \quad (2.75)$$

it can be shown that:

$$\langle \chi_{Gg} | P_{\lambda\alpha} | \chi_{Ge} \rangle = -i \frac{M_{\lambda}}{\hbar} (E_{Ge} - E_{Gg}) \langle \chi_{Gg} | R_{\lambda\alpha} - R_{\lambda\alpha}^0 | \chi_{Ge} \rangle \quad (2.76)$$

Proof: From Eq. (2.75), we have:

$$\nabla_{\lambda\alpha} = \frac{M_{\lambda}}{\hbar^2} [R_{\lambda\alpha}, T_N] \quad (2.77)$$

and since $P_{\lambda\delta} = -i\hbar\nabla_{\lambda\delta}$, we have:

$$P_{\lambda\alpha} = -i\frac{M_\lambda}{\hbar}[R_{\lambda\alpha}, T_N] \quad (2.78)$$

Thus, the integral $\langle\chi_{Gg}|P_{\lambda\alpha}|\chi_{Ge}\rangle$, needed in Eq. (2.74), can be written as:

$$\begin{aligned} \langle\chi_{Gg}|P_{\lambda\alpha}|\chi_{Ge}\rangle &= \\ &= -i\frac{M_\lambda}{\hbar}\langle\chi_{Gg}|(R_{\lambda\alpha}T_N - T_N R_{\lambda\alpha})|\chi_{Ge}\rangle \\ &= -i\frac{M_\lambda}{\hbar}(\langle\chi_{Gg}|(R_{\lambda\alpha}T_N|\chi_{Ge}\rangle - \langle\chi_{Gg}|T_N R_{\lambda\alpha}|\chi_{Ge}\rangle) \\ &= -i\frac{M_\lambda}{i\hbar}(\langle\chi_{Gg}|(R_{\lambda\alpha}(T_N + W_G^0)|\chi_{Ge}\rangle - \langle\chi_{Gg}|(T_N + W_G^0)R_{\lambda\alpha}|\chi_{Ge}\rangle) \\ &= -i\frac{M_\lambda}{\hbar}(E_{Ge} - E_{Gg})\langle\chi_{Gg}|(R_{\lambda\alpha}|\chi_{Ge}\rangle \\ &= -i\frac{M_\lambda}{\hbar}(E_{Ge} - E_{Gg})\langle\chi_{Gg}|R_{\lambda\alpha} - R_{\lambda\alpha}^0|\chi_{Ge}\rangle \end{aligned} \quad (2.79)$$

where we have used Eqs. (2.47), (2.48) and (2.50).

Using Eq. (2.79), Eq. (2.74) becomes:

$$\langle\Psi_{Gg}|(\vec{\mu}_M^{nuc})_\beta|\Psi_{Ge}\rangle = -i(E_{Ge} - E_{Gg}) \sum_{\lambda\gamma\alpha} \frac{eZ_\lambda}{2\hbar c} \epsilon_{\beta\gamma\delta} R_{\lambda\gamma}^0 \langle\chi_{Gg}|R_{\lambda\alpha} - R_{\lambda\alpha}^0|\chi_{Ge}\rangle \quad (2.80)$$

Equation (2.80) can be written in a more compact form by introducing the nuclear contribution to the atomic axial tensor (AAT):

$$J_{\alpha\beta}^\lambda = i\frac{eZ_\lambda}{4\hbar c} \sum_{\gamma} \epsilon_{\beta\gamma\alpha} R_{\lambda\gamma}^0 \quad (2.81)$$

Combining, Eqs. (2.80) and (2.81) and we obtain:

$$\langle\Psi_{Gg}|(\vec{\mu}_M^{nuc})_\beta|\Psi_{Ge}\rangle = -2(E_{Ge} - E_{Gg}) \sum_{\lambda\alpha} J_{\alpha\beta}^\lambda \langle\chi_{Gg}|(R_{\lambda\alpha} - R_{\lambda\alpha}^0)|\chi_{Ge}\rangle \quad (2.82)$$

2.2.2 Beyond the Born-Oppenheimer approximation

As discussed in section 2.2.1, in order to obtain non-zero electronic contributions to the MDTM it is necessary to use corrections to the BO wave functions. A corrected BO wave function can be obtained from first order perturbation theory, using the BO wave functions as the zero-order expansion functions and the terms of the nuclear kinetic operator T_N neglected in the BOA as the perturbation Hamiltonian.

From Eq. (2.51)/(2.52), the terms of T_N neglected in the BOA are:

$$T_N^{(1)} = -\frac{\hbar^2}{2} \sum_{\lambda\alpha} \frac{1}{M_\lambda} [\nabla_{\lambda\alpha}^2(E) + 2\nabla_{\lambda\alpha}(E)\nabla_{\lambda\alpha}(N)] \quad (2.83)$$

As before, the index E indicates that the operators ∇_λ^2 and ∇_λ act on the electronic wave function $\psi_K(\vec{r}, \vec{R})$, whereas the index N indicates that the two operators act on the nuclear wave function $\chi_{Kk}(\vec{R})$.

Using the operator $T_N^{(1)}$, a non-BO wave function can be written:

$$\Psi_{Kk}^{cor}(\vec{r}, \vec{R}) = \Psi_{Kk}(\vec{r}, \vec{R}) + \sum_{K'k' \neq Kk} \frac{\langle \Psi_{K'k'} | T_N^{(1)} | \Psi_{Kk} \rangle}{E_{Kk} - E_{K'k'}} \Psi_{K'k'}(\vec{r}, \vec{R}) + \dots \quad (2.84)$$

Electronic contribution to the vibrational magnetic dipole transition moment

Using the corrected BO wave functions of Eq. (2.84), the electronic MDTM associated with the transition $\Psi_{Gg} \rightarrow \Psi_{Ge}$ is given by:

$$\begin{aligned} \langle \Psi_{Gg}^{cor} | \vec{\mu}_M^{el} | \Psi_{Ge}^{cor} \rangle &= \sum_{Kk \neq Ge} \langle \Psi_{Gg} | \vec{\mu}_M^{el} | \Psi_{Kk} \rangle \frac{\langle \Psi_{Kk} | T_N^{(1)} | \Psi_{Ge} \rangle}{E_{Ge} - E_{Kk}} \\ &+ \sum_{Kk \neq Gg} \langle \Psi_{Kk} | \vec{\mu}_M^{el} | \Psi_{Ge} \rangle \frac{\langle \Psi_{Gg} | T_N^{(1)} | \Psi_{Kk} \rangle}{E_{Gg} - E_{Kk}} \end{aligned} \quad (2.85)$$

where we have neglected the second- and higher-order terms.

The first term on the right side of Eq. (2.85) can be further written:

$$\begin{aligned} \sum_{Kk \neq Ge} \langle \Psi_{Gg} | \vec{\mu}_M^{el} | \Psi_{Kk} \rangle \frac{\langle \Psi_{Kk} | T_N^{(1)} | \Psi_{Ge} \rangle}{E_{Ge} - E_{Kk}} &= \\ = \sum_{Kk \neq Ge} \frac{\langle \chi_{Gg} | \langle \psi_G | \vec{\mu}_M^{el} | \psi_K \rangle | \chi_{Kk} \rangle \langle \chi_{Kk} | \langle \psi_K | T_N^{(1)} | \psi_G \rangle | \chi_{Ge} \rangle}{E_{Ge} - E_{Kk}} &= \end{aligned} \quad (2.86)$$

By neglecting the vibrational contribution to the energy difference $E_{Ge} - E_{Kk}$, i.e. $E_{Ge} - E_{Kk} \simeq W_G^0 - W_K^0$, we have:

$$= \sum_{K \neq G} \frac{1}{W_G^0 - W_K^0} \sum_k \langle \chi_{Gg} | \langle \psi_G | \vec{\mu}_M^{el} | \psi_K \rangle | \chi_{Kk} \rangle \langle \chi_{Kk} | \langle \psi_K | T_N^{(1)} | \psi_G \rangle | \chi_{Ge} \rangle = \quad (2.87)$$

where $W_K^0 = W_K(\vec{R}^0)$ and $W_G^0 = W_G(\vec{R}^0)$ are the eigenvalues of the electronic Schrödinger equation, Eq. (2.50), at the nuclear equilibrium position.

Using the closure relation of the density operator, i.e. $\sum_k |\chi_{Kk}\rangle\langle\chi_{Kk}| = 1$, we obtain:

$$= \sum_{K \neq G} \frac{\langle\chi_{Gg}|\langle\psi_G|\vec{\mu}_M^{el}|\psi_K\rangle\langle\psi_K|T_N^{(1)}|\psi_G\rangle|\chi_{Ge}\rangle}{W_G^0 - W_K^0} = \quad (2.88)$$

Further, we explicitly write the operator $T_N^{(1)}$:

$$= -\frac{\hbar^2}{2} \sum_{\lambda\alpha} \frac{1}{M_\lambda} \sum_{K \neq G} \frac{\langle\chi_{Gg}|\langle\psi_G|\vec{\mu}_M^{el}|\psi_K\rangle [\langle\psi_K|\nabla_{\lambda\alpha}^2|\psi_G\rangle + 2\langle\psi_K|\nabla_{\lambda\alpha}|\psi_G\rangle\nabla_{\lambda\alpha}] |\chi_{Ge}\rangle}{W_G^0 - W_K^0} = \quad (2.89)$$

Because the electrons move much faster than the nuclei, it can be considered that the electronic transitions take place for a practically stationary nuclear framework (the Condon approximation). Thus, we expand the electronic wave functions $\psi_G \equiv \psi_G(\vec{r}, \vec{R})$ and $\psi_K \equiv \psi_K(\vec{r}, \vec{R})$ in Taylor series at the equilibrium nuclear positions (\vec{R}^0) and retain only the zero-order terms:

$$\langle\psi_G|\vec{\mu}_M^{el}|\psi_K\rangle \simeq \langle\psi_G|\vec{\mu}_M^{el}|\psi_K\rangle_0 \quad (2.90)$$

$$\langle\psi_G|\nabla_{\lambda\alpha}^2|\psi_K\rangle \simeq \langle\psi_G|\nabla_{\lambda\alpha}^2|\psi_K\rangle_0 \quad (2.91)$$

$$\langle\psi_G|\nabla_{\lambda\alpha}|\psi_K\rangle \simeq \langle\psi_G|\nabla_{\lambda\alpha}|\psi_K\rangle_0 \quad (2.92)$$

Using Eqs. (2.90)–(2.92), Eq. (2.89) becomes:

$$= -\hbar^2 \sum_{\lambda\alpha} \frac{1}{M_\lambda} \sum_{K \neq G} \frac{\langle\psi_G|\vec{\mu}_M^{el}|\psi_K\rangle_0 \langle\psi_K|\nabla_{\lambda\alpha}|\psi_G\rangle_0}{W_G^0 - W_K^0} \langle\chi_{Gg}|\nabla_{\lambda\alpha}|\chi_{Ge}\rangle \quad (2.93)$$

Thus, the first term of Eq. (2.85) can be written:

$$\begin{aligned} & \sum_{Kk \neq Ge} \langle\Psi_{Gg}|\vec{\mu}_M^{el}|\Psi_{Kk}\rangle \frac{\langle\Psi_{Kk}|T_N^{(1)}|\Psi_{Ge}\rangle}{E_{Ge} - E_{Kk}} = \\ & = \sum_{\lambda\alpha} \frac{\hbar^2}{M_\lambda} \sum_{K \neq G} \frac{\langle\psi_G|\vec{\mu}_M^{el}|\psi_K\rangle_0 \langle\psi_K|\nabla_{\lambda\alpha}|\psi_G\rangle_0}{W_G^0 - W_K^0} \langle\chi_{Gg}|\nabla_{\lambda\alpha}|\chi_{Ge}\rangle \end{aligned} \quad (2.94)$$

where we have used $\langle\psi_K|\nabla_{\lambda\alpha}|\psi_G\rangle = -\langle\psi_G|\nabla_{\lambda\alpha}|\psi_K\rangle$ (follows from integration by parts).

Similarly, the second term on the right side of Eq. (2.85) can be written:

$$\begin{aligned} & \sum_{Kk \neq Gg} \langle\Psi_{Kk}|\vec{\mu}_M^{el}|\Psi_{Ge}\rangle \frac{\langle\Psi_{Gg}|T_N^{(1)}|\Psi_{Kk}\rangle}{E_{Gg} - E_{Kk}} = \\ & = \sum_{\lambda\alpha} \frac{\hbar^2}{M_\lambda} \sum_{K \neq G} \frac{\langle\psi_G|\vec{\mu}_M^{el}|\psi_K\rangle_0 \langle\psi_K|\nabla_{\lambda\alpha}|\psi_G\rangle_0}{W_G^0 - W_K^0} \langle\chi_{Gg}|\nabla_{\lambda\alpha}|\chi_{Ge}\rangle \end{aligned} \quad (2.95)$$

where we have used $\langle \psi_K | \vec{\mu}_M^{el} | \psi_G \rangle = -\langle \psi_G | \vec{\mu}_M^{el} | \psi_K \rangle$ (μ_M^{el} is purely complex).

Finally, by adding Eqs. (2.94) and (2.95), (2.85) becomes:

$$\langle \Psi_{Gg}^{cor} | \vec{\mu}_M^{el} | \Psi_{Ge}^{cor} \rangle = 2 \sum_{\lambda\alpha} \frac{\hbar^2}{M_\lambda} \sum_{K \neq G} \frac{\langle \psi_G | \vec{\mu}_M^{el} | \psi_K \rangle_0 \langle \psi_G | \nabla_{\lambda\alpha} | \psi_K \rangle_0}{W_G^0 - W_K^0} \langle \chi_{Gg} | \nabla_{\lambda\alpha} | \chi_{Ge} \rangle \quad (2.96)$$

As Eq. (2.96) shows, the electronic contribution to the MDTM associated to the transition $\Psi_{Gg} \rightarrow \Psi_{Ge}$ obtained using corrected BO wave functions is not zero. However, as can be seen Eq. (2.96) contains a sum over all excited states. This makes the evaluation of Eq. (2.96) very difficult. One needs either to truncate the sum or invoke the energy-average approximation. In both situations the accuracy of the obtained results is undetermined.

2.2.3 Electronic contribution of the atomic axial tensor

In this section, we will show following Stephens's demonstration [13], that the sum over all excited state present in Eq. (2.96) can be contracted exactly.

First, using Eq. (2.79) and the definition of the momentum operator we have:

$$\langle \chi_{Gg} | \nabla_{\lambda\alpha} | \chi_{Ge} \rangle = \frac{M_\lambda}{\hbar^2} (E_{Ge} - E_{Gg}) \langle \chi_{Gg} | R_{\lambda\alpha} - R_{\lambda\alpha}^0 | \chi_{Ge} \rangle \quad (2.97)$$

Then, substituting Eq. (2.97) into Eq. (2.96) we obtain:

$$\begin{aligned} \langle \Psi_{Gg}^{cor} | \vec{\mu}_M^{el} | \Psi_{Ge}^{cor} \rangle &= \\ &= 2(E_{Ge} - E_{Gg}) \sum_{\lambda\alpha} \sum_{K \neq G} \frac{\langle \psi_G | \vec{\mu}_M^{el} | \psi_K \rangle_0 \langle \psi_G | \nabla_{\lambda\alpha} | \psi_K \rangle_0}{W_G^0 - W_K^0} \langle \chi_{Gg} | R_{\lambda\alpha} - R_{\lambda\alpha}^0 | \chi_{Ge} \rangle \end{aligned} \quad (2.98)$$

Nuclear displacement perturbation

The electronic Hamiltonian can be expanded in a Taylor series around the equilibrium nuclear positions:

$$H_{el}(\vec{r}, \vec{R}) = H_{el}(\vec{r}, \vec{R}^0) + \sum_{\lambda\alpha} \left(\frac{\partial H_{el}}{\partial R_{\lambda\alpha}} \right)_0 (R_{\lambda\alpha} - R_{\lambda\alpha}^0) + \dots \quad (2.99)$$

Similarly, the electronic wave function can also be expanded in a Taylor series around the equilibrium nuclear positions:

$$\psi_K(\vec{r}, \vec{R}) = \psi_K(\vec{r}, \vec{R}^0) + \sum_{\lambda\alpha} \left(\frac{\partial \psi_K}{\partial R_{\lambda\alpha}} \right)_0 (R_{\lambda\alpha} - R_{\lambda\alpha}^0) + \dots \quad (2.100)$$

An expansion of the wave function $\psi_K(\vec{r}, \vec{R})$, that is equivalent to the one in Eq. (2.100), can be obtained from standard perturbation theory by using the first order perturbed Hamiltonian in Eq. (2.99):

$$\psi_G(\vec{r}, \vec{R}) = \psi_G(\vec{r}, \vec{R}^0) + \sum_{\lambda\alpha} \sum_{L \neq K} \frac{\langle \psi_L | \frac{\partial H_{el}}{\partial R_{\lambda\alpha}} | \psi_K \rangle_0}{W_K^0 - W_L^0} \psi_L \times (R_{\lambda\alpha} - R_{\lambda\alpha}^0) + \dots \quad (2.101)$$

Comparing Eqs. (2.100) and (2.101) we obtain:

$$\left(\frac{\partial \psi_K}{\partial R_{\lambda\alpha}} \right)_0 = \sum_{L \neq K} \frac{\langle \psi_L | \frac{\partial H_{el}}{\partial R_{\lambda\alpha}} | \psi_K \rangle_0}{W_K^0 - W_L^0} \psi_L \quad (2.102)$$

Using Eq. (2.102), the integral $\langle \psi_G | \nabla_{\lambda} | \psi_K \rangle_0$ can be written:

$$\begin{aligned} \langle \psi_G | \nabla_{\lambda\alpha} | \psi_K \rangle_0 &= \left\langle \psi_G \left| \frac{\partial \psi_K}{\partial R_{\lambda\alpha}} \right|_0 \right\rangle \\ &= \sum_{L \neq K} \frac{\langle \psi_L | \frac{\partial H_{el}}{\partial R_{\lambda\alpha}} | \psi_K \rangle_0}{W_K^0 - W_L^0} \delta_{GL} \\ &= \frac{\langle \psi_G | \frac{\partial H_{el}}{\partial R_{\lambda\alpha}} | \psi_K \rangle_0}{W_K^0 - W_G^0} \end{aligned} \quad (2.103)$$

Substituting the result of Eq. (2.103) in Eq. (2.98) we obtain:

$$\begin{aligned} \langle \Psi_{Gg}^{cor} | \vec{\mu}_M^{el} | \Psi_{Ge}^{cor} \rangle &= \\ &= -2(E_{Ge} - E_{Gg}) \sum_{K \neq G} \sum_{\lambda\alpha} \frac{\langle \psi_G | \vec{\mu}_M^{el} | \psi_K \rangle_0 \langle \psi_G | \frac{\partial H_{el}}{\partial R_{\lambda\alpha}} | \psi_K \rangle_0}{(W_K^0 - W_G^0)^2} \langle \chi_{Gg} | R_{\lambda\alpha} - R_{\lambda\alpha}^0 | \chi_{Ge} \rangle \end{aligned} \quad (2.104)$$

Magnetic field perturbation

Following the procedure used in the previous section (but for the case of a magnetic field perturbation), in this section, we will obtain an expression for the first-order perturbed wave function due to a magnetic field perturbation. The first-order perturbed Hamiltonian associated to a uniform magnetic field H_β along the direction β is:

$$H^{(1)} = -(\mu_M)_\beta H_\beta \quad (2.105)$$

An exact wave function of the perturbed system can be formally written $\psi_G(\vec{r}, \vec{R}, H_\beta)$. By expanding $\psi_G(\vec{r}, \vec{R}, H_\beta)$ taken at the equilibrium nuclear position, $\psi_G(\vec{r}, \vec{R}^0, H_\beta)$, in Taylor series we obtain:

$$\psi_G(\vec{r}, \vec{R}^0, H_\beta) = \psi_G(\vec{r}, \vec{R}^0) + \left(\frac{\partial \psi_G}{\partial H_\beta} \right)_0 H_\beta + \dots \quad (2.106)$$

From standard perturbation theory we have:

$$\psi_G(\vec{r}, \vec{R}^0, H_\beta) = \psi_G(\vec{r}, \vec{R}^0) + \sum_{L \neq K} \frac{-\langle \psi_L | (\mu_M)_\beta | \psi_G \rangle_0}{W_K^0 - W_L^0} \psi_L H_\beta + \dots \quad (2.107)$$

Comparing Eqs. (2.106) and (2.107) we obtain:

$$\left(\frac{\partial \psi_G}{\partial H_\beta} \right)_0 = - \sum_{L \neq K} \frac{\langle \psi_L | (\mu_M)_\beta | \psi_G \rangle_0}{W_K^0 - W_L^0} \psi_L \quad (2.108)$$

Now that we have obtained expressions for the first order perturbed wave functions due to a nuclear displacement and magnetic field perturbations, we continue the calculation of the electronic contribution of the vibrational MDTM by calculating their overlap:

$$\begin{aligned} \left\langle \left(\frac{\partial \psi_G}{\partial R_{\lambda\alpha}} \right)_0 \middle| \left(\frac{\partial \psi_G}{\partial H_\beta} \right)_0 \right\rangle &= - \sum_{K \neq G} \sum_{L \neq G} \frac{\langle \psi_K | \frac{\partial H_{el}}{\partial R_{\lambda\alpha}} | \psi_G \rangle_0^* \langle \psi_K | (\mu_M)_\beta | \psi_G \rangle_0}{(W_G^0 - W_K^0)^2} \delta_{KL} \\ &= \sum_{K \neq G} \frac{\langle \psi_G | \frac{\partial H_{el}}{\partial R_{\lambda\alpha}} | \psi_K \rangle_0 \langle \psi_G | (\mu_M)_\beta | \psi_K \rangle_0}{(W_G^0 - W_K^0)^2} \\ &= \sum_{K \neq G} \frac{\langle \psi_G | (\mu_M)_\beta | \psi_K \rangle_0 \langle \psi_K | \frac{\partial H_{el}}{\partial R_{\lambda\alpha}} | \psi_G \rangle_0}{(W_G^0 - W_K^0)^2} \end{aligned} \quad (2.109)$$

Comparing the result of Eq. (2.109) to Eq. (2.104) we obtain:

$$\begin{aligned} \langle \Psi_{Gg}^{cor} | (\vec{\mu}_M^{el})_\beta | \Psi_{Ge}^{cor} \rangle &= \\ &= -2(E_{Ge} - E_{Gg}) \sum_{\lambda\alpha} \left\langle \left(\frac{\partial \psi_G}{\partial R_{\lambda\alpha}} \right)_0 \middle| \left(\frac{\partial \psi_G}{\partial H_\beta} \right)_0 \right\rangle \langle \chi_{Gg} | R_{\lambda\alpha} - R_{\lambda\alpha}^0 | \chi_{Ge} \rangle \end{aligned} \quad (2.110)$$

In contrast to Eq. (2.96), which contains a sum over all excited states, Eq. (2.110) involves only the electronic wave function of ground state (ψ_G).

Finally, by introducing the electronic contribution of the atomic axial tensor:

$$I_{\alpha\beta}^\lambda = \left\langle \left(\frac{\partial \psi_G}{\partial R_{\lambda\alpha}} \right)_0 \middle| \left(\frac{\partial \psi_G}{\partial H_\beta} \right)_0 \right\rangle \quad (2.111)$$

Eq. (2.110) becomes:

$$\langle \Psi_{Gg}^{cor} | (\vec{\mu}_M^{el})_\beta | \Psi_{Ge}^{cor} \rangle = -2(E_{Ge} - E_{Gg}) \sum_{\lambda\alpha} I_{\alpha\beta}^\lambda \langle \chi_{Gg} | R_{\lambda\alpha} - R_{\lambda\alpha}^0 | \chi_{Ge} \rangle \quad (2.112)$$

2.2.4 The harmonic approximation

We start from the nuclear Schrödinger equation:

$$\left[T_N^{(0)}(\vec{R}) + W_K(\vec{R}) \right] \chi_{Kk}(\vec{R}) = E'_{Kk}(\vec{r}, \vec{R}) \chi_{Kk}(\vec{R}) \quad (2.113)$$

The potential energy $W_K(R)$ is the eigenvalue of the electronic Schrödinger equation, i.e. Eq. (2.50), and as discussed in section 2.2.1 when Eq. (2.113) was first introduced it depends parametrically on the nuclear coordinates \vec{R} . Assuming that the nuclei oscillations around their equilibrium positions (\vec{R}^0) are small, the potential energy $W_K(R)$ can be approximated by a Taylor expansion at \vec{R}^0 :

$$W_K(\vec{R}) \simeq W_K(\vec{R}^0) + \sum_{\lambda\alpha} \left(\frac{\partial W_K}{\partial R_{\lambda\alpha}} \right)_{\vec{R}^0} \Delta R_{\lambda\alpha} + \frac{1}{2} \sum_{\lambda\alpha, \sigma\beta} \left(\frac{\partial^2 W_K}{\partial R_{\lambda\alpha} \partial R_{\sigma\beta}} \right)_{\vec{R}^0} \Delta R_{\lambda\alpha} \Delta R_{\sigma\beta} + \dots \quad (2.114)$$

with $\Delta R_{\lambda\alpha} = R_{\lambda\alpha} - R_{\lambda\alpha}^0$ and $\Delta R_{\sigma\beta} = R_{\sigma\beta} - R_{\sigma\beta}^0$, the indices λ and σ label nuclei, whereas α and β labels Cartesian coordinates.

The first term on the right side of Eq. (2.114), i.e. $W_K(\vec{R}^0)$, can be neglected since it simply adds a constant to the potential energy (we are not interested in the absolute value of the potential energy). The second term of Eq. (2.114), i.e. $\left(\frac{\partial W_K}{\partial R_{\lambda\alpha}} \right)_{\vec{R}^0}$ is also zero since it represents the gradient of the potential energy evaluated at the equilibrium geometry (where the energy curve goes through a minimum). The higher terms in the Taylor expansion can also be neglected provided that the displacements from the equilibrium (ΔR) are small (which is our initial assumption). Thus, the potential energy $W_K(R)$ can be approximated by a quadratic potential:

$$W_K(\vec{R}) \simeq \frac{1}{2} \sum_{\lambda\alpha, \sigma\beta} \left(\frac{\partial^2 W_K}{\partial R_{\lambda\alpha} \partial R_{\sigma\beta}} \right)_{\vec{R}^0} \Delta R_{\lambda\alpha} \Delta R_{\sigma\beta} \equiv \frac{1}{2} \mathbf{R}^+ \mathbf{F} \mathbf{R} \quad (2.115)$$

where \mathbf{R} is a $3N_\lambda$ -dimensional column vector with $\Delta R_{\lambda\alpha}$ as its components, \mathbf{R}^+ is the transpose of \mathbf{R} (a row vector), and \mathbf{F} is the so called force constant (or Hessian) matrix, i.e. the $3N_\lambda \times 3N_\lambda$ square matrix of elements $\left(\frac{\partial^2 W_K}{\partial R_{\lambda\alpha} \partial R_{\sigma\beta}} \right)_{\vec{R}^0}$, N_λ is the number of nuclei of the molecule.

Inserting Eq. (2.115) in Eq. (2.113) we obtain:

$$\left[-\frac{1}{2} \sum_{\lambda} \frac{\hbar^2}{M_{\lambda}} \frac{\partial^2}{\partial R_{\lambda\alpha}^2} + \frac{1}{2} \mathbf{R}^+ \mathbf{F} \mathbf{R} \right] \chi_{Kk}(\vec{R}) = E'_{Kk}(\vec{r}, \vec{R}) \chi_{Kk}(\vec{R}) \quad (2.116)$$

Equation (2.116) is written in Cartesian coordinates. By transforming to a new coordinate system in which the matrix F is diagonal, Eq. (2.116) is decomposed

into a set of $3N_\lambda$ Schrödinger equations for the harmonic oscillator for which the solutions are known.

First, we introduce the so called mass weighted coordinates (q_i):

$$q_i = \sqrt{M_\lambda} \Delta R_{\lambda\alpha} \quad (2.117)$$

In matrix notation, Eq. (2.117) is written:

$$\mathbf{q} = \mathbf{M}^{\frac{1}{2}} \mathbf{R} \quad (2.118)$$

where \mathbf{q} and \mathbf{R} are $3N_\lambda$ -dimensional column vectors and $\mathbf{M}^{\frac{1}{2}}$ is a $3N_\lambda \times 3N_\lambda$ diagonal matrix of diagonal elements: $M_{ii}^{\frac{1}{2}} = M_{i+1i+1}^{\frac{1}{2}} = M_{i+2i+2}^{\frac{1}{2}} = \sqrt{M_i}$ with $i = 3j + 1$ and $j = 0, N_\lambda - 1$.

Using Eqs. (2.117) and (2.118), Eq. (2.116) can be written:

$$\left[-\frac{\hbar^2}{2} \sum_i \frac{\partial^2}{\partial q_i^2} + \frac{1}{2} \mathbf{q}^+ \mathbf{G} \mathbf{q} \right] \chi_{Kk}(\vec{R}) = E'_{Kk}(\vec{r}, \vec{R}) \chi_{Kk}(\vec{R}) \quad (2.119)$$

where $\mathbf{G} = (\mathbf{M}^{-\frac{1}{2}})^+ \mathbf{F} \mathbf{M}^{-\frac{1}{2}}$ is the so called mass weighted Hessian and $M^{-\frac{1}{2}}$ is the inverse of matrix $M^{\frac{1}{2}}$. As the matrix \mathbf{G} is symmetric (since \mathbf{F} is symmetric):

$$G_{ij} = \frac{F_{ij}}{\sqrt{M_i M_j}} = \frac{F_{ji}}{\sqrt{M_j M_i}} = G_{ji} \quad (2.120)$$

there exists a unitary matrix \mathbf{U} , i.e. $\mathbf{U}^+ \mathbf{U} = \mathbf{I}$ that diagonalises \mathbf{G} :

$$\mathbf{U}^+ \mathbf{G} \mathbf{U} = \mathbf{\Lambda} \quad (2.121)$$

where $\mathbf{\Lambda}$ is a diagonal matrix.

Using \mathbf{U} , we define the normal mode coordinates \mathbf{Q} :

$$\mathbf{q} = \mathbf{U} \mathbf{Q} \quad (2.122)$$

In normal modes coordinates, Eq. (2.119) becomes:

$$\left[-\frac{\hbar^2}{2} \sum_i \frac{\partial^2}{\partial Q_i^2} + \frac{1}{2} \sum_i \Lambda_{ii} Q_i^2 \right] \chi_{Kk}(\vec{R}) = E'_{Kk}(\vec{r}, \vec{R}) \chi_{Kk}(\vec{R}) \quad (2.123)$$

which as already mentioned can be separated into $3N_\lambda$ equations for one-dimensional harmonic oscillators:

$$\left[-\frac{\hbar^2}{2} \frac{\partial^2}{\partial Q_i^2} + \frac{1}{2} \Lambda_{ii} Q_i^2 \right] \phi_{k_i}(Q_i) = E_{k_i}(i) \phi_{k_i}(Q_i), \quad i = 1, 3N_\lambda \quad (2.124)$$

where $E_{k_i}(i)$ and $\phi_{k_i}(Q_i)$ are the eigenvalues and the eigenfunctions associated to the normal mode Q_i . The orthonormal eigenfunctions $\phi_{k_i}(Q_i)$ of Eq. (2.124) are [22]:

$$\phi_{k_i}(Q_i) = N_{k_i}(i) H_{k_i}(\gamma_i Q_i) e^{-\frac{1}{2}\gamma_i^2 Q_i^2} \quad (2.125)$$

with

$$N_{k_i}(i) = \left[\frac{\gamma_i}{2^{k_i} (k_i!) \sqrt{\pi}} \right]^{\frac{1}{2}} \quad \text{and} \quad \gamma_i = \left(\frac{2\pi\nu_i}{\hbar} \right)^{\frac{1}{2}} \quad (2.126)$$

where H_k are the Hermite polynomials and ν_i is the frequency of the normal mode i . The eigenvalues of Eq. (2.124) are [22]:

$$E_{k_i}(i) = \left(k_i + \frac{1}{2} \right) h\nu_i \quad (2.127)$$

The eigenfunctions and eigenvalues of Eq. (2.123) can be expressed in terms of the solutions of Eq. (2.124):

$$\chi_{Kk} = \phi_{k_1}(Q_1) \phi_{k_2}(Q_2) \cdots \phi_{k_{3N}}(Q_{3N}) = \prod_i \phi_{k_i}(Q_i) \quad \text{and} \quad E'_{Kk} = \sum_i E_{k_i}(i) \quad (2.128)$$

Finally, we note that by combining Eqs. (2.118) and (2.122) the Cartesian nuclear displacements, \mathbf{R} , can be connected to the normal modes coordinates \mathbf{Q} :

$$\mathbf{R} = \mathbf{M}^{-\frac{1}{2}} \mathbf{U} \mathbf{Q} = \mathbf{S} \mathbf{Q} \quad (2.129)$$

where \mathbf{U} are the eigenvectors of the mass weighted Hessian (\mathbf{G}) and $\mathbf{S} = \mathbf{M}^{-\frac{1}{2}} \mathbf{U}$.

Equations (2.128) and Eq. (2.129) will be used in the next section to derive final expressions for Stephens' equations for VCD.

Stephens' equations for VCD in the harmonic approximation

From Eq (2.26), the rotational strength associated to the transition between the vibrational states g and e of an electronic state G , $|\chi_{Gg}\rangle \rightarrow |\chi_{Ge}\rangle$, is given by:

$$R(|\chi_{Gg}\rangle \rightarrow |\chi_{Ge}\rangle) = \text{Im} \left[\langle \chi_{Gg} | \vec{\mu}_E | \chi_{Ge} \rangle \cdot \langle \chi_{Gg} | \vec{\mu}_M | \chi_{Ge} \rangle \right] \quad (2.130)$$

From Eqs. (2.64), (2.69), (2.82) and (2.112), the EDTM and MDTM associated to the $|\chi_{Gg}\rangle \rightarrow |\chi_{Ge}\rangle$ transition can be written:

$$\langle \chi_{Gg} | (\vec{\mu}_E)_\beta | \chi_{Ge} \rangle = \sum_{\lambda\alpha} P_{\alpha\beta}^\lambda \langle \chi_{Gg} | \Delta R_{\lambda\alpha} | \chi_{Ge} \rangle \quad (2.131)$$

$$\langle \chi_{Gg} | (\vec{\mu}_M)_\beta | \chi_{Ge} \rangle = -2(E_{Ge} - E_{Gg}) \sum_{\lambda\alpha} A_{\alpha\beta}^\lambda \langle \chi_{Gg} | \Delta R_{\lambda\alpha} | \chi_{Ge} \rangle \quad (2.132)$$

where $P_{\alpha\beta}^\lambda$ is the atomic polar tensor (APT), $A_{\alpha\beta}^\lambda$ is the atomic axial tensor (AAT), the summation indices λ and α run over nuclei and Cartesian components, respectively, and $|\chi_{Gg}\rangle$ and $|\chi_{Ge}\rangle$ are nuclear wave functions associated with the electronic state G and the vibrational levels g and e , respectively.

As already mentioned, the APTs and AATs are defined per atom and have electronic and nuclear contributions:

$$P_{\alpha\beta}^\lambda = E_{\alpha\beta}^\lambda + N_{\alpha\beta}^\lambda \quad (2.133)$$

$$A_{\alpha\beta}^\lambda = I_{\alpha\beta}^\lambda + J_{\alpha\beta}^\lambda \quad (2.134)$$

where the electronic ($E_{\alpha\beta}^\lambda$ and $I_{\alpha\beta}^\lambda$) and the nuclear ($N_{\alpha\beta}^\lambda$ and $J_{\alpha\beta}^\lambda$) contributions of the atomic polar and axial tensors have been defined in Eqs. (2.63), (2.111), (2.68) and (2.81), respectively.

Using Eq. (2.129) and the expression of χ_{Kk} given in Eq. (2.128), the integral $\langle\chi_{Gg}|\Delta R_{\lambda\alpha}|\chi_{Ge}\rangle$ needed in Eqs. (2.131) and (2.132) becomes:

$$\begin{aligned} \langle\chi_{Gg}|\Delta R_{\lambda\alpha}|\chi_{Ge}\rangle &= \sum_i S_{\alpha,i}^\lambda \langle\chi_{Gg}|Q_i|\chi_{Ge}\rangle \\ &= \sum_i S_{\alpha,i}^\lambda \left\langle \prod_j \phi_{g_j}(Q_j) | Q_i | \prod_j \phi_{e_j}(Q_j) \right\rangle \\ &= \sum_i S_{\alpha,i}^\lambda \langle\phi_{g_i}(Q_i)|Q_i|\phi_{e_i}(Q_i)\rangle \prod_{j \neq i} \delta_{g_j e_j} \end{aligned} \quad (2.135)$$

Then, using the recursion formula for the Hermite polynomials [22]:

$$H_{k_i+1}(\gamma_i Q_i) = 2\gamma_i Q_i H_{k_i}(\gamma_i Q_i) - 2k_i H_{k_i-1}(\gamma_i Q_i) \quad (2.136)$$

together with Eqs (2.125) and (2.126), and the orthogonality of the $\phi_{k_i}(i)$ wave functions, it can be shown that:

$$\langle\phi_{g_i}(i)|Q_i|\phi_{e_i}(i)\rangle = \frac{1}{\gamma_i} \left(\sqrt{\frac{e_i+1}{2}} \delta_{g_i(e_i+1)} + \sqrt{\frac{e_i}{2}} \delta_{g_i(e_i-1)} \right) \quad (2.137)$$

Inserting the result of Eq. (2.137) in Eq. (2.135) we obtain:

$$\langle\chi_{Gg}|\Delta R_{\lambda\alpha}|\chi_{Ge}\rangle = \frac{1}{\gamma_i} \sum_i S_{\alpha,i}^\lambda \left(\sqrt{\frac{e_i+1}{2}} \delta_{g_i(e_i+1)} + \sqrt{\frac{e_i}{2}} \delta_{g_i(e_i-1)} \right) \prod_{j \neq i} \delta_{g_j e_j} \quad (2.138)$$

Then, by substituting Eq. (2.138) with Eqs. (2.131) and (2.132), and considering only the fundamental transition of the mode i ($g_i = 0$, $e_i = 1$ and $g_j = e_j$ for

$j \neq i$), Eqs. (2.131) and (2.132) become:

$$\langle \chi_{G0} | (\vec{\mu}_E)_\beta | \chi_{G1} \rangle_i \equiv \langle 0 | (\vec{\mu}_E)_\beta | 1 \rangle_i = \left(\frac{\hbar}{2\omega_i} \right)^{\frac{1}{2}} \sum_{\lambda\alpha} S_{\alpha,i}^\lambda P_{\alpha\beta}^\lambda \quad (2.139)$$

$$\langle \chi_{G0} | (\vec{\mu}_M)_\beta | \chi_{G1} \rangle_i \equiv \langle 0 | (\vec{\mu}_M)_\beta | 1 \rangle_i = -(2\hbar\omega_i)^{\frac{1}{2}} \sum_{\lambda\alpha} S_{\alpha,i}^\lambda A_{\alpha\beta}^\lambda \quad (2.140)$$

where $\omega_i = 2\pi\nu_i$ is the angular frequency.

2.2.5 Stephens' equations for VCD: summary

As shown in the previous section, Eqs (2.139) and (2.140), within the harmonic approximation the electric and magnetic dipole transition moments associated with the fundamental transition $|0\rangle \rightarrow |1\rangle$ of the i^{th} vibrational mode can be written:

$$\langle 0 | (\vec{\mu}_E)_\beta | 1 \rangle_i = \left(\frac{\hbar}{\omega_i} \right)^{\frac{1}{2}} \sum_{\lambda\alpha} P_{\alpha\beta}^\lambda S_{\lambda\alpha,i} \quad (2.141)$$

$$\langle 0 | (\vec{\mu}_M)_\beta | 1 \rangle_i = -(2\hbar^3\omega_i)^{\frac{1}{2}} \sum_{\lambda\alpha} A_{\alpha\beta}^\lambda S_{\lambda\alpha,i} \quad (2.142)$$

where $\vec{\mu}_E$ and $\vec{\mu}_M$ are the electric and magnetic dipole moment operators.

The rotational strength (R) for the fundamental transition $|0\rangle \rightarrow |1\rangle$ of the i^{th} vibrational mode is then given by:

$$R(0 \rightarrow 1)_i = \text{Im} [\langle 0 | \vec{\mu}_E | 1 \rangle_i \cdot \langle 1 | \vec{\mu}_M | 0 \rangle_i] \quad (2.143)$$

Furthermore, from Eqs (2.141) and (2.142), the total electric and magnetic transition dipole moments can be written as sums of atomic contributions:

$$\vec{E}_{01}(i) \equiv \langle 0 | (\vec{\mu}_E)_\beta | 1 \rangle_i = \sum_{\lambda} \vec{E}_{01}^\lambda(i), \quad \vec{M}_{10}(i) \equiv \langle 0 | (\vec{\mu}_M)_\beta | 1 \rangle_i = \sum_{\lambda} \vec{M}_{10}^\lambda(i) \quad (2.144)$$

The atomic contributions are:

$$\left(\vec{E}_{01}^\lambda \right)_\beta(i) = \left(\frac{\hbar}{\omega_i} \right)^{\frac{1}{2}} \sum_{\alpha} \vec{S}_\alpha^\lambda(i) P_{\alpha\beta}^\lambda \quad (2.145)$$

$$\left(\vec{M}_{10}^\lambda \right)_\beta(i) = -(2\hbar^3\omega_i)^{\frac{1}{2}} \sum_{\alpha} \vec{S}_\alpha^\lambda(i) A_{\alpha\beta}^\lambda \quad (2.146)$$

In Eqs. (2.141) to (2.146), $S_{\lambda\alpha,i}$ is the transformation matrix from Cartesian to normal coordinates, $P_{\alpha\beta}^\lambda$ and $A_{\alpha\beta}^\lambda$ are APT and the AAT, respectively, \hbar is the

reduced Planck constant, ω_i is the frequency of the i^{th} vibrational mode, α and β denote Cartesian coordinates, and λ labels the nuclei. Both tensors, APT and AAT, are defined per atom and have electronic ($E_{\alpha\beta}^\lambda$ and $I_{\alpha\beta}^\lambda$) and nuclear ($N_{\alpha\beta}^\lambda$ and $J_{\alpha\beta}^\lambda$) contributions:

$$P_{\alpha\beta}^\lambda = E_{\alpha\beta}^\lambda + N_{\alpha\beta}^\lambda \quad (2.147)$$

$$A_{\alpha\beta}^\lambda = I_{\alpha\beta}^\lambda + J_{\alpha\beta}^\lambda \quad (2.148)$$

From Eqs. (2.63) to (2.68), the components of the APTs are:

$$N_{\alpha\beta}^\lambda = eZ_\lambda \delta_{\alpha\beta} \quad (2.149)$$

$$E_{\alpha\beta}^\lambda = \left(\frac{\partial \langle \psi_G(\mathbf{R}) | (\vec{\mu}_E)_\beta | \psi_G(\mathbf{R}) \rangle}{\partial R_{\lambda\alpha}} \right)_{\mathbf{R}^0} \quad (2.150)$$

The components of the AATs, first introduced in Eqs. (2.81) to (2.111), are:

$$J_{\alpha\beta}^\lambda = i \frac{eZ_\lambda}{4\hbar c} \sum_{\gamma} \epsilon_{\beta\gamma\alpha} R_{\lambda\gamma}^0 \quad (2.151)$$

$$I_{\alpha\beta}^\lambda = \left\langle \left(\frac{\partial \psi_G(\mathbf{R})}{\partial R_{\lambda\alpha}} \right)_{\mathbf{R}^0} \left| \left(\frac{\partial \psi_G(\mathbf{R}^0, \mathbf{H})}{\partial H_\beta} \right)_{\mathbf{H}=0} \right. \right\rangle \quad (2.152)$$

In Eqs. (2.149) to (2.152), ψ_G is the electronic wave function of the ground state G , Z_λ and \mathbf{R}_λ are the charge and the position of nucleus λ , \mathbf{R}_λ^0 is \mathbf{R}_λ at the equilibrium geometry, \mathbf{H} is a static magnetic field, $\epsilon_{\alpha\beta\gamma}$ is the Levi-Civita tensor with the indices α, β, γ running over Cartesian components, e is the elementary charge and c is the speed of light in vacuum. In Eq. (2.152), $\Psi_G(\mathbf{R})$ depends on the positions of the nuclei, which are not fixed, while $\Psi_G(\mathbf{R}^0, \mathbf{H})$ has to be calculated for the equilibrium positions of the nuclei in the presence of a magnetic field. To generalize, with regard to the notation used in this chapter, a quantity Γ depends on a parameter/perturbation y only when it is written as $\Gamma(y)$. Otherwise it refers to the unperturbed case.

The APTs are origin-independent [20], whereas the AATs are origin-dependent by definition. The origin-dependence of the AATs is given by [20]:

$$(A_{\alpha\beta}^\lambda)^{\mathbf{O}_1} = (A_{\alpha\beta}^\lambda)^{\mathbf{O}_2} + \frac{i}{4\hbar c} \sum_{\gamma\delta} \epsilon_{\beta\gamma\delta} Y_\gamma P_{\alpha\delta}^\lambda \quad (2.153)$$

where \mathbf{O}_1 and \mathbf{O}_2 are the position vectors of the two different choices of the origin of coordinate system, while \mathbf{Y} is the displacement vector between the two origins ($\mathbf{Y} = \mathbf{O}_2 - \mathbf{O}_1$). Stephens has shown that if the calculated AATs and APTs fulfill Eq. (2.153) the calculated rotational strengths are origin independent [20].

By defining the following tensors:

$$\Sigma_{\alpha\beta}^1 = 4\hbar c \sum_{\lambda} \text{Im} (A_{\alpha\beta}^{\lambda}) \quad (2.154)$$

$$\Sigma_{\alpha\beta}^2 = \sum_{\lambda\gamma\delta} \epsilon_{\beta\gamma\delta} R_{\lambda\gamma}^0 P_{\alpha\delta}^{\lambda} \quad (2.155)$$

$$\Sigma_{\alpha\beta}^3 = \sum_{\gamma} \epsilon_{\alpha\beta\gamma} (\mu^G)_{\gamma} \quad (2.156)$$

$$\Sigma_{\alpha\beta}^4 = \sum_{\lambda} P_{\alpha\beta}^{\lambda} \quad (2.157)$$

it can be shown that the APTs and AATs are further interconnected via sum rules. In Eq. (2.156), μ_{γ}^G is the γ Cartesian component of the dipole moment of the ground state. For neutral systems and exact wave functions these tensors obey the following sum rules [23]:

$$\Sigma_{\alpha\beta}^1 = \Sigma_{\alpha\beta}^2 = \Sigma_{\alpha\beta}^3, \quad \Sigma_{\alpha\beta}^4 = 0 \quad (2.158)$$

Chapter 3

Implementation of Stephens' equations for VCD in the ADF program package

3.1 Introduction

The aim of this chapter is to describe and validate the implementation of Stephens' equations for VCD [13] in the Amsterdam Density Functional (ADF) program package [24–26]. The ADF package is a Fortran code based on the Kohn-Sham approach to Density-Functional Theory (DFT). It uses Slater-type orbitals (STO) as basis functions and numerical integration throughout. This has consequences for the used algorithms, such as a density fit for the Coulomb potential and subsequent evaluation of the Coulomb potential on the grid. The numerical integration is carried out using a highly optimized and very efficient numerical scheme [27] based on a three-dimensional grid partitioned into Voronoi cells [28]. To speed up the calculations, the numerical integration and the generation of grid points are parallelized. Other features of ADF that further increase its efficiency are the use of frozen cores and extensive molecular symmetry.

As shown in the previous chapter, the VCD intensities are proportional to the rotational strengths. For exact wave functions and for approximate wave functions expanded in a complete one-electron basis, rotational strengths obtained from Stephens' equations for VCD are origin independent [20]. For finite basis sets, the calculations are not necessarily gauge independent. We note that this gauge dependence problem is not specific to VCD, all calculations involving quantities related to external magnetic fields suffer from it [29]. As London has shown [30], the origin-dependence problem is overcome by using magnetic-

field-dependent orbitals, the so called London atomic orbitals (LAO) or gauge including atomic orbitals (GIAO).

This chapter is organized as follows: first we derive implementable expressions for the atomic polar and axial tensors (APT and AAT) in terms of STOs and LAOs, respectively, and discuss their implementation. Then, we demonstrate that the numerical integration used in ADF [27, 28] does not affect the origin-independence of the rotational strengths. Further, the accuracy of the calculated AATs and APTs is assessed via sum rules for a range of systematically increased STO basis sets. Finally, the VCD spectra predicted with ADF are compared with experimental VCD spectra and also with VCD spectra from the literature that were obtained with the B3PW91 and B3LYP functionals. The chapter is finalized with some concluding remarks.

3.2 Implementation

We start by writing the APTs and AATs in terms of Kohn–Sham molecular orbitals (MO). After introducing the coupled-perturbed Kohn–Sham equations (CPKS) the final expressions for APTs and AATs are derived and their implementation is discussed. Only the electronic contributions will be considered since the implementation of the nuclear parts, Eqs. (2.149) and (2.151), is trivial.

When the electronic wave function, ψ_G , is approximated by a single Slater determinant, the electronic components of the APTs ($E_{\alpha\beta}^\lambda$) and of the AATs ($I_{\alpha\beta}^\lambda$), defined in Eqs. (2.150) and (2.152), respectively, become [31]:

$$\begin{aligned} E_{\alpha\beta}^\lambda &= \left(\frac{\partial}{\partial R_{\lambda\alpha}} \int \mathbf{r}_\beta \rho \, d\mathbf{r} \right)_{\mathbf{R}^0} \\ &= \int \mathbf{r}_\beta \left(\frac{\partial \rho}{\partial R_{\lambda\alpha}} \right)_{\mathbf{R}^0} d\mathbf{r} = \int \mathbf{r}_\beta \rho^{(1), R_{\lambda\alpha}} d\mathbf{r} \end{aligned} \quad (3.1)$$

$$I_{\alpha\beta}^\lambda = 2 \sum_{j=1}^{N_{\text{occ}}} \left\langle \left(\frac{\partial \varphi_j}{\partial R_{\lambda\alpha}} \right)_{\mathbf{R}^0} \left| \left(\frac{\partial \varphi_j}{\partial H_\beta} \right)_{\mathbf{H}=0} \right. \right\rangle \quad (3.2)$$

with:

$$\rho = 2 \sum_{j=1}^{N_{\text{occ}}} \varphi_j \varphi_j^* \quad \text{and} \quad \rho^{(1)} = 2 \sum_{j=1}^{N_{\text{occ}}} \left(\varphi_j^{(1)} \varphi_j^* + \varphi_j \varphi_j^{(1)*} \right) \quad (3.3)$$

Here, φ_j is the j^{th} MO, ρ and $\rho^{(1), R_{\lambda\alpha}}$ are the electron density and its derivative with respect to a nuclear displacement, respectively, \mathbf{r} is a spatial coordinate, j runs over the occupied MOs, and N_{occ} is the number of occupied MOs. Note that Eqs. (3.2) and (3.3) are written for the case of a closed-shell system. Throughout

this chapter the upper index “(1)” denotes first order derivatives with respect to some perturbation parameter y .

According to the CPKS formalism the first order derivative of an MO with respect to a perturbation y can be written as [32, 33]:

$$\varphi^{(1)} = \chi^{(1)}\mathbf{C} + \varphi\mathbf{U}^{(1)} \quad (3.4)$$

In Eq. (3.4) φ is a row vector containing the MOs, χ is a row vector containing the perturbation-dependent basis functions and \mathbf{U} is the unitary transformation that relates the perturbed eigenvectors to the unperturbed ones [32, 33]:

$$\mathbf{C}(y) = \mathbf{C}\mathbf{U}(y) \quad (3.5)$$

The elements of the $\mathbf{U}^{(1)}$ matrix required in Eq. (3.4) are solutions of the CPKS equations [32, 33]:

$$U_{ij}^{(1)} = \frac{F_{ij}^{(1)} - \epsilon_j S_{ij}^{(1)}}{\epsilon_j - \epsilon_i} \quad (i \neq j), \quad U_{ii}^{(1)} = -\frac{1}{2}S_{ii}^{(1)} \quad (3.6)$$

$$U_{ij}^{(1)} + U_{ji}^{(1)*} + S_{ij}^{(1)} = 0 \quad (3.7)$$

where \mathbf{S} and \mathbf{F} are the overlap and Fock matrices in the MO basis, respectively, and ϵ_i, ϵ_j denote orbital energies.

3.2.1 Expression for the atomic axial tensor

The electronic contribution to the atomic axial tensor, Eq. (3.2), is an overlap integral of two first-order perturbed wave functions. One perturbation is due to a nuclear displacement, the other is due to the magnetic field.

From Eq. (3.4) the derivatives of the j^{th} MO can be written:

$$\varphi_j^{(1)} = \sum_{a=1}^{N_{\text{bas}}} \chi_a^{(1)} C_{aj} + \sum_{i=1}^{N_{\text{MO}}} \varphi_i U_{ij}^{(1)} \quad (3.8)$$

where N_{bas} is the number of basis functions and N_{MO} is the number of MOs.

By inserting Eq. (3.8) written for magnetic and nuclear displacement pertur-

bations into Eq. (3.2) we obtain:

$$\begin{aligned}
I_{\alpha\beta}^{\lambda} = & \sum_{j=1}^{N_{\text{occ}}} \sum_{a,b=1}^{N_{\text{bas}}} C_{aj} C_{bj} \langle \chi_a^{(1),R_{\lambda\alpha}} | \chi_b^{(1),H_{\beta}} \rangle \\
& + \sum_{j=1}^{N_{\text{occ}}} \sum_{i'=1}^{N_{\text{MO}}} \sum_{a=1}^{N_{\text{bas}}} C_{aj} U_{i'j}^{(1),H_{\beta}} \langle \chi_a^{(1),R_{\lambda\alpha}} | \varphi_{i'} \rangle \\
& + \sum_{j=1}^{N_{\text{occ}}} \sum_{i=1}^{N_{\text{MO}}} \sum_{b=1}^{N_{\text{bas}}} U_{ij}^{(1),R_{\lambda\alpha}} C_{bj} \langle \varphi_i | \chi_b^{(1),H_{\beta}} \rangle \\
& + \sum_{j=1}^{N_{\text{occ}}} \sum_{i,i'=1}^{N_{\text{MO}}} U_{ij}^{(1),R_{\lambda\alpha}} U_{i'j}^{(1),H_{\beta}} \langle \varphi_i | \varphi_{i'} \rangle
\end{aligned} \tag{3.9}$$

In Eq. (3.9) the upper indexes $R_{\lambda\alpha}$ and H_{β} label the nuclear displacement and magnetic field perturbations with respect to which the derivatives were taken.

Finally, by writing the MOs as linear combinations of the basis functions, and also using the orthogonality of the MOs, i.e. $\langle \varphi_i | \varphi_{i'} \rangle = \delta_{ii'}$, we obtain:

$$\begin{aligned}
I_{\alpha\beta}^{\lambda} = & \sum_{j=1}^{N_{\text{occ}}} \sum_{a,b=1}^{N_{\text{bas}}} C_{aj} C_{bj} \langle \chi_a^{(1),R_{\lambda\alpha}} | \chi_b^{(1),H_{\beta}} \rangle \\
& + \sum_{j=1}^{N_{\text{occ}}} \sum_{i=1}^{N_{\text{MO}}} \sum_{a,b=1}^{N_{\text{bas}}} C_{aj} C_{bi} U_{ij}^{(1),H_{\beta}} \langle \chi_a^{(1),R_{\lambda\alpha}} | \chi_b \rangle \\
& + \sum_{j=1}^{N_{\text{occ}}} \sum_{i=1}^{N_{\text{MO}}} \sum_{a,b=1}^{N_{\text{bas}}} C_{ai} C_{bj} U_{ij}^{(1),R_{\lambda\alpha}} \langle \chi_a | \chi_b^{(1),H_{\beta}} \rangle \\
& + \sum_{j=1}^{N_{\text{occ}}} \sum_{i=1}^{N_{\text{MO}}} U_{ij}^{(1),R_{\lambda\alpha}} U_{ij}^{(1),H_{\beta}}
\end{aligned} \tag{3.10}$$

As can be seen from Eq. (3.10), the calculation of the electronic contribution to the AATs requires knowledge of the unitary matrices $\mathbf{U}^{(1),R_{\lambda\alpha}}$ and $\mathbf{U}^{(1),H_{\beta}}$, including their occupied–occupied (occ–occ) blocks, the unperturbed eigenvectors (\mathbf{C}), and the integrals $\langle \chi_a^{(1),R_{\lambda\alpha}} | \chi_b^{(1),H_{\beta}} \rangle$, $\langle \chi_a^{(1),R_{\lambda\alpha}} | \chi_b \rangle$, and $\langle \chi_a | \chi_b^{(1),H_{\beta}} \rangle$.

As already mentioned, the matrices $\mathbf{U}^{(1),R_{\lambda\alpha}}$ and $\mathbf{U}^{(1),H_{\beta}}$ are solutions of the CPKS equations for magnetic field perturbations and nuclear displacements, respectively. The methodologies used to solve the CPKS equations for magnetic field and nuclear displacement perturbations are described in sections 3.2.3 and 3.2.4, respectively.

The integrals $\langle \chi_a^{(1),R_{\lambda\alpha}} | \chi_b^{(1),H_{\beta}} \rangle$, $\langle \chi_a^{(1),R_{\lambda\alpha}} | \chi_b \rangle$, and $\langle \chi_a | \chi_b^{(1),H_{\beta}} \rangle$ are calculated numerically using London atomic orbitals (LAO) as basis functions. An LAO is

obtained from a field independent basis function by adding a phase factor that depends on the magnetic field [29, 34–36]:

$$\sigma_a^A(\mathbf{r}) = \chi_a^A(\mathbf{r}) \cdot \exp \left[-i \frac{e}{\hbar c} (\mathbf{H} \times \mathbf{R}_A) \mathbf{r} \right] \quad (3.11)$$

where A labels the nucleus on which the basis function χ_a^A is centered, \mathbf{H} is a static magnetic field and \mathbf{R}_A is the position vector of the A^{th} nucleus. (In our case the function χ_a^A is an STO.)

For a zero magnetic field an LAO reduces to an STO and therefore only quantities directly related to a magnetic field, i.e. $U_{ij}^{(1),H_\beta}$ and $\chi_b^{(1),H_\beta}$, are calculated using LAOs.

3.2.2 Expression for the atomic polar tensor

From Eq. (3.1) the electronic contribution of the APT, $E_{\alpha\beta}^\lambda$, depends on the first-order density due to a nuclear displacement perturbation $\rho^{(1),R_{\lambda\alpha}}$. Inserting Eq. (3.8) into the expression of the $\rho^{(1),R_{\lambda\alpha}}$ given in Eq. (3.3) and making use of the condition Eq. (3.7) we obtain:

$$\begin{aligned} \rho^{(1),R_{\lambda\alpha}} = & \sum_{i=1}^{N_{\text{vir}}} \sum_{j=1}^{N_{\text{occ}}} \left(U_{ij}^{(1),R_{\lambda\alpha}*} \varphi_i^* \varphi_j + U_{ij}^{(1),R_{\lambda\alpha}} \varphi_i \varphi_j^* \right) \\ & + \sum_{j=1}^{N_{\text{occ}}} \sum_{a=1}^{N_{\text{bas}}} (C_{aj} \varphi_j^* + C_{aj}^* \varphi_j) \chi_a^{(1),R_{\lambda\alpha}} \\ & - \sum_{i=1}^{N_{\text{occ}}} \sum_{j=1}^{N_{\text{occ}}} S_{ji}^{(1),R_{\lambda\alpha}} \varphi_i^* \varphi_j \end{aligned} \quad (3.12)$$

Inserting this into Eq. (3.1) gives

$$\begin{aligned} E_{\alpha\beta}^\lambda = & \sum_{i=1}^{N_{\text{vir}}} \sum_{j=1}^{N_{\text{occ}}} U_{ij}^{(1),R_{\lambda\alpha}*} \langle \varphi_i | \mathbf{r}_\beta | \varphi_j \rangle \\ & + \sum_{i=1}^{N_{\text{vir}}} \sum_{j=1}^{N_{\text{occ}}} U_{ij}^{(1),R_{\lambda\alpha}} \langle \varphi_j | \mathbf{r}_\beta | \varphi_i \rangle \\ & + \sum_{j=1}^{N_{\text{occ}}} \sum_{a=1}^{N_{\text{bas}}} C_{aj}^* \langle \chi_a^{(1),R_{\lambda\alpha}} | \mathbf{r}_\beta | \varphi_j \rangle \\ & + \sum_{j=1}^{N_{\text{occ}}} \sum_{a=1}^{N_{\text{bas}}} C_{aj} \langle \varphi_j | \mathbf{r}_\beta | \chi_a^{(1),R_{\lambda\alpha}} \rangle \\ & - \sum_{i=1}^{N_{\text{occ}}} \sum_{j=1}^{N_{\text{occ}}} S_{ji}^{(1),R_{\lambda\alpha}} \langle \varphi_i | \mathbf{r}_\beta | \varphi_j \rangle \end{aligned} \quad (3.13)$$

Thus, from Eq. (3.13) the calculation of the electronic contribution of the APTs, $E_{\alpha\beta}^\lambda$, requires knowledge of the unitary matrix $\mathbf{U}^{(1),R_{\lambda\alpha}}$ (without the occ-occ block), the unperturbed eigenvectors (\mathbf{C}), the first order perturbed overlap matrix $S^{(1),R_{\lambda\alpha}}$, and the integrals $\langle\varphi_i|\mathbf{r}_\beta|\varphi_j\rangle$, $\langle\varphi_j|\mathbf{r}_\beta|\varphi_i\rangle$, $\langle\chi_a^{(1),R_{\lambda\alpha}}|\mathbf{r}_\beta|\varphi_j\rangle$ and $\langle\varphi_j|\mathbf{r}_\beta|\chi_a^{(1),R_{\lambda\alpha}}\rangle$. All these quantities are calculated numerically using STOs.

3.2.3 Calculation of the $\mathbf{U}^{(1),R_{\lambda\alpha}}$ matrix

In general, the CPKS equations, Eqs. (3.6) and (3.7), have to be solved in an iterative manner due to the fact that the $\mathbf{U}^{(1)}$ matrix depends on the first order perturbed Fock matrix, $\mathbf{F}^{(1)}$, which depends on the first order density, $\rho^{(1)}$, which in turn depends on the $\mathbf{U}^{(1)}$ matrix.

The one-electron Kohn–Sham operator (h) is:

$$\begin{aligned} h &= T + V_{Ne} + V_C + V_{XC} \\ &= -\frac{p^2}{2} - \sum_A \frac{Z_A}{|\mathbf{r} - \mathbf{R}_A|} + \int \frac{\rho}{|\mathbf{r} - \mathbf{r}'|} d\mathbf{r}' + V_{XC} \end{aligned} \quad (3.14)$$

where the first term is the kinetic energy, the second is the nuclear potential, the third is the electronic Coulomb potential, and the last term is the exchange–correlation potential. The derivative of one-electron Kohn–Sham operator h with respect to a nuclear displacement, $R_{\lambda\alpha}$, is:

$$h^{(1),R_{\lambda\alpha}} = \frac{\partial V_{Ne}}{\partial R_{\lambda\alpha}} + \int \frac{\rho^{(1),R_{\lambda\alpha}}}{|\mathbf{r} - \mathbf{r}'|} d\mathbf{r}' + \frac{\partial V_{XC}}{\partial R_{\lambda\alpha}} \quad (3.15)$$

Inserting Eq. (3.12) into the above expression gives an expression for $h^{(1),R_{\lambda\alpha}}$ that can be split into a part that contains the $U^{(1),R_{\lambda\alpha}}$ and a part that does not, so that $F_{ij}^{(1),R_{\lambda\alpha}}$ of Eq. (3.6) can be written as:

$$F_{ij}^{(1),R_{\lambda\alpha}} = F_{ij}(U^{(1),R_{\lambda\alpha}}) + F_{ij}(\text{non} - U^{(1),R_{\lambda\alpha}}) \quad (3.16)$$

Putting this into Eq. (3.6) gives

$$U_{ij}^{(1),R_{\lambda\alpha}} = \frac{F_{ij}(U^{(1),R_{\lambda\alpha}})}{\epsilon_j - \epsilon_i} + \frac{F_{ij}(\text{non} - U^{(1),R_{\lambda\alpha}}) - \epsilon_i S_{ij}^{(1),R_{\lambda\alpha}}}{\epsilon_j - \epsilon_i} \quad (3.17)$$

This equation has the “matrix” form

$$\mathbf{u} = \mathbf{A}(\mathbf{u}) + \mathbf{v}, \quad (3.18)$$

where \mathbf{u} is a vector with components $U_{ij}^{(1),R_{\lambda\alpha}}$, the matrix \mathbf{A} depends on \mathbf{u} , and \mathbf{v} is a vector independent of the $U_{ij}^{(1),R_{\lambda\alpha}}$. Eq. (3.18) is solved using an iterative method [32, 33, 37].

3.2.4 Calculation of the $\mathbf{U}^{(1),\mathbf{H}_\beta}$ matrix

The first order perturbation Hamiltonian for a magnetic field perturbation, $H^{(1),H_\beta}$, is purely imaginary [35]:

$$H^{(1),H_\beta} = -iH_\beta \left(\frac{\vec{r}}{2} \times \vec{\nabla} \right)_\beta \quad (3.19)$$

Thus, from standard perturbation theory it follows that the first-order perturbed MOs, $\varphi^{(1),H_\beta}$, are purely imaginary too. Since the unperturbed MOs, φ_i , can be chosen to be real, the first order density $\rho^{(1),H_\beta}$ becomes:

$$\begin{aligned} \rho^{(1),H_\beta} &= \sum_i^{occ} \left\{ \varphi_i^* \varphi_i^{(1),H_\beta} + \varphi_i \left[\varphi_i^{(1),H_\beta} \right]^* \right\} \\ &= \sum_i^{occ} \left[\varphi_i \varphi_i^{(1),H_\beta} - \varphi_i \varphi_i^{(1),H_\beta} \right] = 0 \end{aligned} \quad (3.20)$$

As can be seen from Eq. (3.20), the first order density $\rho^{(1),H_\beta}$ is zero. Thus, for magnetic field perturbations the first-order perturbed Fock matrix, $\mathbf{F}^{(1),H_\beta}$, does not depend on the $\mathbf{U}^{(1),H_\beta}$ matrix (see discussion in the beginning of section 3.2.3). As a result $\mathbf{U}^{(1),H_\beta}$ can be calculated directly from Eq. (3.6), no iterative procedure is needed.

3.2.5 Contributions to the AATs from the occ–occ blocks of the $\mathbf{U}^{(1),\mathbf{H}_\beta}$ and $\mathbf{U}^{(1),\mathbf{R}_{\lambda\alpha}}$ matrices

As mentioned in section 3.2.1, the occ–occ blocks of both $\mathbf{U}^{(1),\mathbf{R}_{\lambda\alpha}}$ and $\mathbf{U}^{(1),\mathbf{H}_\beta}$ are required for the calculations of the electronic contributions of the AATs ($I_{\alpha\beta}^\lambda$). This is because the basis sets depend on the perturbation. For degenerate orbitals, the denominator in the expression for off-diagonal occ–occ matrix elements in Eq. (3.6) will diverge causing numerical problems. However, as will be shown in this section, the contributions from the off-diagonal matrix elements of the occ–occ blocks can be expressed in terms of the perturbed overlap matrices thereby avoiding any complication.

In the case of a magnetic field perturbation the first-order perturbed Hamiltonian and the first-order perturbed MOs are purely complex. Thus, the first-order perturbed Fock and overlap matrix elements are purely complex too, and satisfy the following relations:

$$F_{ij}^{(1),H_\beta} = -F_{ji}^{(1),H_\beta}, \quad S_{ij}^{(1),H_\beta} = -S_{ji}^{(1),H_\beta} \quad (3.21)$$

Since $F_{ij}^{(1),H\beta}$ and $S_{ij}^{(1),H\beta}$ are purely complex, the matrix elements $U_{ij}^{(1),H\beta}$ are purely complex too (see Eq. 3.6).

When the perturbation is a nuclear displacement, the first-order perturbed Hamiltonian and the first-order perturbed MOs are real, so that:

$$F_{ij}^{(1),R\lambda\alpha} = F_{ji}^{(1),R\lambda\alpha}, \quad S_{ij}^{(1),R\lambda\alpha} = S_{ji}^{(1),R\lambda\alpha} \quad (3.22)$$

Thus, from Eq. (3.6) results that the matrix elements $U_{ij}^{(1),R\lambda\alpha}$ are also real.

To obtain Eqs. (3.21) and (3.22) we have used the Hermiticity property of the perturbed Hamiltonians and the fact that the unperturbed MOs are real.

As can be seen, the last three terms in Eq. (3.10) depend on the $\mathbf{U}^{(1)}$ matrices including their occ-occ blocks. The components of the second and third terms in Eq. (3.10) associated to the i and j occupied MOs ($i \neq j$) are:

$$\begin{aligned} & U_{ij}^{(1),H\beta} \sum_{a,b=1}^{N_{\text{bas}}} C_{aj} C_{bi} \langle \chi_a^{(1),R\lambda\alpha} | \chi_b \rangle + U_{ij}^{(1),R\lambda\alpha} \sum_{a,b=1}^{N_{\text{bas}}} C_{ai} C_{bj} \langle \chi_a | \chi_b^{(1),H\beta} \rangle \\ & + U_{ji}^{(1),H\beta} \sum_{a,b=1}^{N_{\text{bas}}} C_{ai} C_{bj} \langle \chi_a^{(1),R\lambda\alpha} | \chi_b \rangle + U_{ji}^{(1),R\lambda\alpha} \sum_{a,b=1}^{N_{\text{bas}}} C_{aj} C_{bi} \langle \chi_a | \chi_b^{(1),H\beta} \rangle \end{aligned} \quad (3.23)$$

For nuclear displacement perturbations the basis sets are of STO type and therefore $\chi_k^{(1),R\lambda\alpha}$ and χ_l are both real (k, l are either a or b). Thus:

$$\langle \chi_k^{(1),R\lambda\alpha} | \chi_l \rangle = \langle \chi_l | \chi_k^{(1),R\lambda\alpha} \rangle \quad (3.24)$$

For magnetic field perturbation the basis sets are of LAO type. From Eq. (3.11) the derivative of an LAO with respect to a magnetic field, $\chi_m^{(1),H\beta}$, (m is either a or b) is given by:

$$\frac{\partial \sigma_m^A}{\partial H_\beta} = \chi_m^{(1),H\beta} = -i(r \times R_A) \chi_m \quad (3.25)$$

where we have used atomic units ($\frac{e}{\hbar c} = 1$).

Since χ_m is real (it is an STO), $\chi_m^{(1),H\beta}$ is purely imaginary. Thus, we have:

$$\langle \chi_{a,b}^{(1),H\beta} | \chi_{a,b} \rangle = -\langle \chi_{a,b} | \chi_{a,b}^{(1),H\beta} \rangle \quad (3.26)$$

By interchanging the summation indices a and b in the third and fourth terms of Eq. (3.23) and using Eq. (3.24) and Eq. (3.26), Eq. (3.23) becomes :

$$\begin{aligned} & U_{ij}^{(1),H\beta} \sum_{a,b=1}^{N_{\text{bas}}} C_{aj} C_{bi} \langle \chi_a^{(1),R\lambda\alpha} | \chi_b \rangle + U_{ij}^{(1),R\lambda\alpha} \sum_{a,b=1}^{N_{\text{bas}}} C_{ai} C_{bj} \langle \chi_a | \chi_b^{(1),H\beta} \rangle + \\ & + U_{ji}^{(1),H\beta} \sum_{a,b=1}^{N_{\text{bas}}} C_{aj} C_{bi} \langle \chi_a | \chi_b^{(1),R\lambda\alpha} \rangle - U_{ji}^{(1),R\lambda\alpha} \sum_{a,b=1}^{N_{\text{bas}}} C_{ai} C_{bj} \langle \chi_a^{(1),H\beta} | \chi_b \rangle \end{aligned} \quad (3.27)$$

Furthermore, we express $U_{ij}^{(1),H\beta}$ and $U_{ij}^{(1),R\lambda\alpha}$ in Eq. (3.27) using Eq. (3.7):

$$\begin{aligned} & \left[-U_{ji}^{(1),H\beta*} - S_{ij}^{(1),H\beta} \right] \sum_{a,b=1}^{N_{\text{bas}}} C_{aj} C_{bi} \langle \chi_a^{(1),R\lambda\alpha} | \chi_b \rangle \\ & + \left[-U_{ji}^{(1),R\lambda\alpha*} - S_{ij}^{(1),R\lambda\alpha} \right] \sum_{a,b=1}^{N_{\text{bas}}} C_{ai} C_{bj} \langle \chi_a | \chi_b^{(1),H\beta} \rangle \\ & + U_{ji}^{(1),H\beta} \sum_{a,b=1}^{N_{\text{bas}}} C_{aj} C_{bi} \langle \chi_a | \chi_b^{(1),R\lambda\alpha} \rangle - U_{ji}^{(1),R\lambda\alpha} \sum_{a,b=1}^{N_{\text{bas}}} C_{ai} C_{bj} \langle \chi_a^{(1),H\beta} | \chi_b \rangle \end{aligned} \quad (3.28)$$

Collecting the terms that have the same $U^{(1)}$ matrix elements, we obtain:

$$\begin{aligned} & -U_{ji}^{(1),H\beta*} \sum_{a,b=1}^{N_{\text{bas}}} C_{aj} C_{bi} \left[\langle \chi_a^{(1),R\lambda\alpha} | \chi_b \rangle + \langle \chi_a | \chi_b^{(1),R\lambda\alpha} \rangle \right] \\ & -U_{ji}^{(1),R\lambda\alpha*} \sum_{a,b=1}^{N_{\text{bas}}} C_{ai} C_{bj} \left[\langle \chi_a^{(1),H\beta} | \chi_b \rangle + \langle \chi_a | \chi_b^{(1),H\beta} \rangle \right] \\ & -S_{ij}^{(1),H\beta} \sum_{a,b=1}^{N_{\text{bas}}} C_{aj} C_{bi} \langle \chi_a^{(1),R\lambda\alpha} | \chi_b \rangle - S_{ij}^{(1),R\lambda\alpha} \sum_{a,b=1}^{N_{\text{bas}}} C_{ai} C_{bj} \langle \chi_a | \chi_b^{(1),H\beta} \rangle \end{aligned} \quad (3.29)$$

The summations in the first two terms of Eq. (3.29) are the $S_{ji}^{(1),R\lambda\alpha}$ and $S_{ij}^{(1),H\beta}$ matrix elements, respectively. Thus, Eq. (3.29) becomes:

$$\begin{aligned} & -U_{ji}^{(1),H\beta*} S_{ji}^{(1),R\lambda\alpha} - U_{ji}^{(1),R\lambda\alpha*} S_{ij}^{(1),H\beta} \\ & -S_{ij}^{(1),H\beta} \sum_{a,b=1}^{N_{\text{bas}}} C_{aj} C_{bi} \langle \chi_a^{(1),R\lambda\alpha} | \chi_b \rangle - S_{ij}^{(1),R\lambda\alpha} \sum_{a,b=1}^{N_{\text{bas}}} C_{ai} C_{bj} \langle \chi_a | \chi_b^{(1),H\beta} \rangle \end{aligned} \quad (3.30)$$

Next we will consider the components of the fourth term of Eq. (3.10) associated with the same pair of indices i and j . After putting the fourth components in a convenient form, we will return to Eq. (3.30). Thus, using Eq. (3.7), the components of the fourth term of Eq. (3.10) associated to a pair of occupied MOs labeled i and j , can be written:

$$\begin{aligned} & U_{ij}^{(1),R\lambda\alpha} U_{ij}^{(1),H\beta} + U_{ji}^{(1),R\lambda\alpha} U_{ji}^{(1),H\beta} = \\ & = U_{ij}^{(1),R\lambda\alpha} U_{ij}^{(1),H\beta} + (-U_{ij}^{(1),R\lambda\alpha*} - S_{ji}^{(1),R\lambda\alpha})(-U_{ij}^{(1),H\beta*} - S_{ji}^{(1),H\beta}) = \\ & = U_{ij}^{(1),R\lambda\alpha*} S_{ji}^{(1),H\beta} + S_{ji}^{(1),R\lambda\alpha} U_{ij}^{(1),H\beta*} + S_{ji}^{(1),R\lambda\alpha} S_{ji}^{(1),H\beta} \end{aligned} \quad (3.31)$$

To obtain Eq. (3.31) we have used $U_{ij}^{(1),R\lambda\alpha} U_{ij}^{(1),H\beta} + U_{ij}^{(1),R\lambda\alpha*} U_{ij}^{(1),H\beta*} = 0$, which is a consequence of the facts that $U^{(1),H\beta}$ is purely complex and $U^{(1),R\lambda\alpha}$ is real.

By adding the results of Eqs. (3.30) and (3.31) we obtain the final expression for the contributions to $I_{\alpha\beta}^{\lambda}$ from the last three terms of Eq. (3.10) due to a pair of occ-occ MOs i and j :

$$-S_{ji}^{(1),R_{\lambda\alpha}} S_{ji}^{(1),H_{\beta}} - S_{ij}^{(1),H_{\beta}} \sum_{a,b=1}^{N_{\text{bas}}} C_{aj} C_{bi} \langle \chi_a^{(1),R_{\lambda\alpha}} | \chi_b \rangle - S_{ij}^{(1),R_{\lambda\alpha}} \sum_{a,b=1}^{N_{\text{bas}}} C_{ai} C_{bj} \langle \chi_a | \chi_b^{(1),H_{\beta}} \rangle \quad (3.32)$$

As can be seen from Eq. (3.32), the off-diagonal matrix elements of the occ-occ blocks of both $U^{(1)}$ matrices are not needed for the calculation of the electronic contribution to the atomic axial tensor ($I_{\alpha\beta}^{\lambda}$).

We note that for the occ-occ block of $U^{(1)}$ matrix, the equation (3.7) is not equivalent to $U_{ij}^{(1)} = -\frac{1}{2}S_{ij}^{(1)}$ and $U_{ji}^{(1)*} = -\frac{1}{2}S_{ij}^{(1)}$. However, by substituting these expressions for the occ-occ blocks of the two $U^{(1)}$ matrices in Eq. (3.10), and then considering the components of the last three terms of Eq. (3.10) associated with a pair of occupied MOs i and j (like we did in this subsection), one re-obtains Eq. (3.32). Thus, in order to avoid any numerical complications, the off-diagonal elements of the occ-occ blocks of both $U^{(1)}$ matrices, $U_{ij}^{(1),R_{\lambda\alpha}}$ and $U_{ij}^{(1),H_{\beta}}$ (i and j run over occupied MOs), are set to $-\frac{1}{2}S_{ij}^{(1),R_{\lambda\alpha}}$ and $-\frac{1}{2}S_{ij}^{(1),H_{\beta}}$, respectively in the program.

3.3 Validation for a set of benchmark molecules

The theory presented in sections 2.2.4 and 3.2 has been implemented in the ADF program. The AATs, $\mathbf{U}^{(1),H_{\beta}}$ and rotational strengths are calculated with the newly developed VCD module of ADF, while the APTs, $\mathbf{U}^{(1),R_{\lambda}}$ and $\mathbf{S}_{\lambda\alpha,i}$ are calculated with the existing Second Derivatives (SD) module of ADF [37]. The validation of the implementation is done in two ways. First, using Eqs. (2.153) and (2.158) we examine the accuracy of the calculated tensors using ethylene oxide (oxirane) (**1**) as our test molecule. Second, we compare calculated rotational strengths with the experimental values for two benchmark molecules: α -pinene (**2**) and Troger's base (**3**). (Schematic representations of the test molecules are shown in Fig. 3.1.)

The calculations were performed using three different exchange-correlation functionals (BP86 [38, 39], OLYP [40, 41], and BLYP [38, 42]) and basis sets from the ADF basis set library. The basis sets used were SZ, DZ, DZP, TZP, TZ2P and ET-pVQZ [43]. The geometries were optimized separately for each choice of functional and basis set using the optimizer described in reference [44].

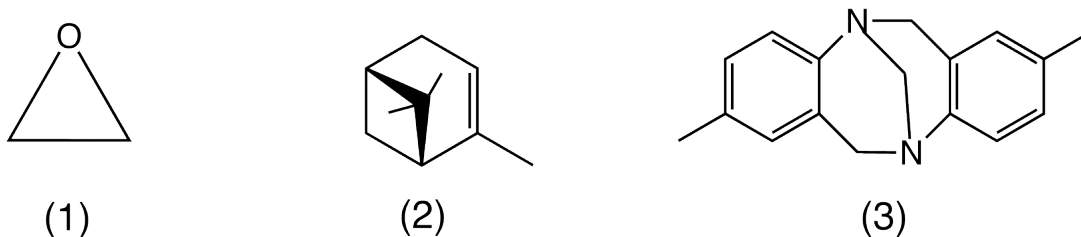


Figure 3.1: Schematic representation of the test molecules used to verify the VCD implementation: Oxirane (1), α -pinene (2), Troger's base (3).

Very tight convergence criteria have been applied for the geometry optimization (10^{-6} Hartree for the energy and 10^{-4} Hartree/Ångstrom for the gradients).

3.3.1 The Atomic Axial Tensors

Gauge dependence

Rotational strengths should be origin-independent. Historically this has been an issue [36, 45–48]. Initially, the importance of using London atomic orbitals was not fully recognized. The failure to use LAOs combined with the use of basis sets of limited size and/or different levels of theory for the computation of the AATs, APTs and force fields yielded rotational strengths that were origin-dependent. As an attempt to remedy this problem the distributed origin (DO) gauge was introduced [20]. In the DO gauge the AAT of each nucleus is calculated with respect to an origin centred at that nucleus. Then using the shift formula of Eq. (2.153), they are referred to a common origin \mathbf{O}_1 . Since this does not yield correct results when LAO's are not used, the results still prove to be dependent on the choice of origin \mathbf{O}_1 , although they generally yielded results of superior accuracy compared to the ones obtained when using the common origin (CO) gauge [45, 46].

Bak *et al.* have proven that when LAOs are used, Eq. (2.153) is satisfied at any basis set level [36] and therefore the calculated rotational strengths are origin-independent [20]. Still, numerical error sources, such as numerical integration of STO-based integrals and/or the limited accuracy of $\mathbf{U}^{(1)}$ matrices may prevent perfect independency of the choice of origin. We therefore verify the degree of origin-independency of our implementation by calculating the AATs with respect to the CO gauge and the DO gauge with origins at nuclei. In the CO gauge the AATs are calculated from Eq. (2.148) using Eq. (2.151) and Eq. (2.152); the origin of the coordinate system was chosen at the molecular center of mass (CM). In the DO gauge with origins at the nuclei, the AATs are calculated with respect

Basis Set			SZ			
$M_{\alpha\beta}^\lambda$	$(M_{\alpha\beta}^\lambda)^{CM,CO}$			$(M_{\alpha\beta}^\lambda)^{CM,DO}$		
$M_{\alpha\beta}^1$	0.0000	-0.2190	0.0001	0.0000	-0.2190	0.0001
	-0.0759	0.0000	0.0000	-0.0759	0.0000	0.0000
	-0.0001	0.0001	0.0002	-0.0001	0.0001	0.0002
$M_{\alpha\beta}^2$	0.0002	0.0656	-0.0002	0.0002	0.0656	-0.0002
	-0.0390	0.0000	0.0383	-0.0389	0.0000	0.0383
	0.0004	0.0555	-0.0004	0.0004	0.0555	-0.0004
$M_{\alpha\beta}^4$	-0.0438	0.0080	0.0401	-0.0439	0.0080	0.0401
	0.0381	0.0046	0.0421	0.0381	0.0046	0.0421
	-0.0757	-0.0164	0.0686	-0.0757	-0.0164	0.0686

Basis Set			ET-pVQZ			
$M_{\alpha\beta}^\lambda$	$(M_{\alpha\beta}^\lambda)^{CM,CO}$			$(M_{\alpha\beta}^\lambda)^{CM,DO}$		
$M_{\alpha\beta}^1$	0.0000	-0.7831	0.0000	0.0000	-0.7830	0.0000
	0.1832	-0.0000	-0.0000	0.1831	-0.0000	-0.0000
	-0.0000	-0.0000	0.0000	-0.0000	-0.0000	0.0000
$M_{\alpha\beta}^2$	-0.0000	0.0891	-0.0000	-0.0000	0.0890	-0.0000
	-0.0766	0.0000	0.2604	-0.0766	0.0000	0.2604
	0.0000	-0.0033	-0.0000	0.0000	-0.0034	-0.0000
$M_{\alpha\beta}^4$	-0.0114	0.1052	0.0118	-0.0114	0.1052	0.0118
	0.0354	0.0150	0.0534	0.0354	0.0150	0.0534
	-0.1074	0.0485	0.0024	-0.1075	0.0486	0.0024

Table 3.1: Comparison of AATs of **1** calculated using CO and DO gauges and the BP86 functional. $M_{\lambda\beta}^\alpha$ are given in a.u.

to the CM from the following equation:

$$(M_{\alpha\beta}^\lambda)^{\mathbf{Y}_{CM}} = (M_{\alpha\beta}^\lambda)^{\mathbf{R}_\lambda^0} + \frac{i}{4\hbar c} \sum_{\gamma\delta} \epsilon_{\beta\gamma\delta} (\mathbf{R}_\lambda^0 - \mathbf{Y}_{CM})_\gamma P_{\alpha\delta}^\lambda \quad (3.33)$$

Equation (3.33) is obtained from Eq. (2.153) by choosing $\mathbf{O}_2 = \mathbf{R}_\lambda^0$ and $\mathbf{O}_1 = \mathbf{Y}_{CM}$; where \mathbf{Y}_{CM} is the position vector of the center of mass.

Since $\mathbf{U}^{(1),H_\beta}$ required for the calculation of AATs is origin-dependent, the solution of the CPKS equations for a magnetic field perturbation has to be repeated for each intermediate origin \mathbf{R}_λ^0 when DO is used. The matrix $\mathbf{U}^{(1),\mathbf{R}_{\lambda\alpha}}$, on the other hand, is origin-independent, and therefore the SCF and the CPKS calculations for nuclear displacement do not have to be repeated. We note that even though solving the CPKS equations for a magnetic field perturbation is much simpler than solving them for a nuclear displacement perturbation (which is the

most time consuming part of the calculation of AATs), the calculation of $\mathbf{U}^{(1),H_\beta}$ in the DO gauge can become the bottleneck for large molecules. Therefore, it is desirable to use only the CO gauge for the calculations of the AATs.

Table 3.1 presents the AATs calculated using the CO, $(M_{\alpha\beta}^\lambda)^{CM,CO}$, and DO, $(M_{\alpha\beta}^\lambda)^{CM,DO}$, gauges with SZ and ET-pVQZ basis sets for the oxirane molecule. For brevity, only the results for the smallest (SZ) and largest (ET-pVQZ) basis sets and the BP86 functional are shown.

As can be seen the CO and DO gauges yield virtually identical AATs. Thus, Eqs. (2.153) and (3.33) are fulfilled for all basis sets which proves that our implementation yields origin-independent rotational strengths [20]. We therefore conclude that when analytical derivatives techniques and LAOs are used for the calculations of the AATs, the CO gauge should be the method of choice. The DO gauge on the other hand can be used as an additional check for the correctness and accuracy of the code.

Sum rules

A systematic study of the accuracy of the calculated AATs is difficult due to their large number (9N tensor components for a molecule with N atoms). A convenient measure of the quality of the AATs is the extent to which they satisfy the sum rules of Eqs. (2.158).

By systematically increasing the size of the basis sets, in this section we investigate the convergence of the sum rules to a stable limit and the degree to which the sum rules are fulfilled.

With the C_2 -axis chosen as the Z -axis, the only non-zero tensor components of oxirane are $\Sigma_{xy}^i = -\Sigma_{yx}^i$ ($i = 1, 2, 3$). Further, we note that the APTs sum rules, $\Sigma_{xy}^2 = \Sigma_{xy}^3$ and $\Sigma_{xy}^4 = 0$ are satisfied for all basis sets (these results are not shown). In this context, the sum rule $\Sigma_{xy}^1 = \Sigma_{xy}^2$ that relates the AATs and APTs, is the only sum rule of interest.

Table 3.2 gives the arithmetic mean of Σ_{xy}^1 and $-\Sigma_{yx}^1$ denoted as $\bar{\Sigma}_{xy}^1$, Σ_{xy}^2 and the experimental value of Σ_{xy}^3 . As can be seen, the magnitude of $\bar{\Sigma}_{xy}^1$ and Σ_{xy}^2 converge to a stable limit as the basis set size is increased. The average deviations of TZP and TZ2P values from the ET-pVQZ are 3.82 and 3.11 percent, respectively, for all three functionals. The differences between $\bar{\Sigma}_{xy}^1$ and Σ_{xy}^2 are less than one percent for ET-pVQZ and around two percent for TZP and TZ2P for all three functionals. Therefore, it is reasonable to assume that the ET-VQZ results are good approximations of the basis set limit. As far as the differences between different functionals are concerned we note that for oxirane the AATs obtained with BLYP converge faster and fulfill the sum rules to a higher degree

Functional	BP86				OLYP				BLYP			
Basis Set	a	$\bar{\Sigma}_{xy}^1$	Σ_{xy}^2	b	a	$\bar{\Sigma}_{xy}^1$	Σ_{xy}^2	b	a	$\bar{\Sigma}_{xy}^1$	Σ_{xy}^2	b
SZ	83.8	0.115	0.476	75.8	81.0	0.129	0.473	72.7	85.3	0.110	0.431	74.4
DZ	38.0	0.983	1.035	5.0	45.8	0.995	1.033	3.6	28.3	0.961	1.036	7.2
DZP	5.1	0.749	0.716	4.6	10.2	0.752	0.698	7.7	1.3	0.759	0.727	4.4
TZP	4.6	0.745	0.740	0.6	4.8	0.715	0.696	2.7	2.0	0.764	0.766	0.2
TZ2P	4.2	0.742	0.732	1.3	3.8	0.708	0.686	3.2	1.3	0.759	0.758	0.1
ET-pVQZ	-	0.712	0.717	0.6	-	0.682	0.679	0.4	-	0.749	0.749	0.0
Exp. Σ_{xy}^3	0.7396 \pm 0.0039				0.7396 \pm 0.0039				0.7396 \pm 0.0039			

Table 3.2: Comparison of $\bar{\Sigma}_{xy}^1 = \frac{1}{2}(\Sigma_{xy}^1 - \Sigma_{yx}^1)$ and Σ_{xy}^2 for **1**. a denotes the deviation from the ET-pVQZ value; b denotes the deviations of $\bar{\Sigma}_{xy}^1$ from Σ_{xy}^2 ; $\bar{\Sigma}_{xy}^1$, Σ_{xy}^2 and Σ_{xy}^3 are given in a.u.; a and b are given in percent. The experimental value for $\Sigma_{xy}^3 = \mu_z^G$ [49] is also shown. In the basis set limit $\bar{\Sigma}_{xy}^1 = \Sigma_{xy}^2 = \Sigma_{xy}^3$.

then the ones calculated with BP86 and OLYP.

The AATs are not directly measurable. However, they are connected via sum rules to the electric dipole moment which is experimentally accessible, see Eqs. (2.154), (2.156) and (2.158). Since the AATs are very sensitive to the functional used we compare the ET-pVQZ value of $\bar{\Sigma}_{xy}^1$ obtained with all three functionals to the experimental value of Σ_{xy}^3 . As can be seen in Table 3.2 the BLYP, BP86 and OLYP values deviate from the experimental value by 1.2, 3.7 and 8.9 percent, respectively. Again, the BLYP functional yields AATs of better accuracy than BP86 and OLYP. Thus, for oxirane, the relative accuracy of the functionals considered here for the calculation of the AATs is BLYP > BP86 > OLYP. However, it is important to note that the accuracy of the vibrational rotational strength is a function not only of the accuracy of the AATs, but also of the accuracy of the APTs and the normal modes (the transformation $\mathbf{S}_{\lambda\alpha,i}$). In fact, Stephens has shown [49] that the accuracy of the harmonic force field (which determines $\mathbf{S}_{\lambda\alpha,i}$) is the most critical parameter. Therefore, when comparing calculated VCD intensities to experiment the relative accuracy of different functionals may be different from the relative accuracy of the AATs obtained with the considered functionals.

3.3.2 The rotational strengths

To study the quality of the VCD spectra obtained with our implementation we calculated the rotational strengths for α -pinene (**2**) and Troger's base (**3**) using the BP86, BLYP and OLYP functionals and TZP and ET-pVQZ basis sets. The VCD spectra are simulated by representing the peaks as Lorentzian bands [50] with a constant half width of 4 cm⁻¹.

VCD spectra of α -pinene

The calculated and experimental spectra of α -pinene (**2**) are shown in Fig. 3.2 (ET-pVQZ) and Fig. 3.3 (TZP). The experimental data are taken from reference [50]. As can be seen in Figs. 3.2 and 3.3 the OLYP and BP86 functionals yield frequencies that are in very good agreement with the experiment even without scaling. It is well-known that harmonic frequencies from BP86 are usually close to experimental fundamental frequencies due to an error cancellation effect [51–53]. The frequencies calculated using BLYP are in fair agreement with the experiment although they are not as good as the ones obtained with OLYP and BP86. Since the three functionals give frequencies that are fairly close, and also yield rotational strengths that are qualitatively similar, i.e. have the same sign for most modes with significant rotational strengths, there is a fair correspondence between their VCD spectra. The best agreement with experiment is obtained for the BP86 functional, which enables a very clear assignment of the fundamental modes 17 to 47, 54 and 55. The OLYP and BLYP spectra have about the same accuracy when compared to experiment, with the OLYP spectrum being slightly better.

In the case of the BP86 functional, the sign of the calculated rotational strengths for some of the fundamentals (32 and 35 to 37) differs from the experimental spectrum for both ET-pVQZ and TZP basis sets. However, all of these modes have low VCD intensities. The TZP calculation additionally predicts a wrong sign for the weak rotational strengths of the modes 19, 24 and 29. The fundamentals 48 to 53 overlap in both calculated and experimental spectra.

In the case of the OLYP functional, the VCD spectra obtained with the TZP and ET-pVQZ basis sets are very similar. The modes 17 to 47 can be clearly assigned while the modes 48 to 55 are unresolved for both basis sets used. Again, the rotational strengths for some of the low-intensity modes (24, 25, 29, 32, 35 to 37 and 39) have opposite sign compared to the experimental values.

For the BLYP spectra, the basis set effect when changing from TZP to ET-pVQZ is more pronounced (see fundamentals 21 to 26 and 37 to 39 in Figs. 3.2 and 3.3). The fundamentals 17 to 47 can be clearly assigned while fundamentals 48–55 are unresolved for both ET-pVQZ and TZP spectra. The ET-pVQZ predicts the wrong sign for the fundamentals 21, 23, 26, 29–31, 35–37 and 39. The TZP basis yields the wrong sign for the fundamentals 24, 29, 30, 35–37, 39–40.

To sum up, the BP86 spectra agree very well with the experimental spectrum; the differences between the TZP and ET-pVQZ spectra are very small. The larger ET-pVQZ basis improves the agreement with experiment for the fundamentals 19, 24, and 29, by predicting the correct sign. The OLYP functional yields spectra

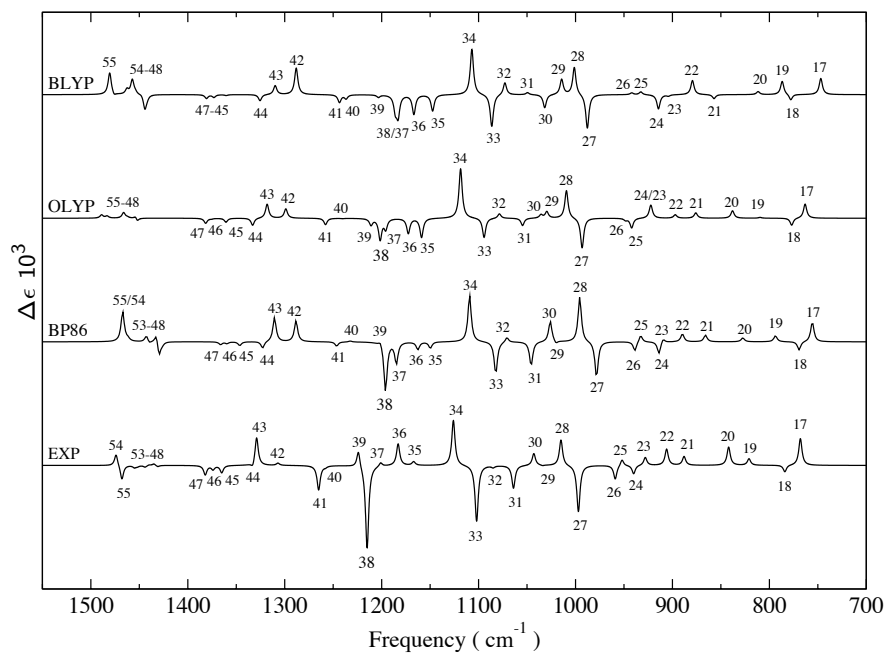


Figure 3.2: VCD spectra for α -pinene (**2**). Comparison of experiment with ET-pVQZ basis calculations for different functionals (BP86, OLYP, BLYP).

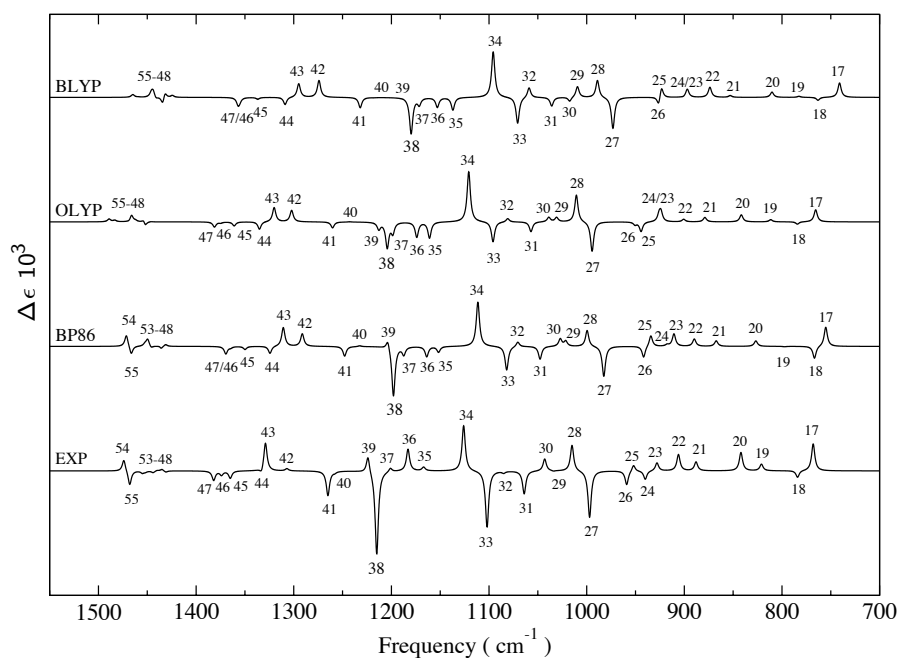


Figure 3.3: VCD spectra for α -pinene (**2**). Comparison of experiment with TZP basis calculations for different functionals (BP86, OLYP, BLYP).

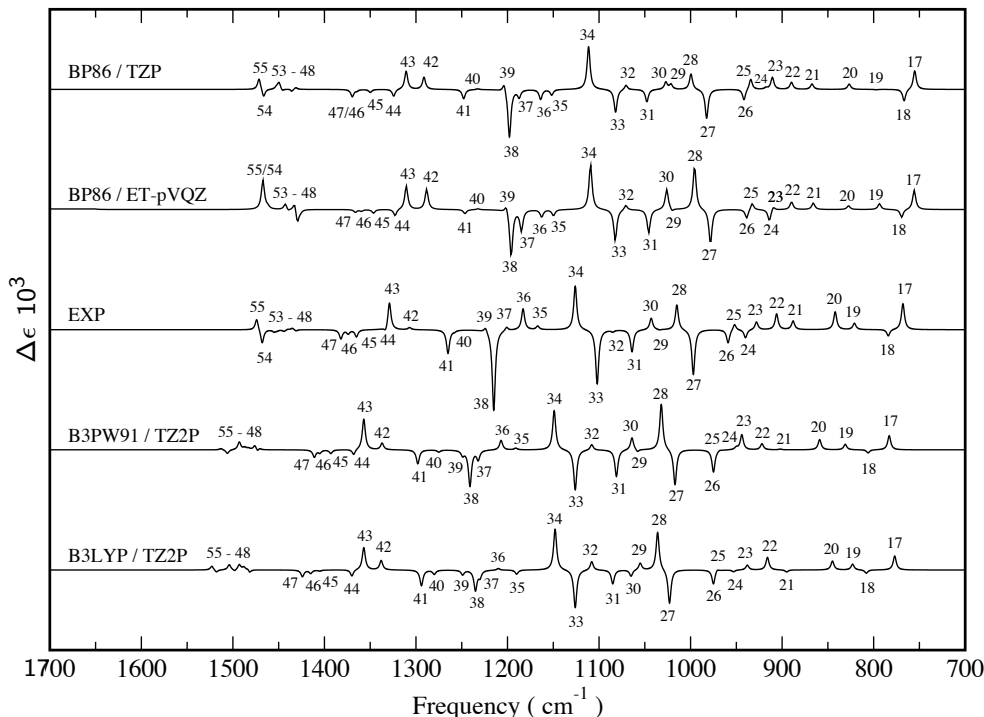


Figure 3.4: VCD spectra for α -pinene (**2**). Comparison between the experimental spectrum spectra obtained with the OLYP, BP86, B3PW91 and B3LYP functionals.

less accurate than the BP86 functional but better than the BLYP functional when the ET-pVQZ basis sets are used. For TZP basis sets the OLYP and BLYP functionals yield VCD spectra of comparable accuracy when compared to the experimental spectrum. Thus, for α -pinene, the relative accuracy of the functionals is $\text{BP86} > \text{OLYP} \geq \text{BLYP}$.

Since hybrid functionals are very popular for the calculation of VCD spectra, in what follows we compare the VCD spectra obtained here using pure density functionals with the results from calculations employing hybrid functionals that have been published before. In reference [50] the IR and VCD spectra of **2** have been calculated using the B3PW91 and B3LYP hybrid functionals and TZ2P basis set. The two hybrid functionals yielded very similar spectra that compare well with experiment. The B3PW91 spectrum reproduces the experimental spectrum somewhat better than the B3LYP spectrum. Figures 3.4 shows the BP86/TZP, BP86/ET-pVQZ, B3PW91/TZ2P and B3LYP/TZ2P VCD spectra together with the experimental one. For a fair comparison, the B3PW91 and B3LYP spectra in Fig. 3.4 were obtained by broadening the rotational strengths and frequencies published in reference [50] using the same technique used to obtain the BP86

spectra. As can be seen in Fig. 3.4 all four calculated spectra are qualitatively very similar and lead to an identical assignment of all fundamentals. The modes 17, 27-28, 33-34, 38 and 43 with relative high VCD intensities, that stand out in the experimental spectrum, are reproduced by all calculated spectra. For the modes with less intense VCD signals differences exist. Thus, for modes 21-26 the spectra obtained with BP86 are clearly superior to the ones obtained with hybrid functionals. The BP86/ET-pVQZ spectrum is the only spectrum that clearly reproduces the experimental pattern; the BP86/TZP spectrum shows a basis set effect only for mode 24, which has low intensity (positive) for the TZP basis. The B3PW91 and B3LYP spectra have been judged to be in qualitative disagreement with the experiment [50]. In the case of modes 35-37 BP86 predicts the wrong sign for all three modes for both ET-pVQZ and TZP basis sets; B3PW91 predicts the wrong sign only for mode 37 while B3LYP yields the wrong sign for the modes 35 and 37.

In conclusion, we would argue that the BP86/ET-pVQZ has yielded overall the best agreement with experiment, even though only marginally so in comparison to B3PW91/TZ2P, and not in every detail. The smaller TZP basis hardly deteriorates the BP86/ET-pVQZ results, and for instance BP86/TZP apparently performs better than B3LYP/TZ2P. One certainly does not obtain superior performance with the more expensive hybrid functionals.

VCD spectra of Troger's base

The absolute configuration of Troger's base (**3**) has been determined by a combination of experiment and calculation [54]. Because the VCD spectra of (**3**) follow the same patterns observed in the case of (**2**), only the BP86/TZP, OLYP/TZP are shown. A comparison of the BP86/TZP, OLYP/TZP and experimental VCD spectra of (**3**) is shown in Fig. 3.5. The experimental data are taken from reference [54].

As can be seen from Fig. 3.5 both calculated spectra compare very well with experiment. The OLYP and BP86 functionals yield frequencies that are very close to the experimental ones; there is no need for scaling. The OLYP frequencies are slightly better than the BP86 ones. The calculated rotational strengths are also in very good agreement with the experiment, permitting an unambiguous assignment of almost all fundamentals from 33 to 87 that have a considerable VCD intensity. For the few modes with low VCD intensities or those vibrations with overlapping peaks, a clear assignment was not possible. Thus, both functionals predict the wrong sign for the modes 33, 40, 46, 68, 70, 71; BP86 also predicts the incorrect sign for mode 67. The modes 54 to 56, 62, 63, 71 and 72 have very

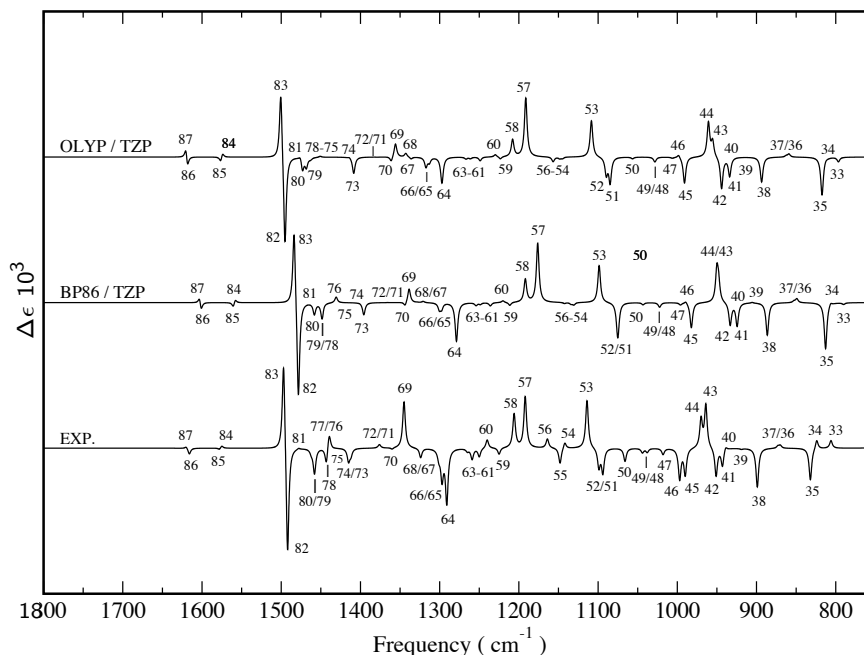


Figure 3.5: VCD spectra for Troger's Base (**3**). Comparison of experiment with TZP calculations.

low VCD intensities which prevents a detailed assignment for both functionals; the same holds true for the modes 75 to 78 calculated with OLYP. To sum up, the OLYP and BP86 functionals predict VCD spectra of **3** that reproduce the experimental spectrum very well. The frequencies and rotational strengths from OLYP are slightly better than the ones obtained with BP86. We refrain from performing calculations with larger basis sets since the results obtained for α -pinene indicate that the spectra are converged with respect to the size of the basis set.

In reference [54] the VCD spectra of **3** have been calculated using the B3PW91 and B3LYP hybrid functionals and 6-31G* basis sets. In Fig. 3.6 we present a comparison between the VCD spectra obtained here with the BP86 and OLYP functionals and TZP basis sets, the B3PW91/6-31G* spectrum, and the experimental VCD spectrum. Due to the similarity of the B3PW91 and B3LYP spectra only the first one was considered here. The B3PW91 spectrum in Fig. 3.6 was obtained by broadening the rotational strengths and frequencies published in reference [54] using the same technique used to obtain the BP86 and OLYP spectra. As can be seen from Fig. 3.6 the frequencies obtained with the BP86 and OLYP functionals are superior to the ones obtained with B3PW91 when compared to experiment (the calculated frequencies are not scaled). Apart from the frequencies, the three functionals predict spectra that are qualitatively very similar. All

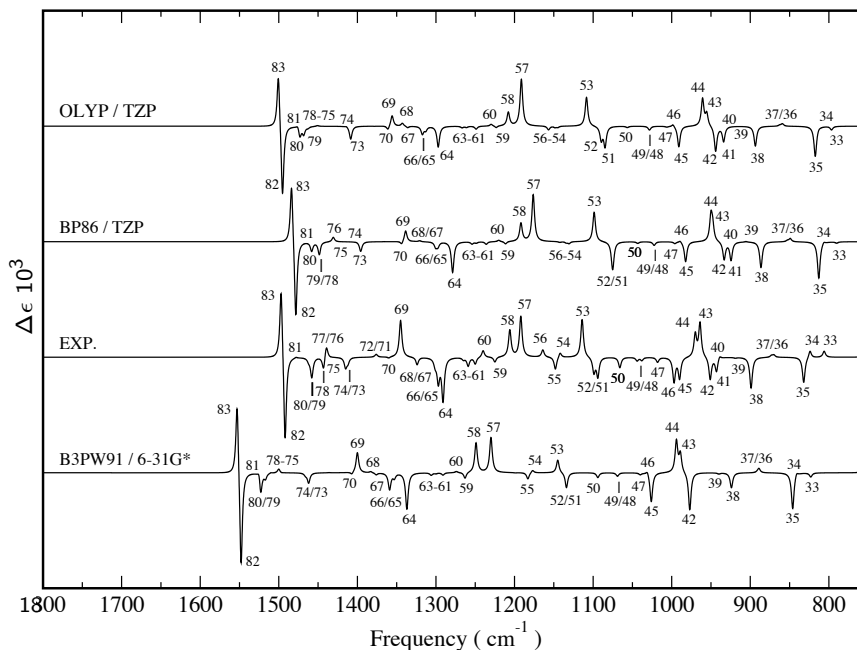


Figure 3.6: VCD spectra for Troger's Base (**3**). Comparison between the experimental spectrum and spectra obtained with the OLYP, BP86 and B3PW91 functionals.

significant features of the experimental spectrum, i.e. modes 35, 38, 42-45, 51-53, 57, 58, 64, 69 and 82-83, are reproduced by all calculated spectra. The OLYP and BP86 spectra are somewhat closer to the experimental spectrum. This is not only due to their superior frequencies, but also because they reproduce somewhat better some regions of the experimental spectrum. Thus, mode 41, is unresolved in the B3PW91 spectrum while it is unambiguously assigned in the BP86 and OLYP spectra. Modes 51 and 52 overlap in the BP86 and B3PW91 spectra while they can be clearly distinguished in the OLYP and experimental spectra.

In conclusion, the OLYP, BP86 and B3PW91 functionals yielded VCD spectra in very good agreement with the experiment that lead to identical assignment of all the modes with reasonable intensities. The spectra obtained with OLYP and BP86 functional are better than the B3PW91, mostly due to their superior frequencies.

3.4 Conclusions

In this chapter we have described in detail the implementation of the Stephens' equations for VCD in ADF and the validation of our implementation. The com-

parison of AATs calculated with the distributed origin gauge and the common origin gauge has proven that the LAO-STO-based implementation works correctly, as the two origin gauges yield virtually identical AATs and therefore origin-independent rotational strengths. Thus, the calculations are not sensitive to the special techniques which have to be used in connection with STOs, i.e. the numerical integration for the matrix elements. It was demonstrated that the sum-rules are fulfilled and quite accurate results can be obtained for the AATs even with moderately large STO basis sets like TZP. In these cases, the sum rules are fulfilled to within 3 % or less. For the largest basis sets used here, the error in the sum-rules drops to less than 0.7 %. Although the AATs obtained with a TZP basis are apparently almost converged w.r.t. the basis set size, we would like to note that calculations with the much larger ET-pVQZ basis set are straightforward for reasonably large molecules with our efficient implementation, which heavily makes use of the parallelization and linear-scaling techniques available in ADF.

The comparison of calculated VCD spectra obtained with different combinations of functionals and basis sets and experimental spectra underlines the importance of accurate vibrational frequencies and the corresponding normal modes. The BP86 VCD spectra are usually superior to the BLYP spectra in terms of agreement with experiment. This is due to the well-known feature of BP86 to yield harmonic force fields in close agreement with experiment [51–53]. VCD spectra from OLYP calculations are comparable to or sometimes even slightly better than those obtained with BP86. This is because the two functionals yield similar force fields. Regarding the basis set dependence of the VCD spectra it turns out that a TZP basis set is sufficiently large for calculations of reasonable accuracy. Our tests, performed on many chiral molecules suggested that BP86/TZP is always a safe choice for a good agreement with experiment.

Although the most popular exchange–correlation functionals for VCD calculations are the B3PW91 and B3LYP hybrid functionals, calculations with the non-hybrid functionals employed here, i.e., BP86 and OLYP, have yielded improved frequencies and rotational strengths that are at least as good. Another advantage of these functionals is that efficient and accurate density-fitting techniques can readily be applied in order to reduce the computational cost.

We have thus demonstrated that our implementation is correct and therefore can be applied for theoretical predictions of VCD spectra, which as demonstrated by the multitude of examples in literature [49, 50, 54–59] is an important prerequisite for assigning the absolute configurations of chiral molecules.

Chapter 4

Effects of complex formation on VCD spectra

Due to a copyright agreement with the American Chemical Society (ACS), this chapter has been removed as it is part of an ACS publication, i.e. *J. Phys. Chem. A*, 2008, 112 (30), pp 6978–6991. A link to the published article appears below:

<http://pubs.acs.org/action/doSearch?action=search&author=Nicu&qsearchArea=author&type=within&publication=40026049>

Chapter 5

Robust Normal Modes in VCD Spectra

5.1 Introduction

When using VCD, the AC of a given molecule is determined by comparing its experimental and calculated VCD spectra. The procedure relies on two facts, the optical enantiomers have VCD spectra of equal magnitude but opposite sign, and the AC of the molecule used in the calculation is known. Therefore, in order to have reliable prediction of AC using VCD, accurate calculations of VCD spectra are required.

Very good agreement between experimental and calculated VCD spectra [50, 54, 81–83] is obtained when the effects induced by the solvent are negligible and when the calculation is for the conformation present in solution (i.e. in case of rigid molecules, or in general if a single conformation is populated in the experimental sample). However, very often these conditions are not met. Many studies [66, 72, 84–88] have shown that the shapes of VCD spectra depend sensitively on the solvent used and also on the concentration of the solute. At the same time, perturbations such as solute-solvent and/or solute-solute interactions are neglected in calculations performed on isolated gas phase molecules. Thus, discrepancies between calculated VCD spectra and experimental VCD spectra measured in solution are often observed.

Currently, continuum solvation models [89] are the only methodology available for modeling solvent effects in DFT VCD calculations. However, as a number of studies have shown [61, 66–68, 70–72, 85] approximating the solvent by a continuum dielectric medium is not sufficient to model the effects on the VCD spectra; specific interactions such as hydrogen-bonding must be taken into account.

Therefore, until more accurate treatments of the solvent will be available, it is desirable to know: a) what type of discrepancies between calculated gas phase VCD spectra and solution experimental VCD spectra can be ascribed to solvent effects, b) what are the mechanisms that induce the observed discrepancies, and c) which of the normal modes are likely/unlikely to be affected by the solvent.

We have addressed these questions in the previous chapter by investigating (theoretically) the effects induced in the VCD spectra by complex formation. As shown in chapter 4, the various differences observed when comparing experimental and calculated VCD spectra (e.g. modes that have different signs, modes with significantly different VCD intensities, modes with shifted frequencies, the appearance of new VCD signals) can all be encountered in case of, and can be explained by complex formation. The theoretical analysis in chapter 4 of the mechanisms that induce the effects enumerated above has shown that: A) some normal modes are more susceptible than others to exhibit a sign change of their rotational strength, and B) the same mechanisms can induce either a change of sign or a change of magnitude of the rotational strengths. These findings led us to the conclusion that the normal modes in a VCD spectrum can be classified as *robust* and *non-robust*. The sign of the rotational strengths of the *non-robust* modes can easily be changed by small perturbations (e.g. solvent effects). The *robust* modes on the other hand have rotational strengths with characteristic sign that should not be affected by small perturbations.

As discussed in the previous chapters, VCD intensities are determined by the rotational strengths (R). Depending on the value of the angle $\xi(i)$ between the vectors electric and magnetic dipole transition moments (EDTM and MDTM) of a mode i , the $R(i)$ can be positive or negative. Thus, $R(i)$ is positive when the angle $\xi(i)$ is smaller than 90° since $\cos[\xi(i)] > 0$, whereas when $\xi(i)$ is larger than 90° $R(i)$ is negative since $\cos[\xi(i)] < 0$. However, when $\xi(i)$ is close to 90° , even a small perturbation can change $\xi(i)$ across 90° . This will result in a sign change. Thus, the *non-robust* modes are characterized by values of ξ that are close to 90° , and as a result their sign can be changed easily. The *robust modes* on the other hand, have ξ angles that are far from 90° and therefore their sign is less likely to be changed by small perturbations present in the experiment or when using slightly different computational parameters.

At the computational side, the choice of exchange-correlation functional affects the calculated VCD spectra. There are many reasonable functionals, and there has not yet emerged one that is clearly universally superior. Moreover, combined experimental and computational studies by Stephens et al. [90, 91] have shown that in case of VCD, in order to achieve good agreement between experimental and calculated spectra, the exchange-correlation functional is the

most critical computational parameter. Therefore, going from one functional to another one may be considered a computational perturbation.

In this chapter we investigate this computational perturbation in the light of the distinction between robust and non-robust modes. There are two questions that need to be answered: 1) Can we apply this concept also to this type of perturbation, and 2) can we identify the modes that can safely be used in the comparison between experiment and theory to distinguish between different ACs? Answering these question should tell us which modes should be used (or not used) when determining the AC of a compound using VCD. There are always discrepancies between experiment and theory in the sign and magnitude of some rotational strengths, but when they are for non-robust modes, they should be of no concern.

The goal of this study is to establish criteria for determining the robustness of the normal modes in the calculated VCD spectra, i.e to determine an appropriate angle interval that enables one to classify a normal mode i as *robust* or *non-robust* depending whether or not its angle $\xi(i)$ belongs to that angle interval. To achieve this, we investigate: 1) the range of values taken by the ξ angles of the normal modes of various molecules, and 2) how the values of the ξ angles change when different exchange-correlation (BP86 vs. OLYP) functionals are used.

The chapter is organized as follows: first we discuss the constraints imposed by the molecular symmetry on the orientation of the electric and magnetic dipole transition moments, then after describing the computational procedure the results are presented and discussed. Finally, the chapter is summarized with some concluding remarks.

5.2 Theory

As shown in chapter 2, section 2.1.4, in achiral molecules the EDTMs and the MDTMs of a given mode i are perpendicular, i.e. $\xi(i) = 90^\circ$, whereas in chiral molecules they are usually not, i.e. $\xi(i) \neq 90^\circ$.

Symmetry constraints can impose further restrictions on the orientation of the EDTMs and MDTMs. Thus, in chiral molecules that have symmetry only certain values are permitted for the angles $\xi(i)$. Chiral molecules belong to point groups that have only proper rotation axes: C_1 , C_n , D_n (with $n \geq 2$), T , O and I . As an example, we will consider the case of a molecule with C_2 symmetry. Group theory states that a matrix element of the form $\langle \psi_a | \hat{O} | \psi_b \rangle$ is zero unless the integrand transforms as the totally symmetric representation of the molecular

point group:

$$\Gamma(\psi_a) \times \Gamma(\hat{O}) \times \Gamma(\psi_b) = A \quad (5.1)$$

For the matrix elements associated with the EDTM and MDTM of a given mode i , see Eq. (2.143), Eq. (5.1) is written:

$$\Gamma(0) \times \Gamma(\hat{O}) \times \Gamma(1) = A \quad (5.2)$$

where the operator \hat{O} is either $(\vec{\mu}_E)_k$ or $(\vec{\mu}_M)_k$ ($k = x, y, z$).

As can be seen in Eq. (2.7), the components of the electric dipole operator, $\vec{\mu}_E$, transform as the components of the vectors \vec{r}_a and \vec{R}_λ (as translations x, y, z in the character tables). From Eq. (2.8), the components of the magnetic dipole operator, $\vec{\mu}_M$ transform as the components of angular momentum (as rotations R_x, R_y, R_z in the character tables).

For C_2 symmetry the z Cartesian components of both $\vec{\mu}_E$ and $\vec{\mu}_M$ have A symmetry, whereas the x and y components have B symmetry. The normal modes of molecules with C_2 symmetry have either A or B symmetry. The harmonic wave function associated to the ground vibrational state, $|0\rangle$, has A symmetry for all modes [22], whereas the harmonic wave function of the first excited vibrational state, $|1\rangle$, of a mode i has the same symmetry as the mode i (either A or B symmetry) [22]. Thus, for modes of A symmetry the left term of Eq. (5.2) becomes:

$$\Gamma(0) \times \Gamma(\hat{O}) \times \Gamma(1) = A \times \Gamma(\hat{O}) \times A = A \times \Gamma(\hat{O}) \quad (5.3)$$

In order to have $A \times \Gamma(\hat{O}) = A$ in Eq. (5.3) and thus, non-zero electric and magnetic dipole transition moments, $\Gamma(\hat{O})$ is necessarily A . Thus, in modes of A symmetry only the z Cartesian components of both transition dipole moments are non-zero. As a result, the transition dipole moments $\vec{E}_{01}(i)$ and $\vec{M}_{10}(i)$ are either parallel $\xi(i) = 0^\circ$ or antiparallel $\xi(i) = 180^\circ$.

For modes of B -symmetry, we have:

$$\Gamma(0) \times \Gamma(\hat{O}) \times \Gamma(1) = A \times \Gamma(\hat{O}) \times B = B \times \Gamma(\hat{O}) \quad (5.4)$$

In order to have $B \times \Gamma(\hat{O}) = A$ in Eq. (5.4) and thus non-zero electric and magnetic dipole transition moments, $\Gamma(\hat{O})$ is necessarily B . This means that in modes of B symmetry the x and y Cartesian components of both transition dipole moments are non-zero. Since the two transition dipole moments can have any orientation in the xy plane, there are no symmetry restrictions on the values taken by the $\xi(i)$ angles in the modes of B symmetry. Using the character tables, similar conclusions can easily be obtained for all the point groups.

Finally, we note that in the chiral molecules without symmetry there are no restrictions on the orientations of the EDTMs and MDTMs. As a result the two

transition dipole moments can have any orientation with respect to each other. This means that in chiral molecules without symmetry the angles ξ can take any value between 0° and 180° .

5.3 Method

In the first part of the study presented in this chapter the values of the ξ angles are investigated. Thus, 27 chiral molecules ranging from very small molecules (5 atoms) to relatively large molecules (48 atoms) have been considered. The distributions of the values of the angles ξ of each molecule are analyzed by calculating the arithmetic means, $\bar{\xi}$, and the standard deviations, $\sigma(\xi)$. Since in most VCD studies in the literature only the finger print region is considered (the frequency interval between 800 and 1800 cm^{-1}), we have analyzed the distribution of the ξ angles of all normal modes and also of only the finger print modes.

In the second part of the study presented in this chapter, we investigate the differences between the values of the ξ angles calculated with the BP86 and OLYP functionals. For a consistent evaluation of these differences a one-to-one mapping between the BP86 and OLYP modes of each molecule is established first by calculating overlaps of normal modes. The normal modes overlaps (Ω) are calculated according to the procedure described in chapter 4 section ??.

As expected, the modes obtained with the two functionals, although very similar, are not identical. Thus, for all the molecules considered, an overlap of at least 0.90 has been calculated for more than 90% of the BP86 and OLYP modes; the remaining 10 percent show overlaps of at least 0.7.

The modes of one functional can be obtained as linear combination of the modes of the other functional:

$$\vec{V}(i, \text{BP86}) = \sum_j \Omega(i, j) \vec{U}(j, \text{OLYP}) \quad (5.5)$$

where $\vec{V}(i, \text{BP86})$ and $\vec{U}(j, \text{OLYP})$ are the $3N$ -dimensional vectors defined in Eq. (??) associated to the BP86 i^{th} and OLYP j^{th} normal modes, respectively. The expansion coefficients, $\Omega(i, j)$, are the normal modes overlaps, and are calculated according to Eq. (??). Since the modes calculated with a given functional are orthogonal, we have:

$$\sum_j \Omega^2(i, j) = 1 \quad (5.6)$$

Thus, an overlap of 0.90 between a BP86 and an OLYP mode means that the two modes differ by 20%, whereas an overlap of 0.70 means that the two modes differ

by 51%. As a result, when analyzing the differences, $\Delta\xi$, between the angles ξ calculated with the two functionals, we have considered only the BP86–OLYP mode pairs with overlaps of at least 90°. The distributions of the values of $\Delta\xi$ are analyzed by calculating for each molecule the arithmetic mean, $\overline{\Delta\xi}$, of all the $\Delta\xi$,

$$\overline{\Delta\xi} = \frac{1}{N_{\Delta\xi}} \sum_{a=1}^{N_{\Delta\xi}} \Delta\xi_a, \quad \Delta\xi_a = \xi_a(BP86) - \xi_a(OLYP). \quad (5.7)$$

the largest $\Delta\xi$, $\Delta\xi_{max}$,

$$\Delta\xi_{max} = \max(|\Delta\xi_a|) \quad (5.8)$$

and the standard deviation of all $\Delta\xi$, $\sigma(\Delta\xi)$,

$$\sigma(\Delta\xi) = \frac{1}{N_{\Delta\xi}} \left[\sum_{a=1}^{N_{\Delta\xi}} (\overline{\Delta\xi} - \Delta\xi_a)^2 \right]^{\frac{1}{2}} \quad (5.9)$$

In Eqs. (5.7), (5.8) and (5.9) $N_{\Delta\xi}$ is the number of BP86–OLYP normal mode pairs considered for each molecule, which is not always the total number of modes, see below.

The number of BP86–OLYP mode pairs considered, $N_{\Delta\xi}$, is determined as follows. In the first place, as noted above, a pair is not taken into account whenever the overlap $\Omega(a, a)$ is below 0.90. In the second place we have excluded modes with small EDTM or MDTM because we have found that very large $\Delta\xi$ can be encountered when at least one of the transition dipole moments of a normal mode has very small magnitude. As an example, we compare the EDTMs and MDTMs of mode 52 of benzoyl-benzoic acid (BBA) (molecule **21** in Fig. 5.1) calculated with the BP86 and OLYP functionals.

Table 5.1 lists the overlap (Ω) of the BP86 and OLYP modes, the frequency, rotational strengths, the angles ξ , and the Cartesian components of the EDTMs and MDTMs calculated with the two functionals. As can be seen, the BP86 and OLYP modes of pair 52 of BBA have very similar frequencies and normal modes (the normal modes overlap is 0.99). The MDTMs of both functionals have relatively large magnitudes and similar values, their Cartesian components are also very similar. Thus, the direction of the MDTM of mode 52 of BBA was not affected by the change of functional. However, mode 52 of BBA has a very small EDTM (also compared to the rest of BBA modes). Both functionals have predicted for it values that are very close to zero. Due to its small magnitude its direction can be easily perturbed. As can be seen in Table 5.1 this is indeed the case, the BP86 and OLYP Cartesian components of the EDTMs of mode 52 are all small but very different. As a result the BP86 and OLYP ξ angles are

$\Omega = 0.99$		$\Delta\xi = 61.81$	
	Freq.	R	ξ
BP86:	1151.54	1.27	49.92
OLYP:	1162.00	-0.97	111.73
$\vec{E}_{01}(i)$	x	y	z
BP86:	-1.74	0.67	-2.29
OLYP:	-3.06	1.51	1.32
$\text{Im}[\vec{M}_{01}(i)]$	x	y	z
BP86:	-14.56	-35.34	-54.57
OLYP:	-12.32	-35.82	-61.13

Table 5.1: Comparison of the frequencies (cm^{-1}), rotational strengths (10^{-44} esu $\cdot\text{cm}$), ξ angle, electric dipole transition moments (10^{-21} esu $\cdot\text{cm}$) and magnetic dipole transition moments (10^{-25} esu $\cdot\text{cm}$) of the normal mode 52 of BBA calculated using the BP86 and OLYP functionals

quite different ($\Delta\xi = 61.81^\circ$). Clearly, the angle ξ of mode 52 of BBA cannot be reliably calculated, and most likely also perturbation due to a solvent would greatly change it. It should therefore be classified as a *non-robust* mode from the outset, and so should all modes with very small EDTM and/or MDTM.

We cannot give an absolute measure, valid for all molecules, to determine what should be considered small in this context. The magnitudes of the total EDTM and MDTM of a normal mode depend on the type of mode and on the number of atoms involved in the normal mode motion, i.e. on the molecule. However, for a given molecule one can easily determine the threshold value for “small”. Take the mean values of all EDTMs and of all MDTMs of all modes of that molecule, then the magnitude of a DTM of some mode is classified as “small” if it is less than 10% of the mean value.

The total number of BP86-OLYP mode pairs considered after removal of these small-DTM modes, $N_{\Delta\xi}$, is listed for each molecule in Tables 5.3 and 5.4 (compare to total number of modes in Table 5.2). $N_{\Delta\xi}$ is typically some 10% smaller than the total number of modes.

As in the previous chapters, all calculations (geometry optimization and IR/VCD calculations) were performed using the ADF program package [24–26]. The BP86 and OLYP functionals and the TZP basis set were used in all the calculations. The geometries have been optimized separately for each choice of

functional using the optimizer described in reference [44]. Very tight convergence criteria have been applied for the geometry optimization (10^{-6} Hartree for the energy and 10^{-4} Hartree/Ångström for the gradients).

5.4 Results and Discussions

Figure 5.1 shows schematic representations of all 27 test molecules we have considered for this study.

5.4.1 Characterization of robust modes

We will first consider possible differences between the finger print modes and the rest of the modes. We have analyzed the distributions of the angles ξ of all the normal modes, $\bar{\xi}_{all}$ and $\sigma(\xi_{all})$, and also of the finger print modes, $\bar{\xi}_{fp}$ and $\sigma(\xi_{fp})$, of each molecule. Table 5.2 lists the arithmetic means $\bar{\xi}_{all}$ and $\bar{\xi}_{fp}$, the standard deviations $\sigma(\xi_{all})$ and $\sigma(\xi_{fp})$, the total number of normal modes, and also the number of finger print modes for all 27 molecules.

As can be seen in Table 5.2, roughly half of the normal modes of a given molecule are in the finger print region. The only exception is molecule **3** which has only 2 out of its 9 modes in the finger print region. There are no significant differences between the distribution of ξ of all normal modes and the distribution of ξ of the finger print modes. The values of the ξ angles are distributed equally around 90° , the arithmetic means $\bar{\xi}_{all}$ and $\bar{\xi}_{fp}$ have both values that are very close to 90° . There are very few cases where the averages $\bar{\xi}_{all}$ and/or $\bar{\xi}_{fp}$ deviate from 90° by more than 5° ($\bar{\xi}_{all} = 96.75$ and $\bar{\xi}_{fp} = 99.20$ for **17**, $\bar{\xi}_{fp} = 100.54$ for **9**, and $\bar{\xi}_{fp} = 84.75$ for **10**). So even if in chiral molecules the ξ angles of individual modes may differ greatly from 90° , as is apparent from the large spread $\sigma(\xi)$ in the ξ values that exists for some molecules, e.g. 63° and 75° for molecules 1 and 2, the spread is obviously practically symmetrical around 90° . This statement remains true also when applied to just the finger print modes, although in that case the deviation of $\bar{\xi}_{fp}$ from 90° tends to be a bit larger, cf. the largest deviations quoted above. Similarly, only small variations are observed when comparing the standard deviations $\sigma(\xi_{all})$ and $\sigma(\xi_{fp})$. The differences between $\sigma(\xi_{all})$ and $\sigma(\xi_{fp})$ are less than 5° for 21 of the 27 molecules, less than 9° for the next 5 molecules and 14.66° for molecule **3** (which has only 2 finger print modes). We can therefore conclude that there do not seem to be systematic differences between the finger print modes and the other ones, which justifies the use of the former for the analysis of the VCD spectra. Our differentiation between robust and non-robust

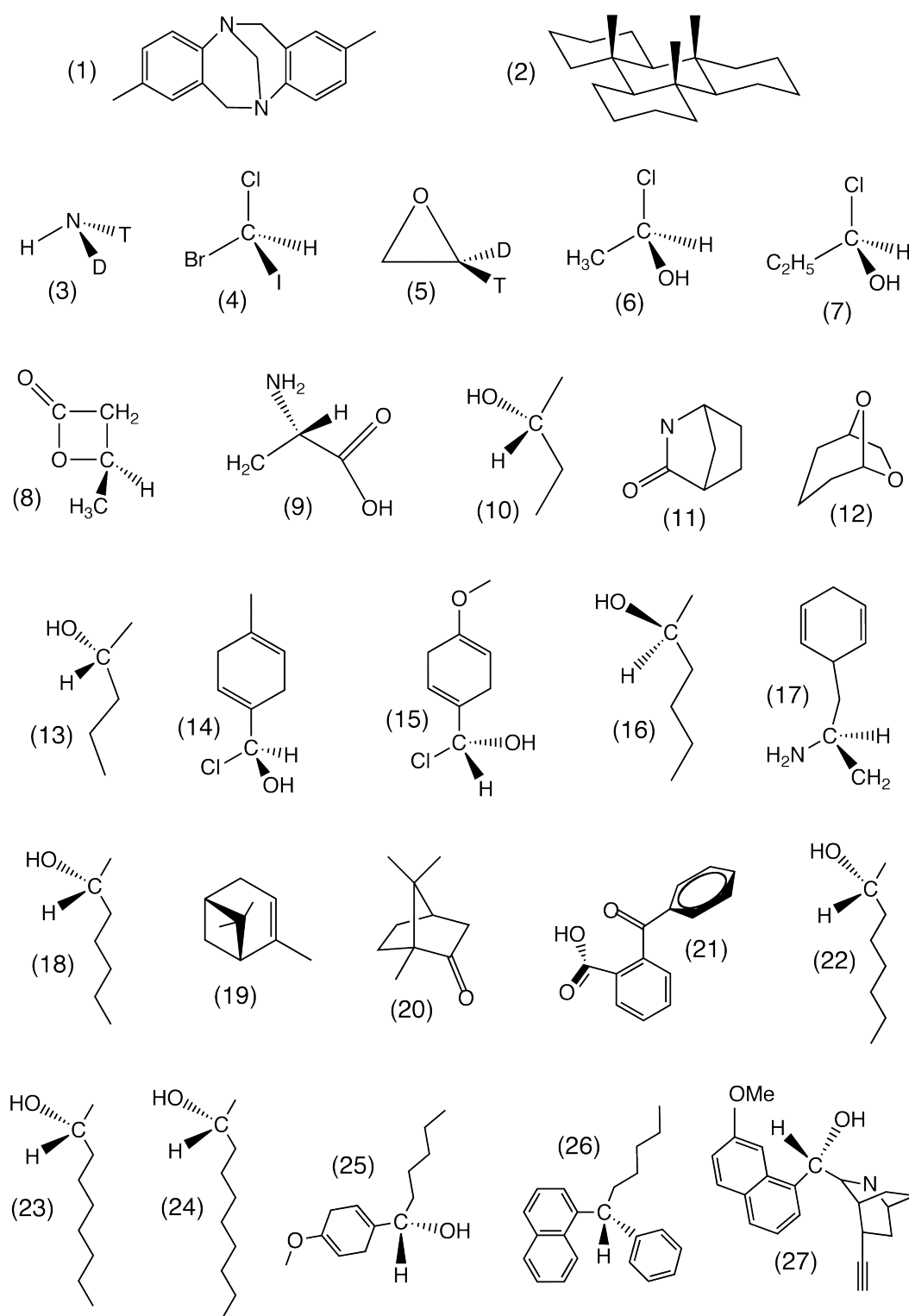


Figure 5.1: Schematic representation of the 27 molecules analyzed.

Molecule	All modes			Finger print modes		
	N	$\bar{\xi}$	$\sigma(\xi)$	N_{fp}	$\bar{\xi}$	$\sigma(\xi)$
1	105	93.16	62.66	54	92.82	65.65
2	138	90.40	75.47	78	89.71	77.64
3	6	92.86	23.55	3	93.36	12.15
4	9	90.46	20.10	2	90.70	5.44
5	15	91.31	14.86	8	93.94	18.36
6	21	92.94	29.59	10	93.47	36.95
7	30	93.37	30.71	14	94.00	39.23
8	30	90.67	31.03	15	92.37	36.86
9	33	90.92	30.39	15	100.54	31.92
10	39	88.26	16.69	19	84.75	15.18
11	45	90.43	32.52	25	89.14	36.78
12	48	89.71	36.40	28	91.18	39.08
13	48	92.42	20.59	25	89.61	24.21
14	51	91.56	32.12	25	91.95	30.37
15	54	89.04	29.67	25	87.31	32.44
16	57	91.57	22.04	29	90.67	28.15
17	63	96.75	27.67	34	99.20	29.01
18	66	89.08	25.33	34	87.22	31.83
19	72	90.21	29.77	37	92.85	33.80
20	75	87.36	28.77	39	89.53	30.57
21	74	86.78	20.03	35	89.78	11.90
22	75	91.42	23.41	38	89.44	26.57
23	84	91.59	25.50	42	91.41	29.56
24	93	92.21	23.26	47	91.04	27.36
25	99	89.04	17.80	49	87.96	19.26
26	132	89.93	24.73	66	88.03	24.26
27	132	89.52	12.49	64	88.33	9.94

Table 5.2: Statistics of the angles ξ . $\bar{\xi}$ is the arithmetic mean and $\sigma(\xi)$ is the standard deviation of the angles ξ of a given molecule. The total number of modes (N) and the number of the finger print modes (N_{fp}) of each molecule are also given.

modes, see below, will be applicable to all the modes, including the finger print modes.

In order to make the distinction between robust and non-robust modes we consider the typical magnitude of a change in the angle ξ caused by change of

Molecule	$N_{\Delta\xi}$	All modes			$N_{\Delta\xi_{fp}}$	Finger print modes		
		$\overline{\Delta\xi}$	$\Delta\xi_{max}$	$\sigma(\Delta\xi)$		$\overline{\Delta\xi}$	$\Delta\xi_{max}$	$\sigma(\Delta\xi)$
3	6	0.25	6.29	3.74	3	0.23	0.34	0.13
4	9	-4.12	3.48	6.26	2	-0.12	1.29	1.41
5	14	1.35	9.66	3.41	7	2.47	9.66	4.14
6	21	0.43	6.27	3.96	10	0.91	4.68	2.02
7	24	1.09	24.77	9.42	13	-1.02	16.67	10.38
8	30	1.27	23.82	7.41	15	-0.46	10.73	5.69
9	33	0.54	19.92	6.22	15	-1.12	3.77	3.64
10	35	-0.38	4.28	2.86	19	-0.33	4.28	3.38
11	42	-0.89	13.40	7.22	25	-0.88	13.40	7.03
12	42	0.78	18.02	7.10	26	-0.06	18.02	6.31
13	45	0.57	20.83	6.31	25	1.03	20.83	7.15
14	41	-0.81	26.89	7.05	25	-0.56	26.89	7.63
15	49	0.08	25.24	9.31	23	-0.36	25.24	9.92
16	53	0.54	27.10	5.93	28	-0.05	9.81	5.74
17	57	1.44	27.46	7.30	31	1.20	27.46	7.54
18	54	0.35	19.18	6.20	30	1.04	19.18	6.45
19	58	-1.10	21.03	7.68	27	-0.80	21.03	7.79
20	63	0.28	27.82	8.51	38	1.15	27.82	9.15
21	58	-0.10	15.94	5.66	29	0.29	15.94	4.08
22	68	0.65	23.46	6.41	35	1.73	13.95	4.22
23	63	-0.54	12.74	6.45	33	-0.28	12.74	7.92
24	79	-0.38	11.72	6.19	44	0.75	11.72	5.25
25	91	0.21	23.65	6.26	46	0.58	16.66	5.72
26	111	0.13	26.05	6.77	55	0.46	26.05	7.21
27	110	-0.16	20.71	5.43	56	-0.25	16.08	4.45

Table 5.3: Statistics of $\Delta\xi$ (the difference between the BP86 and OLYP ξ angles). $\overline{\Delta\xi}$ is the arithmetic mean of all $\Delta\xi$ of a molecule, $\Delta\xi_{max}$ is the maximum $\Delta\xi$ for a molecule, $\sigma(\Delta\xi)$ is the standard deviation of the $\Delta\xi$ of a molecule. The total number of modes considered ($N_{\Delta\xi}$) and the number of the finger print modes among $N_{\Delta\xi}$ ($N_{\Delta\xi_{fp}}$) for each molecule are also given.

functional. We investigate the characteristics of the distribution of $\Delta\xi$ values, and the differences between the angles ξ calculated with BP86 and OLYP. This investigation is carried out for the modes that remain after we have excluded the ones that can be characterized as non-robust from the outset on the basis of the smallness of the EDTM and/or the MDTM, see Section 5.3. In addition, the

Molecule	$N_{\Delta\xi}$	N_{sign}	$\Delta\xi > 20^\circ$	$\Delta\xi > 25^\circ$	$\Delta\xi > 30^\circ$
3	6	0	0	0	0
4	9	2	0	0	0
5	14	2	0	0	0
6	21	0	0	0	0
7	24	0	2	1	0
8	30	2	2	0	0
9	33	1	0	0	0
10	35	3	0	0	0
11	42	0	2	0	0
12	42	5	0	0	0
13	45	5	1	0	0
14	41	1	1	1	0
15	49	6	3	1	0
16	53	5	2	1	0
17	57	3	1	1	0
18	54	9	1	0	0
19	58	9	2	0	0
20	63	4	1	1	0
21	58	6	0	0	0
22	68	12	2	0	0
23	63	12	2	1	0
24	79	13	1	0	0
25	91	10	2	0	0
26	111	10	3	1	0
27	109	8	2	0	0

Table 5.4: The number of BP86-OLYP normal modes pairs considered ($N_{\Delta\xi}$) and the number of modes that have changed sign upon changing the functional (N_{sign}). The last three columns give the numbers of BP86-OLYP modes pairs with $\Delta\xi$ larger or equal to 20° , 25° , 30° , respectively.

modes that mix are excluded. (This is not a criterium for non-robustness that can be used when just a single calculation with a chosen functional is performed; see the comments on how to deal with this phenomenon of mode mixing at the end of the paper.) Table 5.3 gives for each molecule the number of BP86-OLYP mode pairs considered, $N_{\Delta\xi}$, the arithmetic mean of the values of $\Delta\xi$, $\overline{\Delta\xi}$, the absolute value of the largest $\Delta\xi$, $\Delta\xi_{max}$, and the standard deviations of the distributions of $\Delta\xi$, $\sigma(\Delta\xi)$ (see Section 5.3 for more details).

As before, no significant differences between the data associated with all normal modes and the data associated with the finger print modes are observed. The averages $\overline{\Delta\xi}$ are close to zero. This means that the two functionals do not have a systematic difference. The standard deviations $\sigma(\Delta\xi)$ are almost all below 8° , there are only three outliers at 8.5° , 9.3° and 9.4° . Since about 95% of a Gaussian distribution are within 2 standard deviations from the mean, one should expect that 95% of the modes will have a $\Delta\xi$ smaller than 16° . Looking at the values of $\Delta\xi_{max}$ in Table 5.3, it may be noted that indeed there are some molecules with $\Delta\xi_{max} > 20^\circ$, but $\Delta\xi$ is never larger than 30° ; the largest value, $\Delta\xi_{max} = 27.82^\circ$, is exhibited by molecule **7**. To gain a more thorough understanding of the data in Table 5.3, we have listed in Table 5.4 the number of BP86–OLYP mode pairs with rotational strengths of different signs (N_{sign}) and the number of mode pairs with $\Delta\xi$ larger than 20° , 25° and 30° , respectively. As can be seen in Table 5.4 there are very few pairs of modes (≤ 3 for each molecule) with $\Delta\xi > 20^\circ$ and even fewer (≤ 1 for each molecule) with $\Delta\xi > 25^\circ$; as noted, none of the molecules has a $\Delta\xi$ larger than 30° . It is also important to note that, in general, the number of modes of a molecule whose rotational strength changes sign, N_{sign} , is much larger than the number of modes with a large $\Delta\xi (> 20^\circ)$. This clearly shows that the rotational strengths of many modes with relatively small $\Delta\xi$ still change sign, so they must have had ξ angles close to 90° . Of course those modes are most susceptible to change sign. It should also be realized that a large $\Delta\xi$ does not imply a change of ξ across 90° , if the few mode pairs with $\Delta\xi > 20^\circ$ happened to have ξ angles very different from 90° . An example in this regard is molecule **7** which has one mode with $\Delta\xi > 20^\circ$ and one mode with $\Delta\xi > 25^\circ$, but none of the modes of **7** have changed sign when going from BP86 to OLYP ($N_{sign} = 0$).

We have also verified whether a correlation between the value of ξ and the magnitude of the $\Delta\xi$ exists. However, no consistent pattern was observed, i.e. a large $\Delta\xi$ can be exhibited equally well by modes with ξ that are close to or far from 90° . Since $\Delta\xi > 20^\circ$ do occasionally occur, we conclude that a safe criterium would be that *robust* modes should have angles ξ that differ from 90° by at least 30° .

5.4.2 Molecules with symmetry

Troger’s base and D_3 –anti-trans–anti-trans–anti-trans–perhydrotriphenylene (molecules **1** and **2** in Fig. 5.1 and Table 5.2), have C_2 and D_3 symmetry, respectively. As shown in section 5.2, many of the modes of chiral molecules with symmetry have angles ξ that are far from 90° (e.g. 0° or 180°). As a result, the molecules **1** and **2** have very large standard deviations, i.e. $\sigma(\xi_{all}) = 62.66^\circ$

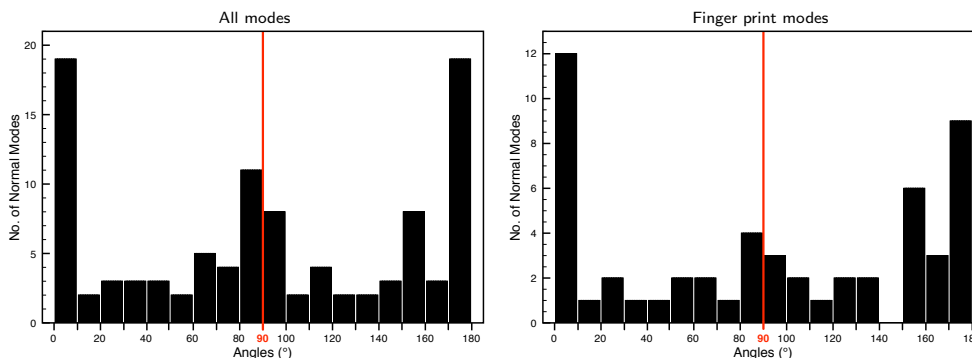


Figure 5.2: Distribution of the values of the ξ angles of molecule **1** (C_2 symmetry). The left panel shows the distribution of all normal modes (ξ_{all}). The right panel shows the distribution of the finger print modes (ξ_{fp}).

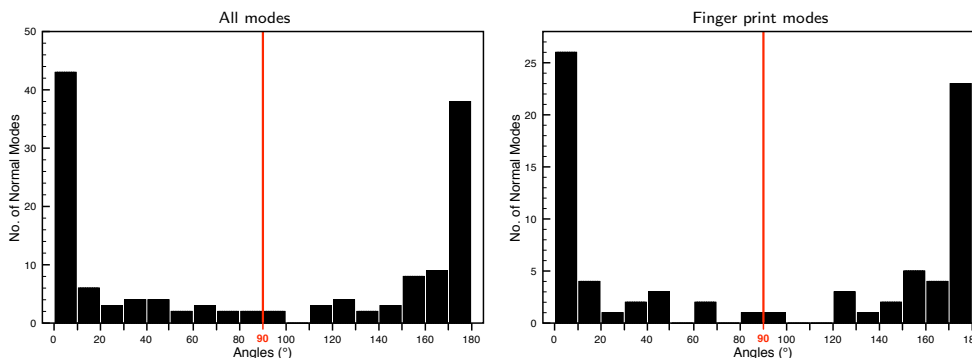


Figure 5.3: Distribution of the values of the ξ angles of molecule **2** (D_3 symmetry). The left panel shows the distribution of all normal modes (ξ_{all}). The right panel shows the distribution of the finger print modes (ξ_{fp}).

and $\sigma(\xi_{fp}) = 65.65^\circ$ for **1**, and $\sigma(\xi_{all}) = 75.47^\circ$ and $\sigma(\xi_{fp}) = 77.64$ for **2**. These values are clearly much larger than the values of the standard deviation of the molecules without symmetry—which are smaller than 40° and mostly between 20° and 30° (see Table 5.2).

The distribution of the angles ξ_{all} and ξ_{fp} of molecules **1** and **2** are shown in Figs. 5.2 and 5.3, respectively. In Figs. 5.2 and 5.3 the horizontal axis represents the angle interval from 0° to 180° (divided into 10° intervals), whereas the vertical axis gives the number of normal modes in a given 10° interval. As can be seen, the distributions of the angles ξ of both molecules have a concave shape with peaks at 0° and 180° . Because they have many modes with angles ξ far from 90° , the molecules **1** and **2** have potentially many robust modes, a fair number of those 0° and 180° modes being expected to be also sufficiently intense.

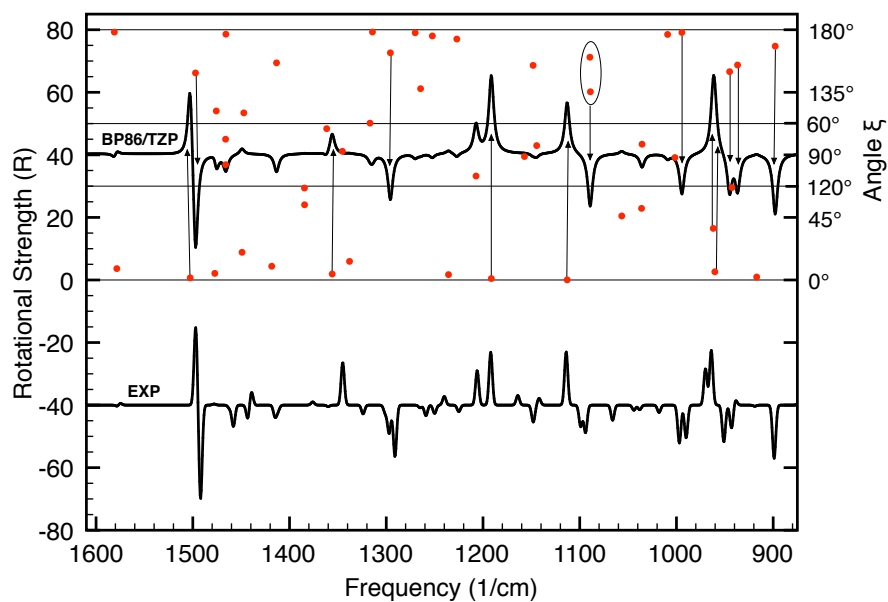


Figure 5.4: Comparison of calculated (BP86/TZP) and experimental (EXP) VCD spectra of molecule **1** (C_2 symmetry).

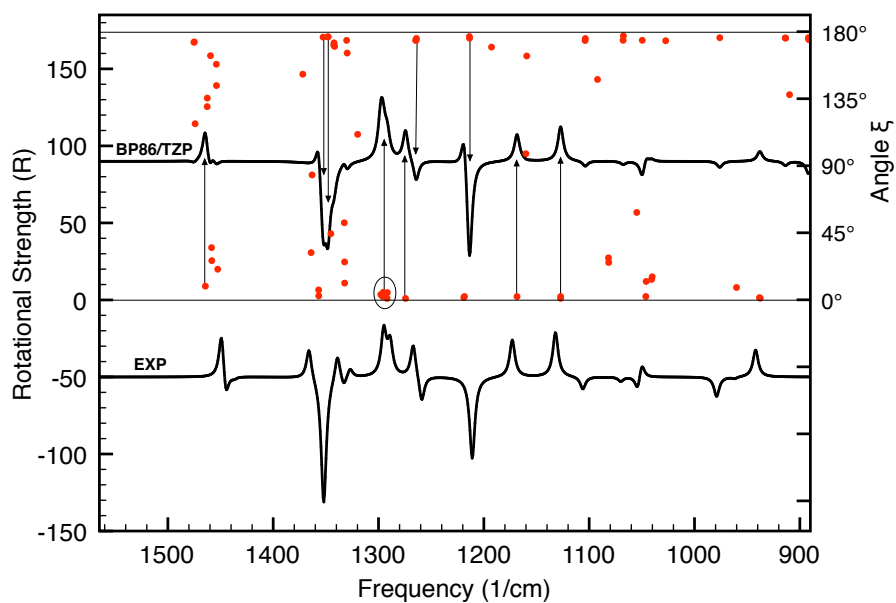


Figure 5.5: Comparison of calculated (BP86/TZP) and experimental (EXP) VCD spectra of molecule **2** (D_3 symmetry).

Figures 5.4 and 5.5 show a comparison of the calculated and experimental VCD spectra of **1** and **2**, respectively. The calculated spectra were obtained from BP86/TZP ADF gas phase calculations on the isolated molecules, the experimental spectra were obtained by Lorentzian broadening of the experimental VCD intensities reported by Stephens et al. [54, 82]. The dots plotted in Figs. 5.4 and 5.5 on top of the VCD spectra indicate the magnitude of the ξ angles of the modes in the calculated spectra. The baseline of the calculated spectra is the 90° line, the Y-coordinate of each dot gives the magnitude of each ξ angle (see the vertical right axis in Figs. 5.4 and 5.5), while the X-coordinate gives the frequency of the mode. The *robust* modes (the modes with significant VCD intensities and values of their ξ angle that differ from 90° by more than 30° degrees) are marked with arrows in Figs. 5.4 and 5.5.

As can be seen, there is a very good agreement between the calculated and experimental VCD spectra of both molecules. All the features that stand out in the VCD spectra of **1** and **2** are associated with *robust* modes. As a matter of fact, even the non-robust modes usually also have the same sign as in the experiment. Finally, we note that the molecules **1** and **2** are very rigid, and as shown in references [54] and [82] these molecules practically have a single conformation populated. Thus, the experimental VCD spectra of both molecules are indeed for the same conformation for which the calculations are performed. We can therefore conclude that in cases like the present ones—rigid molecules with symmetry and therefore many robust modes—it is easy to obtain reliable predictions of the ACs using VCD.

5.4.3 Molecules without symmetry

The rest of the molecules in Fig. 5.1 and Table 5.2 (**3** to **27**) have no symmetry. As already mentioned, the molecules without symmetry have much smaller spread of the ξ values, i.e. $\sigma(\xi)$, around 90° than the molecules with symmetry. Thus, the largest value of $\sigma(\xi_{all})$ is exhibited by **12**, $\sigma(\xi_{all}) = 36.40$, whereas the smallest value is exhibited by **27**, $\sigma(\xi_{all}) = 12.49$ (see Table 5.2). In the case of $\sigma(\xi_{fp})$, the largest value is exhibited by **7**, $\sigma(\xi_{all}) = 39.23$, whereas the smallest value is exhibited by **4**, $\sigma(\xi_{fp}) = 5.44$ (**4** has only 2 finger print modes, both of them with ξ close to 90°).

Approximately 65% of the elements of a Gaussian distribution are situated within one standard deviation from the mean. Because the values of $\sigma(\xi_{all})$ and $\sigma(\xi_{fp})$ of the molecules without symmetry are relatively small, many of the modes of these molecules have ξ that are close to 90° (the approximate mean value), and therefore are *non-robust* modes.

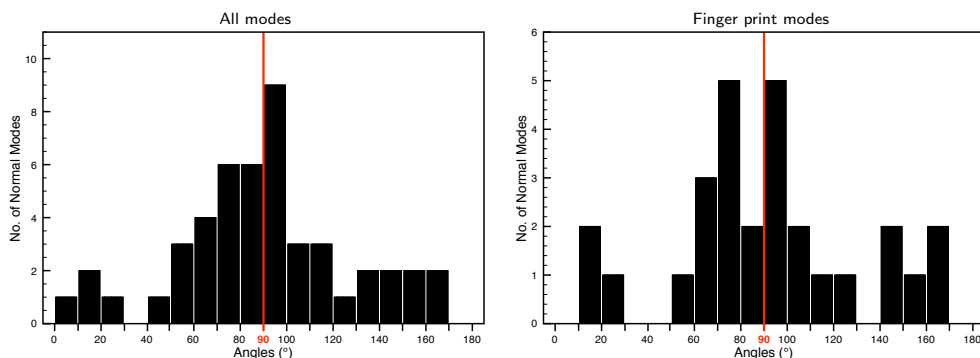


Figure 5.6: Distribution of the values of the ξ angles of molecule **12** (no symmetry). The left panel shows the distribution of all normal modes (ξ_{all}). The right panel shows the distribution of the finger print modes (ξ_{fp}).

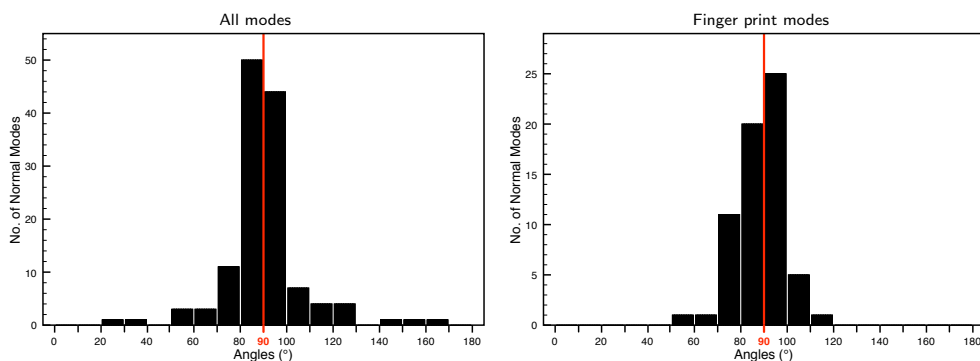


Figure 5.7: Distribution of the values of the ξ angles of molecule **27** (no symmetry). The left panel shows the distribution of all normal modes (ξ_{all}). The right panel shows the distribution of the finger print modes (ξ_{fp}).

As suggested by the data in Table 5.2, all the molecules without symmetry have very similar gaussian-like ξ distributions that are centered approximately on the 90° value. The distribution of the ξ angles of the molecules without symmetry have been carefully investigated. For brevity we will discuss here only two suggestive examples. Figures 5.6 and 5.7 show the distributions of ξ_{all} and ξ_{fp} of molecules **12** and **27**, respectively.

Among the molecules without symmetry, molecule **12** has some of the largest standard deviations $\sigma(\xi_{all})$ and $\sigma(\xi_{fp})$, i.e. 39.08° and 36.40° , respectively. As a result, relatively many of its normal modes have ξ angles that are far from 90° (see Fig 5.6) and therefore are classified as *robust*. Furthermore, **12** is a rigid molecule that does not have much conformational freedom, therefore the experimental VCD spectra (measured in inert solvents such as CCl_4 and CS_2) do

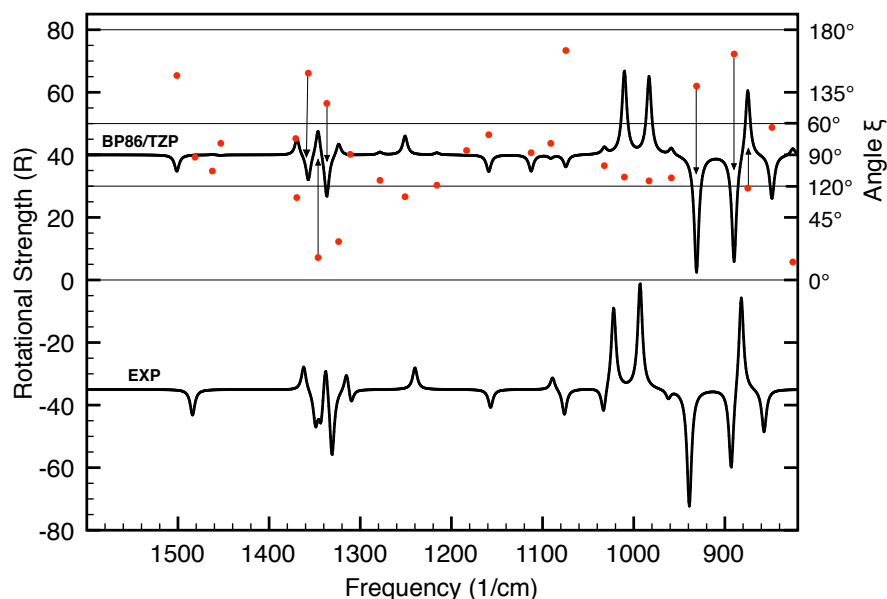


Figure 5.8: Comparison of calculated (BP86/TZP) and experimental (EXP) VCD spectra of molecule **12** (no symmetry).

relate to a single conformer.

Figure 5.8 shows the calculated and experimental VCD spectra of **12**. The calculated spectrum was obtained from a BP86/TZP ADF gas phase calculation on an isolated molecule, the experimental spectrum was obtained by Lorentzian broadening of the experimental VCD intensities measured in CS₂ solvent reported in reference [92]. As before, the dots indicate the values of angles ξ of the modes in the calculated spectra, while the arrows indicate the *robust* modes. The calculated VCD spectrum reproduces very well the experimental one. The *robust* modes all agree in sign and intensity with the experimental spectrum. This allows to conclude that the prediction of the AC of **12** using the comparison of VCD calculation and experiment is a very reliable one. As a matter of fact, also many of the *non-robust* modes in the calculated VCD spectrum of **12** have the correct sign, notably the three intense modes around 850, 980 and 1010 cm⁻¹. This gives the total calculated spectrum a superficially very similar appearance as the experimental one. We should however caution that for the non-robust modes the agreement is somewhat accidental in view of the possible effects of error sources (functional, solvent effects). Indeed, there are also non-robust modes that do have different signs in calculation and experiment, e.g. at 1030 cm⁻¹ and 1090 cm⁻¹, the calculated one at 1110 cm⁻¹ being not visible in experiment. It only

so happens in this molecule that the intense non-robust modes are in agreement with experiment, while the ones that are not have small intensities and therefore are not conspicuous.

It may happen that a molecule has only few robust modes. Consider molecule **27**, which (together with molecule **26**) has the highest number of modes of our set of molecules (132) but which has some of the smallest values for the standard deviations $\sigma(\xi_{all})$ and $\sigma(\xi_{fp})$. As can be seen in Fig. 5.7, most of its modes have angles ξ that are very close to 90° and as a result are *non-robust*. Molecule **27** has only nine robust modes. In fact, only two of the nine robust modes are in the finger print region. Thus, if these robust modes are intense, and are not sensitive to the conformation, they may be used for determination of the AC. (**27** is a very flexible molecule that may adopt many different conformations in solution, but this is a complication we do not address here). However, one should expect to obtain a sub-optimal agreement between the calculated and experimental VCD spectra for molecule **27**.

Finally, we note that the large difference between the standard deviations of the ξ angles of molecules **12** and **27** can be qualitatively understood by looking at their geometrical structures. As shown in section 2.1.4, in achiral molecules the EDTM and MDTM associated with the normal modes are always perpendicular ($\xi = 90^\circ$). Molecule **27** is a very large molecule with many of its normal modes being localized on only one of the four different groups attached to the chiral carbon. Some of these modes, especially the ones localized far from the chiral center, are very similar (almost identical) to the modes of the free group on which they are localized. This is also the case for the APTs and AATs of the atoms that are far from the chiral center (see chapter 4 and [93]). Thus, when such modes are localized on achiral groups, their ξ angles should have values that deviate only slightly from 90° . Molecule **12** on the other hand, is a very small and compact molecule that has two chiral centers. Due to its compactness, molecule **12** has no parts that can behave like isolated achiral molecules and therefore its ξ angles deviate significantly from 90° .

5.5 Summary and conclusions

The sign of the rotational strength of a given mode in a VCD spectrum is determined by the angle ξ made by the EDTM and MDTM of that mode. The modes with $\xi < 90^\circ$ have positive VCD signals ($R > 0$), whereas the modes with $\xi > 90^\circ$ have negative VCD intensities ($R < 0$). However, when ξ is close to 90° , even the smallest perturbation can change ξ across 90° and thus induce a

sign change. Since as shown in chapter 4 (cases **C** and **D**) rotational strengths can have large magnitudes also when ξ is very close to 90° , variation of ξ by few degrees can significantly modify the shape of the VCD spectra if the angle change occurs across 90° . An important perturbation at the experimental side is the influence of the solvent, perturbations at the computational side are change of functional or basis set.

In this chapter we have investigated the distributions of the values of the angles ξ and their dependence on the exchange-correlation functional, using a test group of 27 molecules. The results of the analysis presented in this chapter have validated further the conclusions drawn in chapter 4. That is, the modes in a VCD spectrum can be classified as *robust* and *non-robust*. The *robust* modes have rotational strengths with characteristic sign that is not sensitive to small perturbations (either of computational or experimental nature) and as a result should be correctly predicted by calculations. On the other hand, the signs of the rotational strengths of *non-robust* modes can be changed even by the smallest perturbation and as a result should not be trusted.

The analysis of the differences between BP86 and OLYP calculations has shown that:

1) The differences, $\Delta\xi$, between the ξ angles of BP86–OLYP pairs of modes with $\Omega \geq 0.90$ and large EDTMs and MDTMs were always smaller than 30° . It is therefore clear that the two functionals will not predict different signs for the rotational strengths of modes with angles ξ that differs from 90° by more than 30° (unless perhaps if it mixes strongly with another mode, i.e. when $\Omega \leq 0.90$).

2) When a mode has very small EDTM and/or MDTM, a very large $\Delta\xi$ can be encountered ($\Delta\xi > 70^\circ$ are not unusual). Thus, quite often the BP86 and OLYP *Rs* have different signs.

Based on 1) and 2) we conclude that the *robust* modes are characterized by angles ξ that differ from 90° by at least 30° and by rotational strengths of significant magnitude, i.e. large EDTMs and MDTMs. *Non-robust* modes are characterized by ξ angles that are close to 90° and/or by rotational strengths of small magnitude, i.e. small EDTM and/or MDTM, where we have defined “small” earlier.

Since the sign of the rotational strengths of *non-robust* modes are not reliable, only *robust* modes should be considered when determining the absolute configuration of chiral molecules using VCD. Thus, in order to have reliable VCD prediction it is required that the modes that are used to determine the AC of the molecule are *robust*. On the other hand, sign differences between experimental and calculated VCD signals should be of no concern if the signals are associated with *non-robust* modes.

Although this definition of *robustness* is very useful, it is not a 100% guarantee that a robust mode will not change sign. Occasionally, sign differences are encountered also for modes which are *robust* according to the above criteria. We have already mentioned that robust modes may mix strongly with another mode with similar frequency in response to the small change induced by the change of functional (cf. BP86–OLYP mode pairs with overlaps smaller than 0.90, i.e. $\Omega \leq 0.90$). The “mixed” modes differ significantly from the initial modes (an overlap of 0.70 means that the two modes differ by 51%) and as a result they often have rotational strengths that are very different from the rotational strengths of the initial modes. Such situations also occur in experiment, i.e. the small perturbations present in experiment (e.g solvent effects) may cause normal modes with similar frequencies to mix (such an example will be discussed in the next chapter). Typically less than 10% of the modes of a molecule are in this category. In case different signs are encountered for one or a few of the *robust* modes, the strategy to be followed is to examine whether the cause could be mixing of modes due to a perturbation. From the displacement vectors of the calculated mode (e.g., do they involve atoms that may participate in hydrogen bonding with the solvent?) and taking into account the type of solvent used, one may detect if there is the possibility of mixing of modes by solvent effects. In the calculations, one can check on proximity of other modes. So if in the comparison of calculation to experiment the signs of most of the robust modes agree, but a few anomalous sign changes are observed, one may assume this is caused by mode mixing. This can then be confirmed by performing a second calculation where the interaction is explicitly specified (e.g calculation for the hydrogen-bonded complex) or a computational perturbation (different functional) is applied.

The analysis of the distribution of the values of the ξ angles has shown that there is a significant difference between the distributions of the molecules with and without symmetry. Due to constraints imposed by symmetry on the orientation of the EDTMs and MDTMs, the distribution of the values of the angles ξ has a concave shape with peaks at 0° and 180° . The values of the angles ξ of the chiral molecules without symmetry on the other hand, have gaussian-type distributions that have a maximum at about 90° . This means that molecules with symmetry have many more *robust* modes than the molecules without symmetry. Thus, under normal conditions it is to be expected that better agreement will be obtained between calculated and experimental VCD spectra for molecules with symmetry. As proven by the multitude of literature reports, good agreement between calculation and experiment may also be obtained for molecules without symmetry. As we have shown in this study, this happens when the molecules have enough *robust* modes in the finger print region. However, it is important to realize that

there are also cases when the molecules without symmetry have very few *robust* modes in the finger print region (e.g. **27** has only two *robust* modes in the finger print region). In such cases a sub-optimal agreement between calculation and experiments is usually obtained.

We should caution, however, against overinterpreting the "prediction" of VCD for such molecules if based on a superficial comparison of the experimental and calculated spectra. Only *robust* modes should be considered when determining the absolute configuration of chiral molecules using VCD. We advocate that codes that calculate vibrational rotational strengths should output the angles ξ and the magnitude of the EDTMs and MDTMs. This will enable to assign the *robustness* of each mode in the calculated VCD spectrum which will greatly aid the interpretation of the differences between the calculation and experiment.

Chapter 6

Enhancement of IR and VCD intensities due to charge transfer

6.1 Introduction

In this chapter we investigate the enhancement of the VCD intensities of the N–H stretching modes of the tris(ethylenediaminato)cobalt(III) transition metal complex induced by the association of the chloride ions.

The tris(ethylenediaminato)cobalt(III) complex, $[\text{Co}(\text{en})_3]^{3+}$, is a prototype chiral transition metal complex. Over the years, its optical activity has been extensively studied using spectroscopic techniques like anomalous X-ray [94, 95], electronic circular dichroism [96–100], NMR [101–103], and VCD [55, 84]. The configurations of the $[\text{Co}(\text{en})_3]^{3+}$ complex can be classified as follows. A tris(bidentate) complex can exist in a right-handed (Δ) and left-handed (Λ) form (see Fig. 6.1), using the pseudo-threefold axis of the octahedron as the defining axis.

The Δ and Λ form can exist in various conformations dependent on the conformations of the individual bidentate ligands. An ethylenediamine ligand coordinates to the metal center with the two N lone pairs, forming a puckered five-membered ring. When viewing the metal through the midpoint of the C–C bond, there are two possible conformations for the N–C–C–N bonds (see Fig. 6.2): either the C atom to the left is down and the C atom to the right is up (λ conformation), or the C atom to the left is up and the C atom to the right is down (δ conformation).

Both the Λ and Δ configurations of $[\text{Co}(\text{en})_3]^{3+}$ can therefore exist in four different conformations labeled as $\delta\delta\delta$, $\delta\delta\lambda$, $\delta\lambda\lambda$ and $\lambda\lambda\lambda$. In the Λ enantiomer the δ en ligand has the C–C bond nearly parallel to a C_3 axis, while the λ en

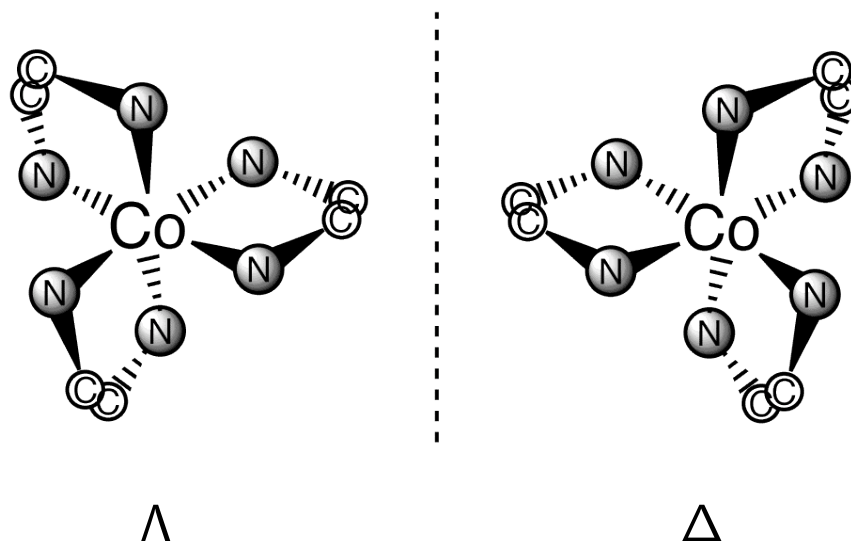


Figure 6.1: Schematic representations of Δ and Λ conformations of Co(en)_3^{3+} .

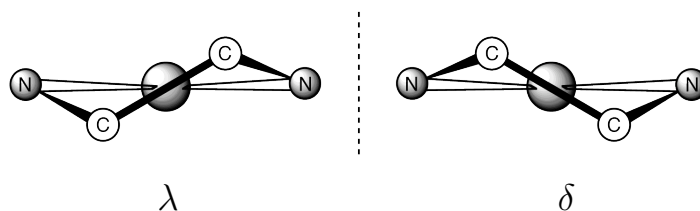


Figure 6.2: Schematic representations of λ and δ conformations of ethylenediamine ligand coordinates to the metal center.

form has the C–C bond oblique to the C_3 axis [104] (see Fig. 6.3 left panel). In the Δ enantiomer the situation is reversed, the C–C bond of the λ *en* ligand is nearly parallel to a C_3 axis, while the C–C bond of the λ *en* ligand is oblique to the C_3 axis (see Fig. 6.3 right panel).

From now on we will restrict ourselves to the Λ configurations, and note that *mutatis mutandis* a similar situation will hold for the enantiomeric Δ forms. Now in the $\Lambda - \delta\delta\delta$ conformation one can distinguish two sets of three N atoms. The first set forms a triangle around the positive z axis, whereas the second set forms a triangle around the negative z axis (the z axis is chosen along the C_3 axis). An important point for the study presented in this chapter is the orientation of the two N–H bonds at each N atom. As can be seen in Fig. 6.4 (also in Fig. 6.5) one N–H bond (the "axial" one) is practically parallel to the z axis, while the other N–H bond (the "equatorial" one) is almost perpendicular to the first one and to the z axis.

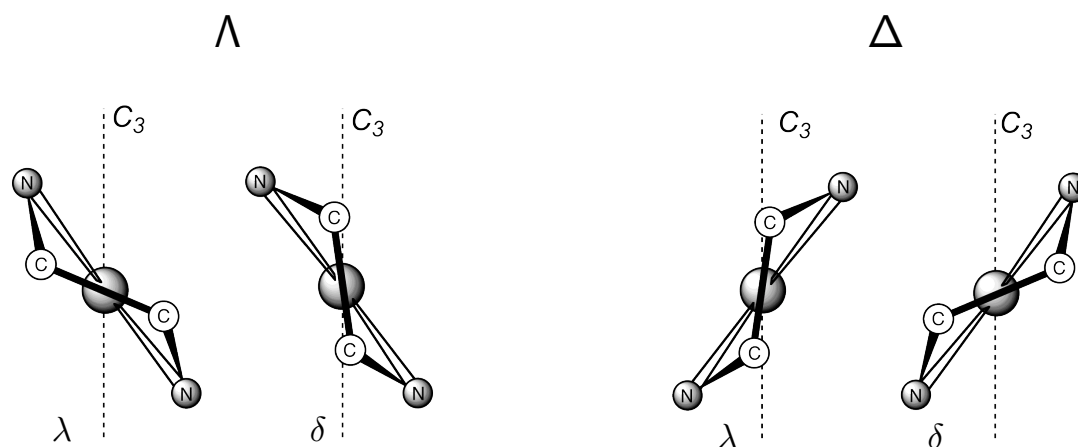


Figure 6.3: Schematic representation showing the orientation of the C–C bond with respect to the C_3 symmetry axis in the λ and δ en-rings coordinated to the metal center for the Λ (left panel) and Δ (right panel) configurations.

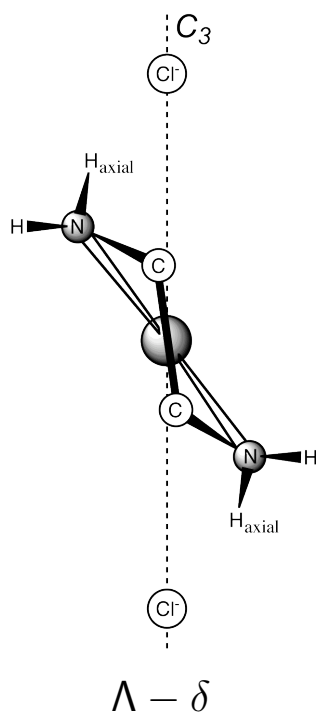


Figure 6.4: Schematic representation showing the orientation of the N–H_{axial} bonds with respect to the C_3 symmetry axis in a δ en-ring coordinated to the metal center for the Λ configuration.

A series of experimental, and combined experimental and computational VCD studies by Nafie et al. [55, 84] have shown that in the presence of excess chloride ions a specific conformation of Λ $[\text{Co}(\text{en})_3]^{3+}$ complex is stabilized by chloride ion association. This is the $\Lambda - \delta\delta\delta$ conformation. When two associated chloride anions are located at the positive and negative z axis, which as already mentioned, is also the C_3 axis, the axial N–H bonds form donor-acceptor bonds with the Cl^- (as the donor) by virtue of the relatively low-lying σ^* of the N–H bond. Three of the six N–H $\cdots\text{Cl}^-$ donor-acceptor bonds are pointing in the positive z direction, while the other three N–H $\cdots\text{Cl}^-$ bonds are pointing approximatively in the negative z direction (see Fig 6.5 right panel).

Here we investigate more closely the most favorable conformer as identified in reference [55], the $\delta\delta\delta$ conformer of $\Lambda - [\text{Co}(\text{en})_3]^{3+} \cdots 2\text{Cl}^-$, $\Lambda - \delta\delta\delta \cdots 2\text{Cl}^-$ for short. Our interest is focused on the enhancement of the IR/VCD intensities of the N–H stretching modes that involve displacements of the protons towards the associated chloride ions (N \leftrightarrow H \cdots Cl stretching modes). The association of the chloride ions induces a spectacular increase in the IR and VCD intensities of the N \leftrightarrow H \cdots Cl stretching modes, and a large redshift of the normal mode frequencies. In vibrational absorption spectroscopy, the effects described above are well known and documented [79, 80], their presence in IR spectra being long used as experimental evidence for intra- and inter-molecular hydrogen bond formation (the effects are more pronounced in the latter). In VCD spectroscopy on the other hand, the phenomenon has been little investigated. In chapter 4 using the benzoyl-benzoic acid – NH_3 complex (BBA– NH_3) as the test molecule, we have shown that the same mechanism is responsible for the enhancement of both IR and VCD intensities. However, since the VCD intensities are determined also by the cosine of the angle, ξ , between the electric and magnetic dipole transition moment, which often is close to zero since ξ is often very close to 90° , we asked the question whether the enhancement of the VCD intensities could be seen experimentally.

To the best of our knowledge the only published experimental evidence of VCD intensities enhanced by the mechanism described above are the VCD spectra of $[\text{Co}(\text{en})_3]^{3+}$ for the N–H/C–H stretching region measured with excess chloride ions presented by Nafie et al. in references [55, 84]. Since the origin of the enhancement was not addressed in the above mentioned studies, and since for this system (unlike for BBA– NH_3) the results of the analysis presented in chapter 4 can be directly compared to experimental data, in this chapter we analyze in detail the various contributions of the electric and magnetic dipole transition moments of the N \leftrightarrow H \cdots Cl modes. The aim being a better understanding of the mechanism responsible for the enhancement of the VCD intensities.

The BBA–NH₃ complex studied in chapter 4 had a single mode that exhibited an enhancement of its IR and VCD intensities upon complexation. It was an O–H···N stretching mode that involved the displacement of a single proton. The $\Lambda - \delta\delta\delta \cdots 2\text{Cl}^-$ complex on the other hand, has six N \leftrightarrow H···Cl stretching modes. Five of them exhibit an enhancement of the IR and VCD intensities, each of these modes involving displacements of six protons. As will be shown, the study of the more complicated $\Lambda - \delta\delta\delta \cdots 2\text{Cl}^-$ complex will reveal more aspects that play a role in the enhancement and therefore provide more insight into the enhancement mechanism.

Finally, we note that besides the calculations in reference [55], theoretical calculations of the VCD intensities enhanced upon hydrogen bonding were also reported by Sadlej et al. [70].

6.2 Theory

The IR intensity for the fundamental transition ($|0\rangle \rightarrow |1\rangle$) of the i^{th} vibrational mode are given by the dipole strength (D) [13]:

$$D(i) = |\vec{E}_{01}(i)|^2 \quad (6.1)$$

As shown in chapter 2 the VCD intensity for the $|0\rangle \rightarrow |1\rangle$ of the i^{th} is given by rotational strength (R):

$$R(i) = \vec{E}_{01}(i) \cdot \text{Im}[\vec{M}_{10}(i)] \quad (6.2)$$

In Eqs. (6.1) and (6.2), $\vec{E}_{01}(i)$ and $\vec{M}_{10}(i)$ are the electric and magnetic dipole transition moments associated with the first vibrational transition ($|0\rangle \rightarrow |1\rangle$) of the i^{th} normal mode.

Within the harmonic approximation the transition dipole moments $\vec{E}_{01}(i)$ and $\vec{M}_{10}(i)$ can be written as a sum of atomic contributions (see chapter 2 section 2.2.5):

$$\vec{E}_{01}(i) = \sum_{\lambda} \vec{E}_{01}^{\lambda}(i), \quad \vec{M}_{10}(i) = \sum_{\lambda} \vec{M}_{10}^{\lambda}(i) \quad (6.3)$$

where the Cartesian components of \vec{E}_{01}^{λ} and \vec{M}_{10}^{λ} are defined in Eqs (2.145) and (2.146), respectively.

Further, since the APTs and the AATs have electronic and nuclear contributions, Eqs (2.147) and (2.148), the electric and magnetic dipole transition moments can be further decomposed into total electronic (el) and total nuclear (nuc) contributions:

$$\vec{E}_{01}(i) = \vec{E}_{01}^{el}(i) + \vec{E}_{01}^{nuc}(i), \quad \vec{M}_{01}(i) = \vec{M}_{01}^{el}(i) + \vec{M}_{01}^{nuc}(i) \quad (6.4)$$

Finally, as shown in chapter 3 the electronic contributions $E_{\alpha\beta}^\lambda$ and $I_{\alpha\beta}^\lambda$ of the APTs and AATs, respectively, can be decomposed in contributions from the occupied molecular orbitals (MO):

$$E_{\alpha\beta}^\lambda = \sum_{j_{occ}} E_{\alpha\beta}^\lambda(j_{occ}), \quad I_{\alpha\beta}^\lambda = \sum_{j_{occ}} I_{\alpha\beta}^\lambda(j_{occ}) \quad (6.5)$$

The MO contributions $I_{\alpha\beta}^\lambda(j_{occ})$ and $E_{\alpha\beta}^\lambda(j_{occ})$ are given by Eqs (3.10) and (3.13), respectively.

6.3 Computational Details

As in the previous chapters, all calculations (geometry optimization and IR/VCD calculations) were performed using the ADF program package [24–26]. The BP86 and OLYP functionals and the TZP basis set were used in all the calculations. The geometries have been optimized separately for each choice of functional using the optimized described in reference [44]. Very tight convergence criteria have been applied for the geometry optimization (10^{-6} Hartree for the energy and 10^{-4} Hartree/Ångstrom for the gradients).

The IR and VCD spectra obtained with BP86 and OLYP were very similar. However, since the frequencies of the $\text{N} \leftrightarrow \text{H} \cdots \text{Cl}$ stretching modes calculated using OLYP were closer to the experimental ones than the BP86 ones, only the OLYP results will be considered. The analysis of the normal modes and of the various contributions of the electric and magnetic transition dipole moments was done using the ToolsVCD program. ToolsVCD requires data saved during an ADF IR/VCD calculation

For a direct comparison to experiment the calculated dipole and rotational strengths have been transformed to molar absorptivity (ϵ) and differential molar absorptivity ($\Delta\epsilon$), respectively, using the following formulas [16, 50]:

$$\epsilon(\nu) = \frac{8\pi^3 N_A}{3 \cdot 2.303 h c} \nu D_i(\nu) \quad (6.6)$$

$$\Delta\epsilon(\nu) = \epsilon_L(\nu) - \epsilon_R(\nu) = \frac{32\pi^3 N_A}{3 \cdot 2.303 h c} \nu R_i(\nu) \quad (6.7)$$

where N_A is Avogadro's number, h is Planck constant, c is the speed of light in vacuum, and $D_i(\nu)$ and $R_i(\nu)$ are the dipole and rotational strengths associated to the i normal mode, ν is the frequency of the normal mode i , and $\epsilon_L(\nu)$ and $\epsilon_R(\nu)$ are the molar absorptivities for left and right circularly polarized light.

The VCD spectra were simulated by representing the peaks as Lorentzian bands [50]. A half-width of 30 cm^{-1} was used for the associated NH-stretching

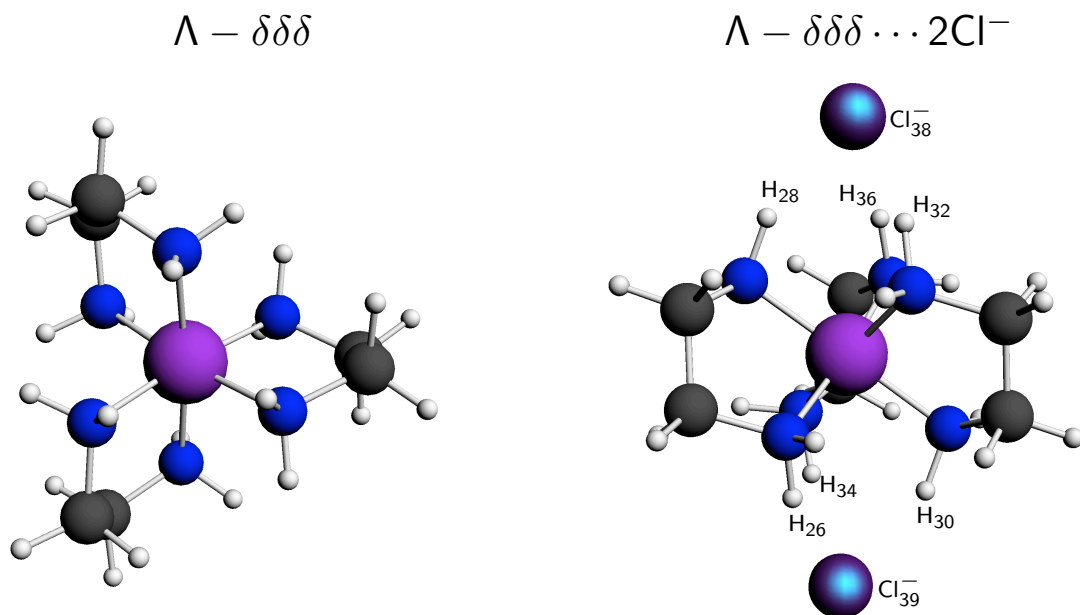


Figure 6.5: The OLYP/TZP optimized structures of $\Lambda - \delta\delta\delta$ and $\Lambda - \delta\delta\delta \cdots 2\text{Cl}^-$. Left panel: $\Lambda - \delta\delta\delta$ viewed along the C_3 axis. Right panel: $\Lambda - \delta\delta\delta \cdots 2\text{Cl}^-$ viewed along the C_2 axis.

modes, and of 15 cm^{-1} for free N-H and C-H stretches [55]. To align the calculated and experimental spectra, the OLYP/TZP frequencies were scaled by 1.0766 (N \leftrightarrow H \cdots Cl stretching) and by 0.9643 (free N-H/C-H stretching). The B3LYP/LanL2DZ frequencies were scaled according to reference [55], by 1.03 (N \leftrightarrow H \cdots Cl stretchings) and by 0.94 (free N-H/C-H stretchings).

6.4 Results and Discussions

The $\Lambda - \delta\delta\delta$ molecule and the $\Lambda - \delta\delta\delta \cdots 2\text{Cl}^-$ complex (with the two Cl^- ions situated on the C_3 axis) are depicted in Fig. 6.5. In the panel to the left the complex is oriented in the standard way, with one N-Co-N axis as (vertical) z -axis. One is looking down the C_3 axis and the three N-H_{axial} bonds pointing approximately towards the observer are clearly visible. In the panel to the right the C_3 axis is taken as vertical axis, which shows the orientation of the C-C bonds approximately along this same direction, and the favorable position of the Cl^- ions for interaction with the three N-H_{axial} bonds pointing to each of them.

Table 6.1 gives the experimental and calculated frequencies, and the IR and VCD intensities of the N-H stretching modes. The experimental data are taken

A) Experiment					B) OLYP/TZP calculation				
$\Lambda\text{--}[\text{Co}(\text{en})_3]^{3+}$ in D_2O					$\Lambda - \delta\delta\delta$				
Sym.	IR		VCD		Freq.	IR		VCD	
	Freq.	ϵ_{max}	Freq.	$10^3\Delta\epsilon_{max}$		ϵ_{max}	$10^3\Delta\epsilon_{max}$	Sym.	Label
E	–	–	3060	–1.5	3263.7	8.9	+5.1	E	94/95
E	–	–	3105	+2.5	3265.2	16.8	+20.1	E	96/97
A_2	3130	486	3105	–1.3	3266.5	56.6	–55.2	A_2	98
E	–	–	3215	+4.0	3320.0	2.8	–10.4	E	100/101
A_2	3242	561	3276	+16.0	3322.0	11.8	–7.8	E	102/103
					3323.1	47.4	+49.8	A_2	104
$\Lambda\text{--}[\text{Co}(\text{en})_3]^{3+}$ in $\text{DMSO-}d_6$ with excess Cl^-					$\Lambda - \delta\delta\delta \cdots 2\text{Cl}^-$				
Sym.	IR		VCD		Freq.	IR		VCD	
	Freq.	ϵ_{max}	Freq.	$10^3\Delta\epsilon_{max}$		ϵ_{max}	$10^3\Delta\epsilon_{max}$	Sym.	ξ
E	3041	792		+200	3015.2	41.1	–244.1	$1E$	180°
A_2	3125	1098		–89	3019.4	129.4	+296.9	$2E$	0°
					3148.6	1973.8	–67.8	A_2	180°

Table 6.1: Experimental and calculated frequencies, IR and VCD intensities of the N–H stretching modes of $\Lambda\text{--}[\text{Co}(\text{en})_3]^{3+}$. A) Experimental data taken from [55, 84]: $\Lambda\text{--}[\text{Co}(\text{en})_3]^{3+}$ 0.10 M in D_2O (upper panel), and $\Lambda\text{--}[\text{Co}(\text{en})_3]^{3+}$ 0.060 M with excess Cl^- (0.6 M LiCl) in $\text{DMSO-}d_6$ (lower panel). B) OLYP/TZP calculation for the $\Lambda - \delta\delta\delta$ molecule (upper panel) and for the $\Lambda - \delta\delta\delta \cdots 2\text{Cl}^-$ complex (lower panel). The calculated frequencies were scaled by 1.0766 ($\text{N}\leftrightarrow\text{H}\cdots\text{Cl}$ stretching) and by 0.9643 (free N–H stretching). Units: Freq.(1/cm) and ϵ_{max} ($10^3 \text{ cm}^2/\text{mol}$).

from references [84] and [55].

In Section A of Table 6.1 (left panel) the experimental measurements for $\Lambda\text{--}[\text{Co}(\text{en})_3]^{3+}$ 0.10 M with 1 M DCl in D_2O are compared with those for $\Lambda\text{--}[\text{Co}(\text{en})_3]^{3+}$ 0.060 M with 0.6 M LiCl in $\text{DMSO-}d_6$ (a 10-fold excess of chloride anion per complex). We note that out of the 12 N–H modes there are two (with A_1 symmetry) that have zero intensity. Furthermore, in the experiment some modes have such low intensity that they are not observed (e.g. the E modes in the IR in D_2O solution). In the solutions with halide ions the broadening of the signals leads to even fewer N–H stretching modes being resolved in the experimental spectra.

Section B of Table 6.1 (right panel) compares the calculated (OLYP/TZP) data of the $\Lambda - \delta\delta\delta$ molecule with those of the $\Lambda - \delta\delta\delta \cdots 2\text{Cl}^-$ complex. The angles ξ (between the electric and magnetic dipole transition moments) of the $1E$, $2E$ and A_2 modes of the chloride complex are also given in Section B of Table 6.1.

As discussed in reference [84], the D_2O solution with acid (DCl) has little hydrogen bonding of the N–H groups to the halide, compared to the $\text{DMSO-}d_6$

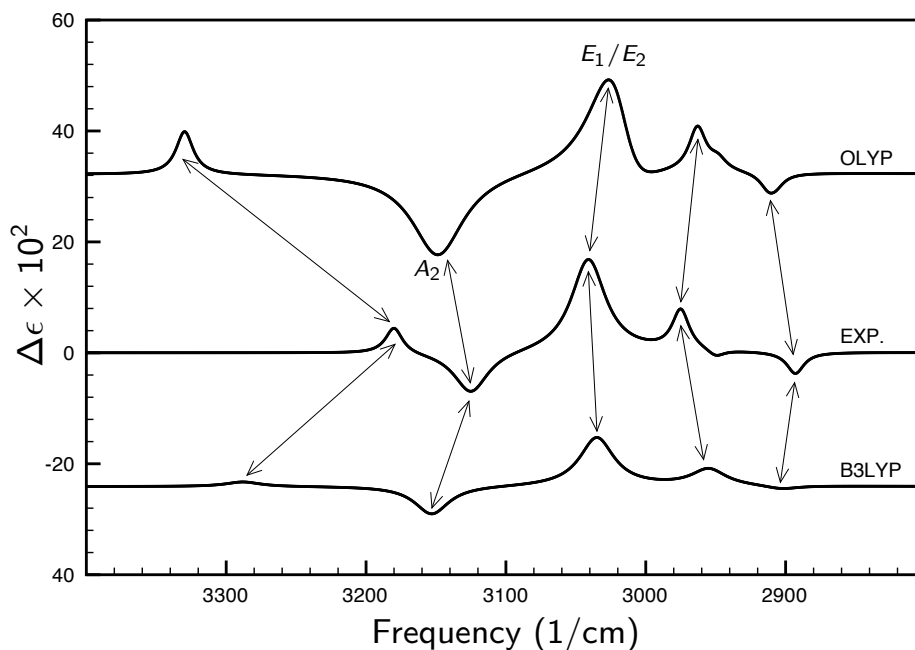


Figure 6.6: Comparison of experimental and calculated (OLYP/TZP, B3LYP/LanL2DZ) VCD spectra for the CH/NH stretching frequency region. The experimental spectrum was measured for Λ -[Co(en)₃]³⁺ 0.060 M with 0.6 M LiCl in DMSO-*d*₆ (a 10-fold excess of chloride anion per complex). The experimental and B3LYP spectra were taken from reference [55].

solution with LiCl, because of strong solvation of the Cl⁻ ions in D₂O, which is absent in DMSO-*d*₆ which has a much lower dielectric constant and is aprotic. This can be clearly seen when comparing, the experimental IR and VCD intensities measured in DMSO-*d*₆ solution with excess chloride and those measured in D₂O solution (see Table 6.1). Thus, in case of the IR intensities a two-fold increase is observed for the *A*₂ modes, and a significant but not quantifiable increase for the *E* modes since those are not observed in the systems without Cl⁻ complexation. In the case of VCD, an enhancement of the intensities of 5 up to 133-fold is observed. The intensity enhancements are also accompanied by frequency shifts towards red of about 100-150 cm⁻¹. The same trend is seen also when looking at the calculated data, i.e. upon chloride association an increase in magnitude up to 40-fold is observed for both IR and VCD intensities along with a large redshift of the normal mode frequencies (which are in the range 3260–3320 cm⁻¹ in $\Lambda - \delta\delta\delta$ and in the range 3015–3148 cm⁻¹ in $\Lambda - \delta\delta\delta \cdots 2\text{Cl}^-$).

Figure 6.6 shows a comparison between the experimental VCD spectrum of Λ -[Co(en)₃]³⁺ measured in DMSO-*d*₆ with excess of chloride ions and the

calculated VCD spectra of $\Lambda - \delta\delta\delta - 2\text{Cl}^-$ obtained using OLYP/TZP and B3LYP/LanL2DZ, for the CH/NH stretching region. The B3LYP/LanL2DZ spectrum was taken from reference [55]. As can be seen the experimental and calculated (OLYP and B3LYP) VCD spectra are in very good agreement. Intensity wise, the OLYP/TZP spectrum reproduces the experimental spectrum somewhat better than B3LYP/LanL2DZ spectrum. Frequency wise, the B3LYP functional is somewhat better (the frequencies of the B3LYP and OLYP $\text{N}\leftrightarrow\text{H}\cdots\text{Cl}$ stretching modes were scaled by 0.9643 and 1.0766, respectively). We note that a comparison between the experimental IR/VCD spectra measured in D_2O and the calculated spectra of the isolated $\Lambda - \delta\delta\delta$ molecule is irrelevant because the experimental spectrum is strongly perturbed as indicated by the low frequency of the N–H stretching modes.

Thus, even though the OLYP functional overestimates both the intensities and the frequency shifts whereas B3LYP underestimates them, we can conclude based on the comparisons done in Table 6.1 and Fig. 6.6, that the DFT calculations give a good description of the phenomena observed experimentally upon chloride association to the $\Lambda - [\text{Co}(\text{en})_3]^{3+}$ molecule.

Beside the dramatic effects of chloride complexation on the intensities and frequencies there are two more details that should be pointed out about the data listed in Table 6.1 for the chloride complex. First, although the A_2 modes have the largest IR intensities (exp.: 1098 for A_2 vs. 792 for E ; calc.: 1973.8 for A_2 vs. 129.4 for $2E$ and 41.1 for $1E$), their absolute VCD intensity is the smallest (exp.: 89 for A_2 vs. 200 for E ; calc.: 67.8 for A_2 vs. 296.9 for $2E$ and 244.1 for $1E$). Since $\cos\xi$ is either 1 or -1 (ξ is 0° or 180°) and therefore is not influencing the magnitude of the VCD intensities, the very different behavior of the IR and VCD intensities of the A_2 mode on the one hand and the E modes on the other hand is rather striking and calls for an explanation. Second, the values of the ξ angles of the three $\text{N}\leftrightarrow\text{H}\cdots\text{Cl}$ modes are either 0° or 180° . Thus, these modes are robust modes [78], i.e. the sign of their rotational strengths is accurately predicted by calculations. As seen, the calculated spectra reproduce well the experimental spectrum.

In IR spectroscopy, the enhancement of the intensities is a consequence of the transfer of charge from the associated ions into the N–H bond [79, 80]. As discussed in chapter 4 section ?? (Case E) the VCD enhancement has the same origin. However, the different behavior of the A_2 intensity with respect to the E intensities in VCD compared to IR already indicates that the explanation in VCD is more complex. We will for the moment take the charge transfer effects in the vibrational motion, i.e. increasing charge transfer from Cl^- into the $\sigma^*(\text{N}-\text{H}_{\text{axial}})$ orbitals during $\text{N}-\text{H}_{\text{axial}}$ stretch, for granted, and we will deal first (in section

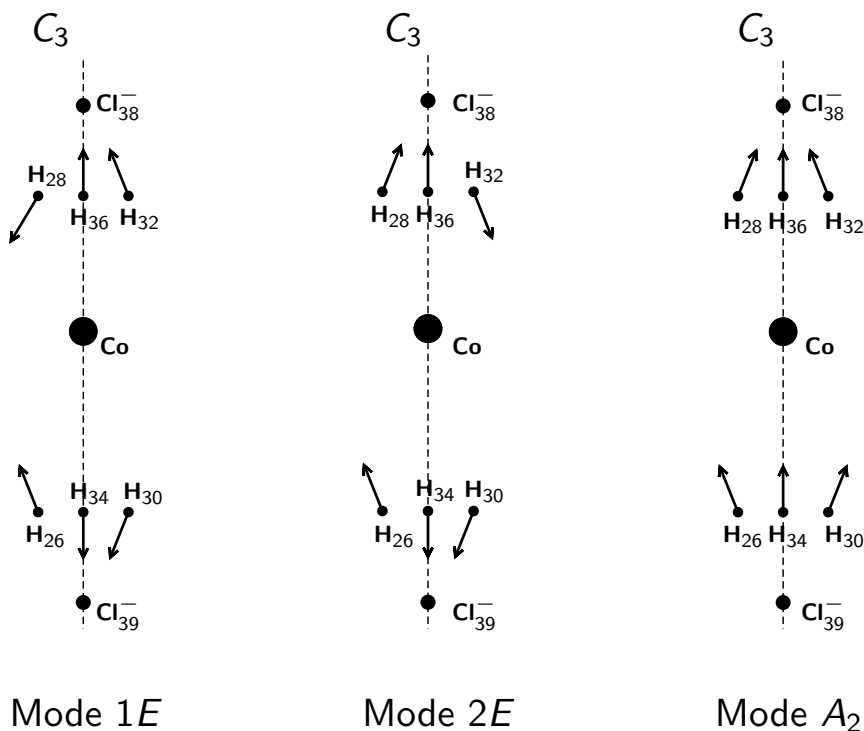


Figure 6.7: Schematic representation of the $\text{N} \leftrightarrow \text{H} \cdots \text{Cl}$ stretching modes of $\Lambda - \delta\delta\delta \cdots 2\text{Cl}^-$. For the modes $1E$ and $2E$ only one of the degenerate mode pair is shown.

6.4.2) with the central topic of this chapter, namely a detailed analysis of how these charge motions affect the electric and magnetic dipole transition moments and therefore the various intensities. Then in the following section (6.4.3) we will turn to a discussion of how exactly the charge density responds to the nuclear motions of the vibrational modes.

6.4.1 Normal mode analysis

The N–H stretching modes of both $\Lambda - \delta\delta\delta$ and $\Lambda - \delta\delta\delta \cdots 2\text{Cl}^-$ have been analyzed by visualizing their nuclear displacements. In the N–H stretching modes of the bare $\Lambda - \delta\delta\delta$ complex both hydrogens attached to a nitrogen atom move (in phase or out of phase) with similar amplitudes. Upon association of the chloride ions the N–H stretching modes of the bare $\Lambda - \delta\delta\delta$ system have mixed in such a way that in the resulting modes the equatorial and axial N–H stretches are uncoupled. Thus, in the $\text{N} \leftrightarrow \text{H} \cdots \text{Cl}$ modes of the chloride complex we will be investigating only the hydrogen atoms involved in the inter-molecular bond (the axial hydrogens H_{axial}) are moving.

$\Lambda - \delta\delta\delta \cdots 2\text{Cl}^-$	$\Lambda - \delta\delta\delta$		
Mode	Mode No.	Coef.	Overlap
$1E$	94	-0.1208	
	95	-0.1013	
	96	0.6512	
	97	0.3370	0.99
	100	0.2108	
	102	0.5140	
	103	0.3439	
$2E$	94	0.4399	
	95	-0.5688	
	97	0.1242	
	100	-0.1870	0.99
	101	0.6136	
	102	-0.1103	
	103	0.1799	
A_2	98	-0.6970	0.99
	104	0.7118	

Table 6.2: Decomposition of the $\text{N} \leftrightarrow \text{H} \cdots \text{Cl}$ modes $1E$, $2E$ and A_2 of $\Lambda - \delta\delta\delta \cdots 2\text{Cl}^-$, which are mostly N-H_{axial} stretches, into (axial and equatorial) N-H stretching modes of the $\Lambda - \delta\delta\delta$ free molecule. The mixing coefficients are inner products between the normalized vector consisting of all x, y, z nuclear displacements of a mode of the molecular complex ($1E$, $2E$ or A_2) with the similar vectors representing the most important modes of the free molecule. The overlaps (inner product squared of a mode of the complex with the linear combination of mode-vectors of the free molecule) are calculated as the sum of the squared mixing coefficients. Only the modes that had a mixing coefficient with absolute value larger than 0.1 are listed.

There are six $\text{N} \leftrightarrow \text{H} \cdots \text{Cl}$ stretching modes, one A_1 , one A_2 , and two two-fold degenerated modes of E symmetry (labeled $1E$ and $2E$). Since the complex has D_3 symmetry, the A_1 mode is IR/VCD inactive and will not be further discussed. A schematic representation of the $\text{N} \leftrightarrow \text{H} \cdots \text{Cl}$ modes $1E$, $2E$ and A_2 is given in Fig. 6.7.

The N-H modes of the free $\Lambda - \delta\delta\delta$ molecule that mix to form the modes $1E$, $2E$ and A_2 of the complex and their mixing coefficients are given in Table 6.2. As discussed in chapter 5 section 5.3 the mixing coefficients are inner products between the normalized $3N$ -dimensional vectors characterizing the modes (which have as components the x, y, z -displacements of all nuclei) of the complex $\Lambda -$

$\delta\delta\delta\cdots 2\text{Cl}^-$ of the parent molecule $\Lambda - \delta\delta\delta$. The modes of $\Lambda - \delta\delta\delta\cdots 2\text{Cl}^-$ can almost perfectly be represented as linear combinations of the modes of the free molecule ($\Lambda - \delta\delta\delta$). This follows from the fact that the inner products between the modes $1E$, $2E$ and A_2 of $\Lambda - \delta\delta\delta\cdots 2\text{Cl}^-$ and the corresponding linear combinations of the $\Lambda - \delta\delta\delta$ modes are practically 1.0 (see Table 6.2).

6.4.2 The enhancement of IR/VCD intensity

The mechanism of the intensity enhancement

As shown in chapter 4 section ?? (Case E) the mechanism and the magnitude of the enhancement of the IR/VCD intensities can easily be understood by looking at the nuclear and electronic contributions of the total electric and magnetic dipole transition moments.

Table 6.3 gives the nuclear and electronic contributions to the Cartesian components of the dipole transition moments \vec{E}_{01} and $\text{Im}[\vec{M}_{01}]$ of the modes $1E$, $2E$ and A_2 of the $\Lambda - \delta\delta\delta\cdots 2\text{Cl}^-$ complex, and for comparison, also of the mode 101 of the free $\Lambda - \delta\delta\delta$, which is an E mode (that is representative for the modes of the free molecule). As can be seen, the modes of E symmetry ($1E$, $2E$ and 101) have electric dipole transition moments (EDTM) and magnetic dipole transition moments (MDTM) with non-zero x and y Cartesian components and zero z components, whereas the mode A_2 has non-zero z components and zero x and y components. This can be qualitatively understood by looking at the schematic representation of the nuclear displacement vectors of the modes $1E$, $2E$ and A_2 in Fig. 6.7. In the E modes a cancelation between the z components of the displacement vectors of the H atoms occurs at each H_{axial} triad. This means that no net displacement of charge in the z direction occurs in the E modes. In the A_2 modes the cancelation occurs for the x and y components of the displacement vectors and as a result no net charge displacement occurs in the xy plane. This is ultimately a consequence of the D_3 symmetry.

Looking at the non-zero components of the dipole transition moments in Table 6.3, we note a clear difference between the free molecule and the chloride complex. In mode 101 of the free molecule the electronic and nuclear components have different sign and as a result they counteract each other. This holds for both the x and y components. We note that since the nuclei and the electrons have opposite electrical charges, this is exactly what one would expect, viz., the displacements of the nuclei induce a displacement of approximately the same amount of negative electronic charge (the nuclei "drag" the electrons along).

For the chloride complex, the situation is different. Counteraction of electronic

Mode		X		Y		Z	
		nuc.	el.	nuc.	el.	nuc.	el.
1E	\vec{E}_{01}	-41.37	-34.85	16.60	13.99	0.00	0.00
	$\text{Im}[\vec{M}_{01}]$	482.68	1780.08	-193.73	-714.51	0.00	0.00
2E	\vec{E}_{01}	9.69	39.15	27.20	109.94	0.00	0.00
	$\text{Im}[\vec{M}_{01}]$	154.48	406.03	433.82	1140.13	0.00	0.00
A ₂	\vec{E}_{01}	0.00	0.00	0.00	0.00	-290.20	-266.74
	$\text{Im}[\vec{M}_{01}]$	0.00	0.00	0.00	0.00	-53.12	148.76
101 of FM (E mode)	\vec{E}_{01}	-32.93	21.46	-44.42	28.95	0.00	0.00
	$\text{Im}[\vec{M}_{01}]$	506.96	-293.38	683.91	-395.81	0.00	0.00

Table 6.3: Cartesian components of the nuclear (*nuc.*) and electronic (*el.*) contributions of the electric (\vec{E}_{01}) and magnetic ($\text{Im}[\vec{M}_{01}]$) transition dipole moments for the modes 1E, 2E and A₂ of the chloride complex and mode 101 of the free molecule (an E mode). Units: $E_{01}(10^{-22}\text{esu}\cdot\text{cm})$, $M_{01}(10^{-24}\text{esu}\cdot\text{cm})$.

and nuclear contributions is no longer observed. In all cases but one (the *z* component of $\text{Im}[\vec{M}_{01}]$ in the A₂ mode of the chloride complex) the electronic and nuclear contributions to a Cartesian component have the same sign. Thus, in the chloride complex, the nuclear and electronic components reinforce each other rather than counteracting each other as they do in the free molecule. As a result, the total electric and magnetic dipole transition moments of the complex are much larger than the ones of the free molecule. Since the IR and VCD intensities are determined by the two dipole transition moments, via Eqs. (6.1) and (6.2), respectively, it is clear that both intensities are significantly enhanced upon complexation.

A very simple and intuitive physical explanation can be given for the effects of the complexation described above. When the H atoms move towards the Cl⁻ ions, the increasing transfer of charge from the chloride ions into the N–H bonds is an opposite movement of negative electronic charge that counteracts the effects of the electrons dragged along by the displaced protons. Thus, depending on the amount of charge that flows into the N–H bonds, the total electronic contributions of the electric dipole transition moments (EDTM) either have much smaller magnitudes and therefore are unable to counteract the nuclear contributions anymore, or change sign and therefore will reinforce the nuclear parts. In both cases the magnitudes of the total EDTM are significantly increased as a consequence of the charge transfer in the chloride complex (due to the suppression of the cancellation of nuclear and electronic parts). Furthermore, since the electric and magnetic phenomena are intimately related, a sign change of the electronic contribution of the EDTM will induce a sign change of the electronic contribution of the (perpendicular) magnetic dipole transition moment (MDTM).

Symmetry constraints on the EDTM and MDTM and the magnitude of IR/VCD intensity

The displacement of the H_{axial} atoms, as well as the counteracting charge transfer, are in all modes mostly in the positive or negative z direction. Thus, it is to be expected that the resulting EDTMs will have very large z components (much larger than the x and y components). Furthermore, these large z components of the EDTMs will induce very large MDTMs in the xy plane (the plane perpendicular to the z direction). That is, the x and y components of the MDTMs are expected to be much larger than the z component.

Due to cancelations dictated by symmetry, the close relation between electric and magnetic phenomena cannot be traced per mode in Table 6.3. In the E modes, since the z components of the total EDTMs are zero (by symmetry), no net charge displacements along z that can influence the x and y components of the MDTMs are visible. In the A_2 mode the effects of the z charge displacements on the x and y components of the MDTM are equally invisible, since these components (of the total MDTMs) are also zero by symmetry.

In order to shed additional light on the overall picture deduced from Table 6.3, in the following we will investigate the atomic contributions of the total electric and magnetic dipole transition moments of the modes $2E$ and A_2 . The mode $1E$ is not considered since it is very similar to the mode $2E$. Furthermore, since in the $N \leftrightarrow H \cdots Cl$ modes the effects of the charge transfer are most notable for the six H atoms involved in the complex bond to the Cl^- , and since these atoms have the largest displacement vectors, we single out the contributions of these H atoms for special consideration.

Tables 6.4 and 6.5 show the nuclear and electronic contributions of the atomic EDTMs (upper panels) and MDTMs (lower panels) of these six H atoms for the normal modes $2E$ and A_2 , respectively. The summed contributions of all other atoms as well as the total transition dipole moments are also given.

Considering first the A_2 mode (Table 6.4), we note that the nuclear z components of the atomic EDTMs are much larger than the nuclear x and y components. This is in keeping with the predominantly z directed nuclear motions in this mode. The electronic z components are much reduced due to the counteracting charge transfer motion of the electronic charge, although they still have different sign compared to the nuclear z components. The sum over all 6 H's of +47.10 of the electronic z components is much smaller than the -576.30 of the nuclear z components. Combined with the contributions of all the other atoms, which are numerically not negligible, but do have roughly equal nuclear and electronic parts of opposite sign, the nuclear and electronic sum totals are both of the same sign

Atomic, \vec{E}_{01}^λ , and total, \vec{E}_{01} , Electric Dipole Transition Moments of Mode A_2 .							
Atom	$ \vec{E}_{01}^\lambda $	X		Y		Z	
		nuc	el	nuc	el	nuc	el
H ₂₆	96.02	-29.84	1.86	-7.71	-17.91	-96.05	7.85
H ₃₀	96.02	8.24	-16.44	29.70	7.34	-96.05	7.85
H ₃₄	96.02	21.60	14.58	-21.99	10.56	-96.05	7.85
H ₂₈	96.02	-8.24	16.44	29.70	7.34	-96.05	7.85
H ₃₂	96.02	29.84	-1.86	-7.71	-17.91	-96.05	7.85
H ₃₆	96.02	-21.60	-14.58	-21.99	10.56	-96.05	7.85
6 H's		0.00	0.00	0.00	0.00	-576.30	+47.10
other atoms		0.00	0.00	0.00	0.00	+286.10	-313.84
						-290.20	-266.74
total \vec{E}_{01}	556.94	0.00		0.00		-556.94	

Atomic, $\text{Im}[\vec{M}_{10}^\lambda]$, and total, $\text{Im}[\vec{M}_{10}]$, Magnetic Dipole Transition Moments of Mode A_2 .							
Atom	$ \text{Im}[\vec{M}_{10}^\lambda] $	X		Y		Z	
		nuc	el	nuc	el	nuc	el
H ₂₆	658.08	171.36	247.74	-302.64	-204.71	-28.94	32.96
H ₃₀	658.06	-347.77	-301.15	2.92	-112.18	-28.94	32.96
H ₃₄	658.06	176.41	53.41	299.72	316.90	-28.95	32.96
H ₂₈	658.06	347.77	301.15	2.92	-112.18	-28.94	32.96
H ₃₂	658.08	-171.36	-247.74	-302.64	-204.71	-28.94	32.96
H ₃₆	658.06	-176.41	-53.41	299.72	316.90	-28.95	32.96
6 H's		0.00	0.00	0.00	0.00	-173.64	+197.76
other atoms		0.00	0.00	0.00	0.00	+120.52	-49.00
						-53.12	+148.76
total $\text{Im}[\vec{M}_{10}]$	95.64	0.00		0.00		95.64	

Table 6.4: Normal mode A_2 . The length and the Cartesian components of the nuclear (*nuc*) and electronic (*el*) contributions of the atomic EDTMs, \vec{E}_{01}^λ (upper panel), and MDTMs, $\text{Im}[\vec{M}_{10}^\lambda]$ (lower panel), of the hydrogen atoms involved in the inter-molecular bond. Contributions of all other atoms as well as the total EDTMs and MDTMs (\vec{E}_{01} and $\text{Im}[\vec{M}_{10}]$) are also given. Units: $\vec{E}_{01}, \vec{E}_{01}^\lambda$ (10^{-22} esu·cm), $\text{Im}[\vec{M}_{01}], \text{Im}[\vec{M}_{10}^\lambda]$ (10^{-24} esu·cm).

(negative) and add up to a large negative EDTM.

The x and y components of the atomic EDTMs of the A_2 mode are relatively small. The counteracting effect of the charge transfer on the electronic parts is often (though not always) visible for individual atoms, but the x and y EDTM components add up to zero by symmetry anyway. The atomic x and y EDTM components are too small to induce any changes in the perpendicular (z) atomic MDTMs. As a result the atomic z components of the MDTMs are relatively small and have nuclear and electronic parts of different sign and similar magnitude which add up to a small total contribution of the six H atoms (see lower panel of Table 6.4). This makes the contribution from the other atoms to the z component of the MDTM of the A_2 mode equally important.

We note that the lack of significant influence of the charge transfer in the complex bond on the MDTM z component of A_2 explains the phenomenon ob-

served earlier in Table 6.3. That is, the electronic and nuclear z components of the MDTM of mode A_2 have opposite signs and counteract each other. However, it should also be noted that the perpendicular x and y atomic MDTMs of the six H atoms *are* affected by the large z component of the EDTMs, i.e. the electronic and nuclear parts have the same sign in almost all cases (the only exception involves a very small nuclear y component of 2.92). These x and y components of the atomic MDTM are large (compared to the z components), in agreement with the predominant motion of the charges in the z direction, but since they sum up to zero, there is no effect on the rotational strength. This explains the magnitudes of the IR and VCD intensities of the mode A_2 . The very large IR intensity (see Table 6.1) arises from the square of the large z component of \vec{E}_{01} . The VCD intensity on the other hand is determined by the inner product of $(E_{01})_z$ and $(M_{10})_z$, and although it is enhanced, it is still moderate due the relatively small $(M_{10})_z$.

For the $2E$ mode the picture is rather similar, only the various Cartesian components play different roles. In keeping with the predominantly z -directed motion of the atoms in this mode, the z components of the individual atomic EDTMs are relatively large (compared to the x and y components). Again, as with the A_2 mode, in response to the charge transfer caused by the complexation of the chloride ions, the electronic parts of the z components have much smaller magnitudes than their nuclear counterparts, and although the two components still have opposite signs the electronic contributions are unable to counteract the nuclear ones. Thus, the magnitudes of the z components of the atomic EDTMs of the $2E$ mode have increased significantly compared to the free molecule. However, since in the $2E$ mode the contributions to the z component from the various atoms cancel, no overall large z component of the total EDTM is obtained, in contrast to the A_2 mode.

Even though the z component of the total EDTM is zero, the charge transfer effect is still important for the $2E$ mode since the large net z components of the atomic EDTMs are mirrored in large perpendicular (x and y) atomic MDTM components. The charge transfer effect shows up in that the nuclear and electronic parts of the atomic MDTMs have mostly the same sign and as a result the x and y components of the total MDTM are large (see lower panel of Table 6.5).

Turning back to the x and y components of the EDTM, we note that per atom they are smaller than the z components, but they do not cancel when added over the atoms. The nuclear and electronic parts have the same sign for most of the atoms, so they add up. The total x and y EDTM components, although increased, are much smaller than the A_2 z component. Thus, the IR intensity, resulting from the inner product of \vec{E}_{01} with itself is accordingly considerably lower than the

Atomic, \vec{E}_{01}^λ , and total, \vec{E}_{01} , Electric Dipole Transition Moments of Mode $2E$.							
Atom	$ \vec{E}_{01}^\lambda $	X		Y		Z	
		nuc	el	nuc	el	nuc	el
H ₂₆	137.02	41.11	-1.24	7.10	29.26	138.95	-13.00
H ₃₀	62.09	6.61	-11.84	17.64	6.24	-63.02	5.95
H ₃₄	74.93	14.73	13.40	-17.51	8.57	-75.93	7.05
H ₂₈	125.46	-13.22	23.80	35.81	12.45	-127.25	11.93
H ₃₂	110.87	-33.30	1.04	5.83	23.59	112.38	-10.48
H ₃₆	14.60	2.70	2.77	3.44	-1.69	14.87	-1.45
6 H's		+18.63	+27.93	+52.31	+78.42	0.00	0.00
other atoms		-8.94	+11.22	-25.11	+31.52	0.00	0.00
		9.69	39.15	27.20	109.94		
total \vec{E}_{01}	145.58	48.84		137.14		0.00	

Atomic, \vec{M}_{01}^λ , and total, \vec{M}_{01} , Magnetic Dipole Transition Moments of Mode $2E$							
Atom	$ \text{Im}[\vec{M}_{01}^\lambda] $	X		Y		Z	
		nuc	el	nuc	el	nuc	el
H ₂₆	894.80	-222.44	-347.92	412.09	277.34	44.76	-51.14
H ₃₀	405.26	-211.85	-187.72	6.36	-73.96	-20.43	23.36
H ₃₄	489.52	134.21	36.42	218.39	240.41	-24.33	27.78
H ₂₈	819.21	428.49	379.22	12.39	-149.02	-41.04	46.90
H ₃₂	724.12	180.25	281.30	333.48	224.46	36.10	-41.24
H ₃₆	95.10	26.31	6.82	-42.06	-47.09	4.94	-5.66
6 H's		+334.97	+168.12	+940.65	+472.14	0.00	0.00
other atoms		-180.49	+237.91	-506.83	+667.99	0.00	0.00
		154.48	406.03	433.82	1140.13		
total $\text{Im}[\vec{M}_{01}]$	1670.78	560.51		1573.96		0.00	

Table 6.5: Normal mode $2E$. The length and the Cartesian components of the nuclear (*nuc*) and electronic (*el*) contributions of the atomic EDTMs, \vec{E}_{01}^λ (upper panel), and MDTMs, $\text{Im}[\vec{M}_{10}^\lambda]$ (lower panel), of the hydrogen atoms involved in the inter-molecular bond. Contributions of all other atoms as well as the total EDTMs and MDTMs (\vec{E}_{01} and $\text{Im}[\vec{M}_{10}]$) are also given. Units: $\vec{E}_{01}, \vec{E}_{01}^\lambda$ (10^{-22} esu·cm), $\text{Im}[\vec{M}_{01}], \text{Im}[\vec{M}_{10}^\lambda]$ (10^{-24} esu·cm).

A_2 IR intensity (see Table 6.1). The rotational strength, resulting from the inner product of (E_{01}) and (M_{10}), is however large, on account of the large MDTM x and y components and the not negligible EDTM x and y components. We are therefore able to understand both the mechanism of the enhancement of the IR and VCD intensities by the chloride ion complexation, and the relative magnitudes of the IR and VCD intensities of the $2E$ (and similarly $1E$) *versus* A_2 $\text{N} \leftrightarrow \text{H} \cdots \text{Cl}$ modes.

6.4.3 The charge transfer

Charge redistribution during vibrational motion

In this section we investigate the transfer of charge from the associated chloride ions into the N–H bonds induced during the normal mode motion when the H

atoms in the intermolecular bond approach the chloride ions.

As an example, the mode A_2 will be considered. The six H atoms are displaced by 0.05 Å along their nuclear displacement vectors. Then, a single point calculation is done for this unrelaxed geometry. As can be seen from the schematic representation of the mode A_2 in Fig. 6.7, the hydrogens H_{28} , H_{32} and H_{36} are displaced towards the Cl_{38}^- ion, whereas the hydrogens H_{26} , H_{30} and H_{34} are displaced away from the Cl_{39}^- . We note that the displacement considered (0.05 Å) is comparable to the amplitude of the vibrational motion

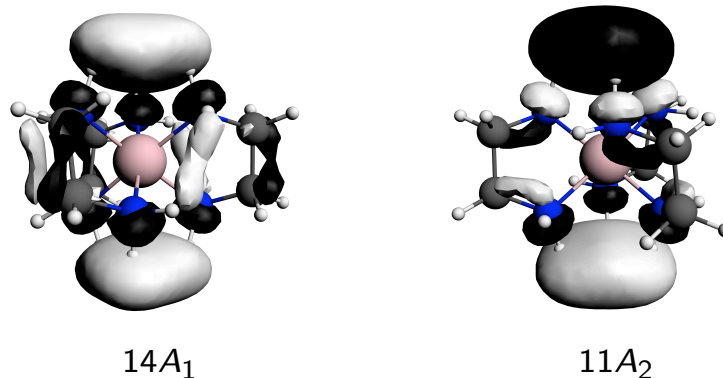
An estimation of the amount of charge transferred as a result of the displacement of the protons can be obtained by comparing the Mulliken charges of the two chloride ions in the equilibrium geometry and in the displaced one. In the equilibrium geometry the Mulliken charge of each chloride ion is -0.5215 electrons. In the displaced geometry the two chlorides have different Mulliken charges, the charge of the Cl_{38} is -0.4730 electrons whereas the charge of the Cl_{39} is -0.5640 electrons. This clearly shows that when the protons approach a Cl^- , charge flows from the ion into the N–H bond, whereas when the protons move away from the Cl^- the reverse happens. The resulting effect is charge transfer over effectively a large distance, from Cl_{38}^- towards Cl_{39}^- . We have verified that the same conclusions are also obtained when looking at the Hirshfeld charges and/or the Voronoi deformation densities (VDD) charges [105] of the two chloride ions.

The changes in charge transfer during the vibrational motion are largely determined by the N–H_{axial} σ^* orbitals. A triad of N–H_{axial} σ^* orbitals can form a totally in-phase combination, e.g. $(1/\sqrt{3})(\sigma_{28}^* + \sigma_{32}^* + \sigma_{36}^*)$ (see atom numbering in Fig. 6.5), which has σ symmetry with respect to the C_3 axis and can form a σ bond with the Cl_{38}^- $3p_z$ orbital. The same three local σ^* orbitals can also form two combinations which have nodal planes passing through the z axis and which can form donor-acceptor π bonds with the Cl_{38}^- $3p_x$ and $3p_y$ orbitals. Of course the σ^* s at the triad of axial N–H groups at the negative z axis can form analogous σ and π combinations, which can interact with the Cl_{39}^- $3p_z$ and $3p_{x,y}$ orbitals, respectively. In the overall D_3 symmetry group these σ and π orbitals at the upper and lower N–H triads form plus and minus symmetry combinations; the σ orbitals for instance form combinations that enter the A_1 and A_2 irreps and interact with the combinations of the axial Cl^- $3p_z$ donor orbitals of the same irrep symmetry. The π orbitals go into the E irrep and interact with E combinations of the $3p_{x,y}$ orbitals at Cl_{38}^- and Cl_{39}^- .

An illustration is given for the σ case. Figure 6.8 displays in the upper panel the virtual orbitals $14A_1$ and $11A_2$ of $\Lambda - \delta\delta\delta$ at equilibrium geometry, and in the lower panel the corresponding orbitals ($66A$ and $67A$) of $\Lambda - \delta\delta\delta$ with displaced hydrogens. These orbitals are clearly formed locally from in phase combinations

Virtual MOs

Equilibrium Geometry



Displaced geometry

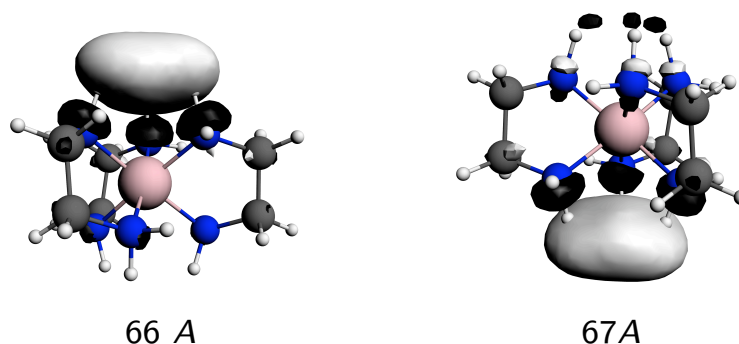


Figure 6.8: The shape of the virtual σ MOs that play an important role in the charge transfer phenomenon.

of the N-H_{axial} σ^* orbitals at an H_{axial} triad, so that lobes with large amplitude towards the Cl⁻ ions are created.

Upon displacement of the six H atoms, a localization of the orbitals occurs. The (localized) virtual orbitals 66A and 67A of $\Lambda - \delta\delta\delta$ with displaced hydrogens are in phase and out of phase, respectively, combinations of the virtual orbitals 14A₁ and 11A₂. The 14A₁ and 11A₂ orbitals are close in energy and can easily be mixed by perturbations such as the H displacements. As can be seen in Fig. 6.8, orbital 66A (the out of phase combination) is localized on the upper three N-H

bonds that have been stretched, and it will overlap with chloride ion Cl_{38}^- , whereas orbital 67A (the in phase combination) is localized mostly on the downside H's of the three N-H bonds that have been shortened, and will overlap with chloride ion Cl_{39}^- . The stretching of the upper N-H bonds will cause a lower energy of orbital 66A, and better overlap with Cl_{38}^- since its amplitude towards the Cl_{38}^- is somewhat extended, while the shortening of the lower N-H bonds will raise the energy of 67A and its slight shrinking will lower the overlap with Cl_{39}^- . This means that more charge will be donated by the chloride Cl_{38}^- into the virtual orbital 66A, whereas less charge will be donated by the chloride Cl_{39}^- into 67A. Precisely the same effects operate in the π symmetry. This explains the effects on the Cl^- charges of the H displacements in the vibrational motion that we noted above.

Contributions from the occupied MOs to the AATs and APTs

In order to further substantiate that the observed large effect of complexation on the intensities of the N-H_{axial} modes originates from charge transfer, we will show in this section that the observed effects on the electronic contributions to the EDTMs and MDTMs can be traced back to the role of the Cl^- 3p donor orbitals. The electronic contributions of both atomic tensors (APT and AAT) can be decomposed into contributions from the occupied molecular orbitals, see Eqs. (3.10) and (3.13). We have monitored how the electronic contributions of the atomic tensors (APT and AAT) of the H atoms in the intermolecular bond and their MO contributions change when going from the free molecule to the chloride complex. We have found that in most of the cases when a tensor component has significantly different values in the free molecule and in the complex, the contributions from the 8 occupied Cl^- valence orbitals of the complex (3s and 3p orbitals) have relatively large magnitudes. To substantiate this remark, in the following we will discuss the case of two tensor components (xz and zx) of the AAT of the hydrogen H_{28} in Fig. 6.5 (the tensor is not symmetrical). In the zx tensor component the contributions from the 8 Cl^- based occupied MOs have large magnitudes, whereas for the xz tensor component they are almost zero. We note that we have analyzed the MO contributions of all the tensor components of both APTs and AATs, however, for brevity and due to the qualitative nature of the analysis we shall discuss here only two representative examples.

Figures 6.9 show the contributions from all occupied MOs to the tensor components I_{xz}^{28} and I_{zx}^{28} , respectively. The vertical axis indicates the magnitude of the MO contributions, $I_{\alpha\beta}^{28}(J_{occ})$, while the horizontal axis indicates the occupied MOs (J_{occ}). The (mainly) Cl^- orbitals, which have no counterparts in the free

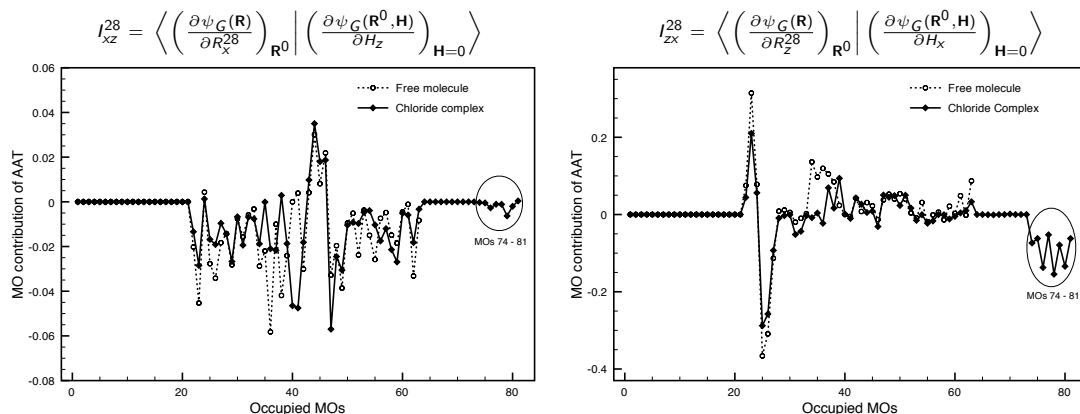


Figure 6.9: Contribution from the occupied MOs to the electronic components of the atomic axial tensor (AAT). Comparison between MOs contributions in the free molecule (dotted line) and in the chloride complex (continuous line) for the tensor components I_{xz}^{28} (upper panel) and I_{zx}^{28} (lower panel) of the AAT of atom H_{28} . The mostly Cl^- orbitals have been assemble to the right (MOs 64-81), the rest of the orbitals are ordered according to increasing orbital energy. The units are $a.u.$.

molecule, have been assembled to the right (orbitals 64-81). The orbitals 64-73 are core orbitals of Cl^- , whereas the orbitals 74-81 are the $3s$, $3p$ orbitals of Cl^- . The rest of the occupied orbitals (1-63) are orbitals of the bare $\Lambda - \delta\delta\delta$.

The tensor component I_{xz}^{28} has similar values in the complex ($-0.559 a.u.$) and in the free molecule ($-0.629 a.u.$), and as can be seen in Fig. 6.9 (left panel) the contributions of the last 8 occupied MOs are almost zero (note the different vertical scale of the left and right panels of Fig. 6.9). The tensor component I_{zx}^{28} , on the other hand, has very different values in the complex ($-0.789 a.u.$) and in the free molecule ($+0.7097 a.u.$), and as can be seen in Fig. 6.9 (right panel) the contributions due to the last 8 occupied MOs have significant magnitudes and mainly determine this difference. Since this correlation with significant Cl^- orbital contributions can be made for almost all tensor components that show substantial changes, we conclude that the occupied Cl^- valence orbitals i.e. MOs 74-81, play a key role in the changes observed in the H_{axial} atomic tensors, hence in the total electric and magnetic transition dipoles and therefore in the enhancement mechanism. This is in complete accord with the role of charge transfer out of these Cl^- orbitals we have inferred earlier. Thus, we conclude that the analysis of the MO contributions to the atomic tensors presented in this section quantifies the charge transfer effects and demonstrates explicitly the direct involvement of the chloride occupied valence orbitals in the enhancement of the IR and VCD

intensities via an electronic mechanism.

6.5 Summary and Conclusions

In this chapter we have investigated the enhancement of the IR and VCD intensities of the N–H stretching modes of $[\text{Co}(\text{en})_3]^{3+}$ induced by the association of the chloride ions. We have shown that due to the charge transfer from the chloride ions into the N–H bond, the electronic parts of both the electric and magnetic dipole vibrational transition moments often change sign. As a result the nuclear and electronic parts reinforce each other (normally they counteract each other) which results in enhancement of the intensities.

We note that since the charge transfer affects both the electric and magnetic dipole transition moments (EDTM and MDTM), the mechanisms responsible for the enhancement of the IR and VCD intensities are related. However, as the discussion of the A_2 and $2E$ $\text{N} \leftrightarrow \text{H} \cdots \text{Cl}$ modes showed, the effects may show up in different Cartesian components of the EDTM and the MDTM. Large z directed charge flow affects the z component of the EDTM, and if that is not zero by symmetry, there is a large effect on the IR intensity, as in the A_2 mode. But since this charge flow does not increase the z component of the MDTM, the inner product of EDTM and MDTM (consisting only of the product of the z components) shows a moderate effect, hence moderate enhancement of the VCD intensity. The perpendicular (x and y) MDTM components are related to z charge flow, and in the E modes in which these x and y components are nonzero, the large x and y MDTM components cause a relatively large VCD intensity.

Our analysis has provided a simple and intuitive overall physical picture of the mechanism responsible for the enhancement of both IR and VCD intensities, clearly explaining the origin of very large enhancements (up to 3 orders of magnitude [79, 80]), which have been known for a long time in the case of IR intensities.

We have also shown the N–H stretching modes ($\text{N} \leftrightarrow \text{H} \cdots \text{Cl}$) are robust modes (as defined in the chapters 4 and 5) [78], with values of the angle ξ (made by their electric and magnetic dipole transition moments) that differ far from 90° , being either 0° or 180° . This is a consequence of the D_3 symmetry. As a result their signs are accurately predicted by calculations, and therefore good agreement is expected between calculations and experiments. The comparisons between the calculated (OLYP/TZP and B3LYP/LanL2DZ) VCD spectrum of the $[\text{Co}(\text{en})_3]^{3+} \cdots 2\text{Cl}^-$ in the $\Lambda - \delta\delta\delta$ conformation and the experimental spectrum of $[\text{Co}(\text{en})_3]^{3+}$ measured in excess of chloride ions (taken from reference [55])

showed that this is indeed the case.

We have applied the analysis of the APTs and AATs in terms of contributions from the occupied molecular orbitals we have introduced in chapter 4 [78]. This has helped to identify the charge transfer from the Cl^- orbitals as the cause of the intensity enhancements we have considered in this paper. Such an analysis should be more widely applicable, and for instance also provide insight into other electronic effects that affect the VCD spectra, such as the effects induced by d-electron configuration of a central metal ion [84, 106, 107].

Chapter 7

Summary and Conclusions

Determination of the absolute configuration (AC) of chiral molecules is of utmost importance in the pharmaceutical industry since the enantiomers of chiral drugs can have completely different biological and pharmacological properties (e.g. while one enantiomer has the desired pharmacological activity, the other one may be less active, inactive, or even toxic).

Vibrational Circular Dichroism spectroscopy is a powerful tool for determination of AC. In VCD spectroscopy the AC of a compound is determined based on a comparison of its experimental and calculated spectra. Thus, in order to have reliable VCD predictions, it is imperative to understand the differences between the experimental and calculated VCD spectra, and the mechanisms that induce these changes.

This thesis deals with the various aspects related to the calculation and interpretation of VCD spectra.

Chapter 1

Chapter 1 gives a brief introduction of chirality and optical activity phenomena. After summarizing the implication of chirality in chemistry, biology and pharmaceutical industry, a short overview of the chiroptical spectroscopic techniques with emphasis on VCD is given.

Chapter 2

In *Chapter 2* the theory of vibrational circular dichroism is presented. After deriving a general quantum mechanical expression for rotational strength, i.e. the quantity that determines the circular dichroism intensities, the properties of rotational strength are discussed. Then, the expression for rotational strength is

cast into a form implementable in computer programs, i.e. Stephens' equations for VCD, by making successive approximations.

Chapter 3

Chapter 3 describes the implementation of Stephens' equations for VCD in the Amsterdam Density Functional (ADF) program package and the validation of our implementation.

Analytical derivatives techniques have been employed for the calculation of APTs, AATs and harmonic force fields (HFF). Slater-type orbitals have been used for the calculation of APTs and HFF, whereas STO based London-atomic orbitals, the so called GIAO (gauge included atomic orbitals), have been used for the calculation of the AATs.

One complication encountered during the implementation process was the dependence of the AATs on the occupied–occupied (occ–occ) block of the $U^{(1),R_{\lambda\alpha}}$ and $U^{(1),H_{\beta}}$ matrices, i.e. the derivatives of the eigenvectors of the unperturbed Kohn-Sham equations with respect to a nuclear displacement and a magnetic field, respectively. For degenerate orbitals, the denominator of the occ–occ off-diagonal matrix elements of both $U^{(1),R_{\lambda\alpha}}$ and $U^{(1),H_{\beta}}$ matrices will diverge causing numerical problems. However, as demonstrated in section 3.2.5, the contributions from these off-diagonal matrix elements of the occ–occ blocks can be expressed in terms of the perturbed overlap matrices thereby avoiding any complication.

The validation of the implementation was done in two steps. First, we have verified the internal consistency of the code by investigating 1) the degree of origin independence of our calculated rotational strengths, and 2) to what extent the APTs and AATs sum rules are satisfied. Thus, we have shown that 1) the common origin gauge and the distributed origins gauge yield practical identical AATs, which proves that our implementation yields rotational strengths that are origin independent [20], and 2) the sum rules for the AATs and APTs convergence to a stable limit as the size of the basis set is increased and are practically satisfied when using the large ET-pVQZ basis set, which is a good approximation of the basis set limit.

Then, we have shown that our implementation yields VCD spectra that reproduce very well the experimental VCD spectra. Using α -pinene and Troger's base as test molecules, we have tested the performance of various combinations of functionals and basis sets by comparing our calculated VCD spectra to experimental VCD spectra. We found that the BP86 and OLYP functionals in combination with TZP basis set yield VCD spectra that are in very good agree-

ment with experiments. The good agreement obtained between calculated and experimental spectra is the ultimate proof for the usefulness and correctness of the code.

Finally, we have also compared our BP86 and OLYP VCD spectra to the VCD spectra obtained with the hybrid functionals B3LYP and B3PW91 which are the most popular exchange–correlation functionals for VCD calculations. As shown, the non-hybrid functionals, i.e. BP86 and OLYP, have yielded frequencies and rotational strengths that are at least as good as the ones calculated with hybrid functionals.

Chapter 4

In *Chapter 4* the effects induced by complex formation in VCD spectra have been investigated. Formation of molecular complexes between solute and solvent molecules is the most important interaction that affects the experimental VCD spectra measured in solution. Therefore, to correctly interpret the differences between gas phase calculations and experimental VCD spectra measured in solutions, it is crucial to identify and understand the mechanisms that induce changes in VCD spectra upon complex formation.

Using benzoyl-benzoic acid (BBA) hydrogen bonded to the achiral NH_3 as an example, 6 types of differences have been encountered when comparing the VCD spectrum of free BBA to the VCD spectrum of BBA-NH_3 , i.e. very small changes in the rotational strengths of solute modes (case **A**), changes of sign of rotational strengths (case **B**), changes in magnitude (case **C**), non-zero rotational strengths for modes of the achiral solvent (“transfer of chirality”, case **D**), large frequency shifts accompanied by giant enhancements of the IR and VCD intensities of modes involved in hydrogen bonding (case **E**), and emergence of new peaks (case **F**).

By monitoring the changes of the APTs, AATs, and normal modes, when going from the free molecule (BBA) to the molecular complex (BBA-NH_3) we have been able to understand all these differences. The results of our detailed analysis have highlighted the role played by the angles ξ between the electric and magnetic dipole transition moments, and clearly showed how knowledge of the values of the angles ξ of the modes in the VCD spectrum can aid the interpretation of the VCD spectra. Thus, based on the value of its angle ξ a normal mode can be classified as *robust* or *non-robust*. Robust modes have angles ξ that are far from 90° . The sign of the rotational strength of a robust modes can be trusted since it is not easily affected by the small perturbation present in experiment. Non-robust modes, on the other hand, have angles ξ that are close to 90° . The sign of the rotational strength of a non-robust mode should not be trusted since

it can be affected even by small perturbations. Clearly, only robust modes should be considered for determining the AC using VCD.

Chapter 5

In *Chapter 5* we have investigated further the concept of *robust modes* introduced in Chapter 4. Using a test group of 27 molecules, ranging from small (5 atoms) to relatively large (44 atoms) molecules, and computational parameters that are known to yield converged APTs, AATs and normal mode frequencies, we have investigated 1) the distribution of the values taken by the angles ξ , and 2) the dependence of the distributions of the values taken by the ξ angle on the exchange-correlation functional used in the calculation (BP86 vs. OLYP). We have found that in order to be classified as *robust* a normal mode should have significantly large electric and magnetic dipole transition moments, i.e. intense VCD signal, and an angle ξ that differs from 90° by at least 30° .

Further, we have also shown that due to constraints imposed by symmetry on the orientations of the electric and magnetic dipole transition moments, chiral molecules that have symmetry have many normal modes with angles ξ that are far from 90° (e.g. 0° or 180°). As a result, it is to be expected that under normal conditions chiral molecules with symmetry have many robust modes and therefore a better agreement between calculation and experiment should be obtained for them in comparison to molecules without symmetry.

Chapter 6

In *Chapter 6* we have investigated further the mechanism responsible for the giant enhancements of the IR and VCD intensities of modes involved in hydrogen bonding. Using tris(ethylenediaminato)cobalt(III) complex with two associated chloride ions along the C_3 symmetry axes as an example, we have first investigated the enhancement mechanism by looking at the nuclear and electronic components of the total and atomic electric and magnetic dipole transition moments. This analysis has highlighted 1) the close relation between electric and magnetic phenomena, and 2) the constraints imposed by symmetry on the orientation of the electric and magnetic dipole transition moments and their consequences for the magnitudes of the IR and VCD intensities, which increased greatly our understanding of the enhancement mechanism.

Then, we have analyzed in detail the donor-acceptor interactions between the $3p_z$ orbitals of the Cl^- associated ions (as donor) and the σ^* molecular orbital localized on the $\text{N-H}_{\text{axial}}$ bonds (the bonds involved in the intermolecular hydro-

gen bonds). We have shown that upon stretching of the N-H_{axial} bonds, charge flows from the the 3p_z chloride orbitals into the N-H_{axial} bonds.

Finally, by looking at the contributions to the atomic tensors (AATs and APTs) from occupied MOs, we have shown that the observed sign change of the electronic components of the electric and magnetic dipole transition moments is a direct consequence of the charge transfer phenomena. We have found that in most of the cases when the tensor components of the APTs and AATs of the hydrogen atoms involved in the intermolecular bond have significantly different values in the free molecule and in the complex (which also correlates to the sign changes of the electronic components), the components to the total AATs and APTs associated to the 8 occupied chloride valence orbitals of the complex (3s and 3p orbitals) have significantly large magnitudes.

The results of our analysis are consistent with the following simple physical picture of the enhancement mechanisms: the transfer of charge induced upon elongation of the N-H_{axial} bond counteracts the movement of negative electronic charge dragged along by the motion of the H nuclei. Depending on the amount of charge that flows into the N-H_{axial} bonds, the total electronic contributions of the electric dipole transition moments either have much smaller magnitudes and therefore are unable to counteract the nuclear contributions anymore, or change sign and therefore will reinforce the nuclear parts. Since the electric and magnetic phenomena are intimately related, a sign change of the electronic contribution of the electric dipole transition moment will induce a sign change of the electronic contribution of the (perpendicular) magnetic dipole transition moment. As a result, the nuclear and electronic components of both dipole transition moments will reinforce each other in the complex. This clearly explains the large enhancements observed for the IR and VCD intensities. The very good agreement obtained between the experimental and calculated (OLYP/TZP) VCD spectra has validated further the conclusions of this study.

Samenvatting

Het bepalen van de absolute configuratie (AC) van chirale moleculen is van uiterst belang in de farmaceutische industrie, omdat de enantiomeren van chirale medicijnen compleet verschillende biologische en farmaceutische eigenschappen kunnen hebben. (Bijv. de ene enantiomeer kan de gewenste farmaceutische eigenschap hebben, terwijl de ander deze in mindere mate heeft, niet, of zelfs giftig is.)

Vibratieel circulair dichroïsme (VCD) is een krachtige techniek om de AC te bepalen. Met VCD spectroscopie wordt de AC van een stof bepaald door berekende spectra te vergelijken met spectra verkregen uit het experiment. Daarom is het belangrijk voor betrouwbare VCD voorspellingen om de verschillen tussen de berekende en experimentele spectra en de mechanismen die deze verschillen veroorzaken te begrijpen.

Dit proefschrift behandelt de uiteenlopende aspecten van het berekenen en het interpreteren van VCD spectra.

Hoofdstuk 1

Hoofdstuk 1 geeft een korte introductie in chiraliteit en optisch activiteit. Na een samenvatting van de gevolgen van chiraliteit in scheikunde, biologie en de farmaceutische industrie, wordt een kort overzicht gegeven over spectroscopische technieken voor chiraliteit met nadruk op VCD.

Hoofdstuk 2

In *Hoofdstuk 2* wordt de theorie van vibratieel circulair dichroïsme gepresenteerd. Na het afleiden van een algemene quantum mechanische uitdrukking voor de rotatiesterkte, i.e. de grootte die de circulair dichroïsme-intensiteiten bepaald, worden de eigenschappen van de rotatiesterkte besproken. Vervolgens wordt de uitdrukking voor de rotatiesterkte herschreven tot een vorm die implementeerbaar is in computerprogramma's, i.e. de zogenaamde Stephens' vergelijkingen voor VCD, door het maken van opeenvolgende benaderingen.

Hoofdstuk 3

Hoofdstuk 3 beschrijft de implementatie van Stephens' vergelijkingen voor VCD in het Amsterdam Density Functional (ADF) programma pakket en de validatie van onze implementatie.

Analytische afgeleiden zijn gebruikt om de atomaire polaire tensoren (APTs), de atomaire axiaaltensoren (AATs) en het harmonische krachtenveld te berekenen. Slaterorbitalen (STOs) zijn gebruikt voor de berekening van de APTs en het harmonische krachtenveld. De op de STOs gebaseerde Londonorbitalen, de zogenaamde GIAOs (geijkte atoom orbitalen), zijn gebruikt voor de berekening van de AATs.

Een van de problemen tijdens de implementatie was dat de AATs afhankelijk waren van het bezette-bezette blok van de $U^{(1),R_{\lambda\alpha}}$ en de $U^{(1),H_{\beta}}$ matrices, i.e. de afgeleiden van de eigenvectoren van de ongestoorde Kohn-Sham vergelijkingen naar de kernverplaatsing en het magnetisch veld respectievelijk. Voor ontaarde orbitalen zorgt de divergentie van de noemer in de bez-bez niet-diagonale matrix elementen van zowel de $U^{(1),R_{\lambda\alpha}}$ als de $U^{(1),H_{\beta}}$ matrices voor numerieke problemen. Echter, zoals in sectie 3.2.5 aangetoond, kunnen de bijdragen van deze niet-diagonale matrix elementen van het bez-bez blok uitgedrukt worden in termen van de gestoorde overlap matrices, waarmee complicaties vermeden worden.

De validatie van de implementatie bestond uit twee stappen. Eerst werd de interne consistentie van de code gecontroleerd door 1) de onafhankelijkheid van de berekende rotatiesterkten met betrekking tot de keuze van de oorsprong te testen en 2) te kijken in welke mate de APTs en AATs aan de somregels voldoen. We hebben laten zien dat 1) een andere keuze van de oorsprong dan de gebruikelijke bijna dezelfde AATs oplevert, wat aantoont dat onze implementatie oorsprong onafhankelijke rotatiesterktes geeft, en 2) de somregels voor de AATs en APTs naar een stabiele limiet convergeren met het vergroten van de basisset en ze bijna kloppen als een grote ET-pVQZ basisset gebruikt wordt, welke een goede benadering is voor de basisset limiet.

Vervolgens hebben we laten zien dat onze implementatie VCD spectra geeft die zeer goed de experimentele VCD spectra reproduceren. Met behulp van α -pinene en Trogers base als testmoleculen hebben we een aantal combinaties van functionalen en basissets getest door onze berekende VCD spectra te vergelijken met experimentele spectra. We hebben ontdekt dat de BP86 en OLYP functionalen in combinatie met de TZP basisset VCD spectra geven die goed overeenkomen met de experimenten. De goede overeenkomst tussen de berekende en experimentele spectra is het ultieme bewijs voor een correcte en bruikbare

code.

Tenslotte hebben we onze BP86 en OLYP VCD spectra met de VCD spectra vergeleken, die verkregen zijn met de hybride functionalen B3LYP en B3PW91, welke de meest populaire uitwissel-correlatie functionalen voor VCD berekeningen zijn. De niet-hybride functionalen BP86 en OLYP gaven frequenties en rotatiesterktes die minstens zo goed zijn als die met hybride functionalen berekend zijn.

Hoofdstuk 4

In *Hoofdstuk 4* zijn de effecten die door complexvorming veroorzaakt worden onderzocht. Het vormen van moleculaire complexen van de opgeloste en de oplosmiddel moleculen is de belangrijkste interactie die de in oplossing gemeten experimentele VCD spectra beïnvloedt. Daarom is het, voor het goed interpreteren van de verschillen tussen de gasfase berekeningen en de in oplossing gemeten experimentele VCD spectra, cruciaal om de mechanismen te identificeren en te begrijpen die de verschillen in de VCD spectra induceren als complexen gevormd worden.

Met behulp van het benzoyl-benzoëzuur (BBA) waterstofgebonden met het achirale NH_3 als voorbeeld waren er zes type verschillen bij het vergelijken van het VCD spectrum van vrij BBA met het VCD spectrum van BBA-NH_3 : zeer kleine verschillen in de rotatiesterktes van het oplosmolecuul (geval **A**), het veranderen van teken van de rotatiesterktes (geval **B**), verandering in de grootte (geval **C**), eindige rotatiesterktes voor vibraties van het achirale oplosmolecuul (“overdracht van chiraliteit”, geval **D**), grote frequentie verschuivingen in combinatie met gigantische versterking van infrarood (IR) en VCD intensiteiten van vibraties van de waterstofbinding (geval **E**) en het ontstaan van nieuwe pieken (geval **F**).

Door het bestuderen van de veranderingen in de APTs, AATs en normaalvibraties van het moleculaire complex (BBA-NH_3) ten opzichte van het vrije molecuul (BBA) hebben we al deze verschillen kunnen begrijpen. De resultaten van onze gedetailleerde analyse hebben de rol van de hoeken ξ tussen de elektrische en magnetische overgangsdipool benadrukt en lieten duidelijk zien hoe kennis van de waarden van de hoeken ξ van de vibraties in het VCD spectrum kan helpen bij de interpretatie van het VCD spectrum. Het blijkt dat gebaseerd op de waarde van de hoek ξ van een normaalvibratie, deze geclassificeerd kan worden als *robust* of *niet-robust*. Robuuste vibraties hebben een hoek ξ ver van 90° . Het teken van de rotatiesterkte van een robuuste vibratie is betrouwbaar, omdat het niet makkelijk verstoord wordt door de kleine storingen in het experiment. Niet

robuuste vibraties echter, hebben een hoek ξ in de buurt van 90° . Het teken van de rotatiesterkte van een niet-robuuste vibratie is niet betrouwbaar, aangezien het teken veranderd kan worden door kleine storingen. Het is duidelijk dat enkel de robuuste vibraties gebruikt moeten worden om de AC met behulp van VCD te bepalen.

Hoofdstuk 5

In *Hoofdstuk 5* hebben we het concept *robuuste vibraties* geïntroduceerd in *Hoofdstuk 4* verder bestudeerd. Met behulp van een testgroep van 27 moleculen met kleine tot relatief grote moleculen (5 t/m 44 atomen) en numerieke parameters waarvan bekend is dat ze geconvergeerde APTs, AATS en normaalvibraties geven, hebben we 1) de spreiding van de waarden van de hoek ξ en 2) de afhankelijkheid ten opzichte van de uitwissel-correlatie functionaal (BP86 vs. OLYP) bestudeerd. We hebben ontdekt dat voor de classificatie als *robuust* een normaalvibratie een grote elektrische en magnetische overgangsdipool moet hebben, i.e. een intens VCD signaal, en een hoek ξ die meer dan 30° verschilt van 90° .

Verder hebben we laten zien dat door de condities opgelegd door de symmetrie op de oriëntaties van de elektrische en magnetische overgangsdipolen, symmetrische chirale moleculen veel normaalvibraties hebben met hoeken ξ ver van 90° (bijv. 0° of 180°). Daarom is het te verwachten dat onder normale condities symmetrische chirale moleculen veel robuuste vibraties hebben en dus kan een betere overeenkomst tussen de berekening en het experiment worden verwacht ten opzichte van niet-symmetrische moleculen.

Hoofdstuk 6

In *Hoofdstuk 6* hebben we het mechanisme dat de gigantische versterkingen van de IR en VCD intensiteiten voor vibraties van waterstofbindingen veroorzaakt verder bestudeerd. Met behulp van het tris(ethylenediaminato)cobalt(III) complex met twee chloride ionen langs de C_3 symmetrie as als voorbeeld hebben we eerst het versterkingsmechanisme onderzocht door te kijken naar de nucleaire en elektronische componenten van het totale en de atomaire elektrische en magnetische overgangsdipolen. Deze analyse heeft 1) de sterke relatie tussen elektrische en magnetische fenomenen en 2) de restricties opgelegd door symmetrie op de oriëntatie van de elektrische en magnetische overgangsdipolen en hun effecten op de groottes van de IR en VCD intensiteiten benadrukt, wat ons begrip van het versterkingsmechanisme sterk vergroot heeft.

Vervolgens hebben we de donor-acceptor interacties tussen de $3p_z$ orbitalen

van Cl^- ionen (als donor) en de σ^* moleculaire orbitalen (MOs) gelocaliseerd op de $\text{N-H}_{\text{axiaal}}$ binding (de bindingen die deelnemen aan de waterstofbinding) in detail geanalyseerd. We hebben laten zien dat door het oprekken van de $\text{N-H}_{\text{axiaal}}$ bindingen lading van de $3p_z$ chloride orbitalen in de $\text{N-H}_{\text{axiaal}}$ bindingen vloeit.

Uiteindelijk door te kijken naar de bijdragen aan de atomaire tensoren (AATs en APTs) van de bezette MOs hebben we laten zien dat de geobserveerde tekenwissel van de elektronische componenten van de elektrische en magnetische overgangsdipolen direct het gevolg zijn van het ladingstransportfenomeen. We hebben ontdekt dat in de meeste gevallen de bijdragen aan de atomaire tensoren van de acht bezette chloride valentie orbitalen van het complex ($3s$ en $3p$ orbitalen) bijzonder groot zijn, als de tensor componenten van de APTs en de AATs van de waterstof atomen betrokken bij de intermoleculaire binding significant andere waarden hebben in het vrije molecuul dan in het complex (welke ook correleren met de tekenveranderingen van de elektronische componenten).

Het resultaat van onze analyse is consistent met het volgende simpele natuurkundige idee van het versterkingsmechanisme: de geïnduceerde overdracht van lading door de verlenging van de $\text{N-H}_{\text{axiaal}}$ binding compenseert de beweging van de negatieve lading meegetrokken door de H kernen. Afhankelijk van de hoeveelheid lading die in de $\text{N-H}_{\text{axiaal}}$ bindingen vloeit, worden de totale elektronische bijdragen van de elektrische overgangsdipool veel kleiner en kunnen de nucleaire bijdragen dus niet meer compenseren, of deze zullen van teken veranderen en het nucleaire gedeelte dus versterken. Omdat elektrische en magnetische fenomenen sterk met elkaar verbonden zijn, zal een tekenverandering in de elektronische bijdrage van de elektrische overgangsdipool, een tekenverandering in de elektronische bijdrage van de (loodrechte) magnetische overgangsdipool induceren. Daardoor zullen de nucleaire en elektronische componenten van beide overgangsdipolen elkaar versterken in het complex. Dit is een duidelijke verklaring voor de grote versterkingen waargenomen in de IR en VCD intensiteiten. De goede overeenkomst tussen de experimentele en berekende (OLYP/TZP) VCD spectra versterken de conclusies van dit onderzoek.

References

- [1] Immanuel Kant. *Prolegomena zu einer jeden künftigen Metaphysik die als Wissenschaft wird auftreten können*. For an english translation see : Immanuel kant's prolegomena to any future metaphysics (b. logan) ed.
- [2] A. F. Möbius. *Der barycentrische Calcul (The Calculus of Centers of Gravity)*. J. Ambrosius Barth Verlag, Leipzig, 1827.
- [3] J.M. Bijvoet, A.F. Peerdeman, A.J. van Bommel. Determination of absolute configuration of optical active compounds by means of x-rays. *Nature*, **168 (4268)** (1951) 271–272.
- [4] C W. Deutsche, A. J. Moscovitz. Optical Activity of Vibrational Origin. I. A Model Helical Polymer. *J. Chem. Phys.*, **49** (1968) 3257–3272.
- [5] C W. Deutsche, A. J. Moscovitz. Optical Activity of Vibrational Origin. II. Consequences of Polymer Conformation. *J. Chem. Phys.*, **53** (1970) 2630–2644.
- [6] G. Holzwarth, I. Chabay. Optical Activity of Vibrational Transitions: A Coupled Oscillator Mode. *J. Chem. Phys.*, **57** (1972) 1632–1635.
- [7] J. A. Schellman. Vibrational optical activity. *J. Chem. Phys.*, **58** (1973) 2882.
- [8] J. A. Schellman. Vibrational optical activity. *J. Chem. Phys.*, **60** (1973) 343.
- [9] E. C. Hsu, Holzwarth G. Vibrational circular dichroism observed in crystalline α -NiSO₄·6H₂O and α -ZnSeO₄·6H₂O between 1900 and 5000 cm⁻¹. *J. Chem. Phys.*, **59** (1973) 4678–4685.
- [10] G. Holzwarth, E. C. Hsu, H. S. Mosher, T. R. Faulkner, A. Moscovit. Infrared circular dichroism of carbon-hydrogen and carbon-deuterium stretching modes. Observations. *J. Am. Chem. Soc.*, **96** (1974) 251–252.

- [11] Cheng J. C., Nafie L. A., Stephens P. J. Polarization scrambling using photo elastic modulator: application to circular dichroism measurements. *J. Opt. Soc. Am.*, **65** (1975) 1031–1035.
- [12] Nafie L. A., Diem M. Theory of High-Frequency Differential Interferometry - Application to the Measurement of Infrared Circular and Linear Dichroism via Fourier-Transform Spectroscopy. *Soc. Applied Spectroscopy*, **33** (1979) 130–135.
- [13] P. J. Stephens. Theory of Vibrational Circular Dichroism. *J. Phys. Chem.*, **89** (1985) 748–752.
- [14] J. R. Cheesman, M. J. Frisch, F. J. Devlin, P. J. Stephens. Ab initio calculation of atomic axial tensors and vibrational rotational strengths using density functional theory. *Chem. Phys. Lett.*, **252** (1996) 211–220.
- [15] Peter Atkins, Roland Friedman. *Molecular Quantum Mechanics*. Oxford University Press, 4th ed., 2005.
- [16] P.L. Polavarapu. *Vibrational spectra: principles and applications with emphasis on optical activity*. Elsevier, Amsterdam, Lausanne, New York, Shannon, Singapore, Tokyo, 1st ed., 1998.
- [17] L.D. Barron. *Molecular light scattering and optical activity*. Cambridge University Press, Cambridge, New York, 2nd ed., 2004.
- [18] Ira N. Levine. *Molecular spectroscopy*. John Wiley and Sons, New York, London, Sydney, Toronto, 1st ed., 1975.
- [19] T. Thirunamachandran D.P. Craig. *Molecular quantum electrodynamics : an introduction to radiation-molecule interaction*. Dover Publications, Inc., Mineola, New York, 1st ed., 1998.
- [20] P. J. Stephens. Gauge Dependence of Magnetic Dipole Transition Moments and Rotational Strength. *J. Phys. Chem.*, **91** (1987) 1712–1715.
- [21] Albert Messiah. *Quantum Mechanics*. Dover Publications, Inc., New York, London, Sydney, Toronto, 2nd ed., 1975.
- [22] E. B. Wilson, Jr. J. C. Decius, P. C. Cross. *Molecular Vibration*. Dover Publication Inc. New York, Mineola, New York, 2001.

- [23] A. D. Buckingham, P. W. Fowler, P. A. Galwas. Velocity-Dependent Property Surfaces and the Theory of Vibrational Circular Dichroism. *Chemical Physics*, **112** (1987) 1–14.
- [24] Amsterdam Density Functional program. Theoretical Chemistry, Vrije Universiteit, Amsterdam. URL: <http://www.scm.com>.
- [25] G. Te Velde, F. M. Bickelhaupt, E. J. Baerends, C. Fonseca Guerra, S. J. A. Van Gisbergen, J. G. Snijders, T. Ziegler. Chemistry with ADF. *J. Comput. Chem.*, **22** (9) (2001) 931–967.
- [26] C. Fonseca Guerra, J.G. Snijders, G. te Velde, E.J. Baerends. Towards an order-N DFT method. *Theor Chem Acc*, **99** (1998) 391–403.
- [27] P. M. Boerrigter, G. te Velde, E. J. Baerends. Three-dimensional numerical integration for electronic structure calculations. *Int. J. Quant. Chem.*, **33** (1988) 87–113.
- [28] G. te Velde, E. J. Baerends. Numerical Integration for Polyatomic Systems. *J. Comp. Phys.*, **99** (1992) 84–98.
- [29] R. Ditchfield. Self-consistent perturbation theory of diamagnetism. Gauge-invariant LCAO method for NMR chemical shifts. *Mol. Phys.*, **27** (1974) 789–807.
- [30] F. London. The quantic theory of inter-atomic currents in aromatic combinations. *J. Phys. Radium*, **8** (1937) 397–409.
- [31] R. D. Amos, N. C. Handy, K. J. Jalkanen, P. J. Stephens. Efficient calculation of Vibrational Magnetic Dipole Transition Moments and Rotational Strength. *Chem. Phys. Lett.*, **133** (1987) 21–26.
- [32] J. Gerratt, I. Mills. Force Constants and Dipole Moment Derivatives of Molecules from Perturbed Hartree-Fock Calculations. I. *J. Chem. Phys.*, **49** (1968) 1719–1729.
- [33] J. A. Pople, R. Krishnan, H. B. Schlegel, J. S. Binkley. Derivative Studies in Hartree-Fock and Møller-Plesset Theories. *Int. J. Quant. Chem.: Quant. Chem. Symp.*, **13** (1979) 225–241.
- [34] R. J. McWeeny. *Methods of Molecular Quantum Mechanics*. Academic Press, New York, 2nd ed., 1964.

-
- [35] G. Schreckenbach, T. Ziegler. Calculation of NMR Shielding Tensors Using Gauge-Including Atomic Orbitals and Modern Density Functional Theory. *J. Phys. Chem.*, **99** (1995) 606–611.
- [36] K. L. Bak, P. Jorgensen, T. Helgaker, K. Ruud, H. Jorgen, Aa. Jensen. Gauge-origin independent multiconfigurational self-consistent theory for vibrational circular dichroism. *J. Chem. Phys.*, **98** (1993) 8873–8887.
- [37] Stephen K. Wolff. Analytical Second Derivatives in the Amsterdam Density Functional Package. *Int. J. Quant. Chem.*, **104** (2005) 645–659.
- [38] A. D. Becke. Density-functional exchange-energy approximation with correct asymptotic behavior. *Phys. Rev. A*, **38** (1988) 3098–3100.
- [39] J. P. Perdew. Density-functional approximation for the correlation energy of the inhomogeneous electron gas. *Phys. rev. B*, **33** (1986) 8822–8824.
- [40] N. C. Handy, A. J. Cohen. Left-right correlation energy. *Mol. Phys.*, **99** (2001) 403–412.
- [41] F. A. Hamprecht, A. J. Cohen, N. C Handy. Development and assessment of new exchange-correlation functionals. *J. Chem. Phys.*, **109** (1988) 6264–6271.
- [42] C. Lee, W. Yang, R. G. Parr. Development of the Colle-Salvetti correlation-energy formula into a functional of the electron density. *Phys. Rev. B*, **37** (1988) 785–789.
- [43] E. van Lenthe, E.J. Baerends. Optimized Slater-Type Basis Sets for Elements 1-118. *J. Comput. Chem.*, **24** (2003) 1142–1156.
- [44] Marcel Swart, F. Matthias Bickelhaupt. QUILD: QUantum-regions interconnected by local descriptions. *J. Comput. Chem*, **29:5** (2007) 724–734.
- [45] K. J. Jalkanen, R. W. Kawiecki, P. J. Stephens, R. D. Amos. Basis set and Gauge Dependence of ab Initio Calculations of Vibrational Circular Strengths. *J. Phys. Chem.*, **94** (1990) 7040–7055.
- [46] K. J. Jalkanen, P. J. Stephens, R. D. Amos, N. C. Handy. Gauge Dependence of Vibrational Rotational Strength: NHDT. *J. Phys. Chem.*, **92** (1988) 1781–1785.

- [47] P. J. Stephens, K. J. Jalkanen, R. D. Amos, P. Lazzeretti, R. Zanasi. Ab initio Calculations of Atomic Polar and Axial Tensors for HF, H₂O, NH₃ and CH₄. *J. Phys. Chem.*, **94** (1990) 1811–1830.
- [48] Danya Yang, Arvi Rauk. Vibrational circular dichroism intensities: Ab initio vibronic coupling theory using the distributed origin gauge. *J. Chem. Phys.*, **97** (1992) 6517–6534.
- [49] P. J. Stephens, C. S. Ashvar, F. J. Devlin, J. R. Cheesman, M. J. Frisch. Ab initio calculation of atomic axial tensors and vibrational rotational strengths using density functional theory. *Mol. Phys.*, **89** (1996) 579–594.
- [50] F. J. Devlin, P. J. Stephens, J. R. Cheesman, M. J. Frisch. Ab Initio Prediction of Vibrational Absorption and Circular Dichroism Spectra of Chiral Natural Products Using Density Functional Theory: α -Pinene. *J. Phys. Chem. A*, **101** (1997) 9912–9924.
- [51] Johannes Neugebauer, Bernd A. Hess. Fundamental Vibrational Frequencies of Small Polyatomic Molecules from Density Functional Calculations and Vibrational Perturbation Theory. *J. Chem. Phys.*, **118** (2003) 7215–7225.
- [52] M. Reiher, J. Neugebauer, Bernd A. Hess. Quantum chemical calculation of Raman intensities for large molecules: The photoisomerization of $[\{\text{Fe}(\text{S}_4)(\text{PR}_3)_2\}(\text{N}_2\text{H}_2)]$ ($\text{S}_4^{2-} = 1,2\text{-bis}(2\text{-mercaptophenylthio)ethane(2-)}$). *Z. Physik. Chem.*, **217** (2003) 91–103.
- [53] Johannes Neugebauer, Evert Jan Baerends, Evgeny V. Efremov, Freek Ariese, Cees Gooijer. Combined Theoretical and Experimental Deep-UV Resonance Raman Studies of Substituted Pyrenes. *J. Phys. Chem. A*, **109** (2005) 2100–2106.
- [54] A. Aamouche, F. J. Devlin, P. J. Stephens. Structure, Vibrational Absorption and Circular Dichroism Spectra, and Absolute Configuration of Troger's Base. *J. Am. Chem. Soc.*, **122** (2000) 2346–2354.
- [55] T.B. Freedman, X. Cao, D. A. Young, L. A. Nafie. Density Functional Theory Calculations of Vibrational Circular Dichroism in Transition Metal Complexes: Identification of Solution Conformations and Mode of Chloride Ion Association for (+)-Tris(ethylenediaminato)cobalt(III). *J. Phys. Chem. A*, **106** (2002) 3560–3565.

- [56] T. Kuppens, J. P. Tollenaere W. Langenaeker, P. Bultinck. Determination of the Stereochemistry of 3-Hydroxymethyl-2,3-dihydro-[1.4]dioxino[2,3-b]-pyridine by Vibrational Circular Dichroism and the Effect of DFT Integration Grid. *J. Phys. Chem. A*, **107** (2003) 542–553.
- [57] P. J. Stephens, F. J. Devlin. Determination of the Structure of Chiral Molecules Using Ab Initio Vibrational Circular Dichroism Spectroscopy. *Chirality*, **12** (2000) 172–179.
- [58] F. J. Devlin, P.J. Stephens, J. R. Cheeseman, M. J. Frisch. Ab Initio Prediction of Vibrational Absorption and Circular Dichroism Spectra of Chiral Natural Products Using Density Functional Theory: Camphor and Fenofone. *J. Phys. Chem. A*, **101** (1997) 6311–6333.
- [59] F. Wang, P. L. Polavarapu, V. Schurug, R. Schmidt. Absolute configuration and Conformational Analysis of a Degradation Product of Inhalation Anesthetic Sevoflurane: A Vibrational Circular Dichroism Study. *Chirality*, **14** (2002) 618–624.
- [60] T. B. Freedman, X. Cao, R. K. Dukor, Nafie L. A. Nafie. Absolute Configuration Determination in Solution State Using Vibrational Circular Dichroism. *Chirality*, **15** (2003) 734–758.
- [61] K. J. Jalkanen, S. Suhai. N-Acetyl-L-alanine N'-methylamide: a density functional analysis of the vibrational absorption and vibrational circular dichroism spectra. *Chemical Physics*, **208(1)** (1996) 81–116.
- [62] F. Wang, P.L. Polavarapu. Vibrational circular dichroism, predominant conformations, and hydrogen bonding in (s)-(-)-3-butyn-2-ol. *J. Phys. Chem. A*, **104(9)** (2000) 1822–1826.
- [63] Thomas Bürgi, Angelo Vargas, Alfons Baiker. VCD spectroscopy of chiral cinchona modifiers used in heterogeneous enantioselective hydrogenation: conformation and binding of non-chiral acids. *J. Chem. Soc., Perkin Trans. 2*, (2002) 1596–1601.
- [64] Joanna E. Rode, Jan Cz. Dobrowolski. Chiral allenes: theoretical VCD and IR spectra. *J. Mol. Struct. (Theochem)*, **635 (1-3)** (2003) 151–159.
- [65] Chira Cappelli, Susanna Monti, Antonio Rizzo. Effect of the Environment on Vibrational Infrared and Circular Dichroism Spectra of (S)-Proline. *Int. J. Quant. Chem.*, **104** (2005) 744–757.

- [66] Jiangtao He, Prasad L. Polavarapu. Determination of Intermolecular Hydrogen Bonded Conformers of *r*-Aryloxypropanoic Acids Using Density Functional Theory Predictions of Vibrational Absorption and Vibrational Circular Dichroism Spectra. *J. Chem. Theory Comput.*, **1** (2005) 506–514.
- [67] T. Kuppens, W. Herrebout, B. van der Veken, , P. Bultinck. Intermolecular Association of Tetrahydrofuran-2-carboxylic Acid in Solution: A Vibrational Circular Dichroism Study. *J. Phys. Chem. A*, **110** (2006) 10191–10200.
- [68] T. B. Freedman, X. Cao, L. M. Phillips, P. T. W. Cheng, R. Dalterio, Y.-Z. Shu, H. Zhang, N. Zhao, R. B. Shukla, A. Tymiak, S. K. Gozo, L. A. Nafie, J. Z. Gougoutas. Determination of the Absolute Configuration and Solution Conformation of a Novel Disubstituted Pyrrolidine Acid A by Vibrational Circular Dichroism. *Chirality*, **18** (2006) 746–753.
- [69] V Würtz Jürgensen, K Jalkanen. The VA, VCD, Raman and ROA spectra of tri-L-serine in aqueous solution. *Phys. Biol.*, **3** (2006) S63–S79.
- [70] J. E. Rode J. Sadlej, J. C. Dobrowolski, M. H. Jamrz. DFT study of vibrational circular dichroism spectra of D-lactic acidwater complexes. *Phys. Chem. Chem. Phys.*, **8** (2006) 101–113.
- [71] P. Zhang, P. L. Polavarapu. Spectroscopic Investigation of the Structures of Dialkyl Tartrates and Their Cyclodextrin Complexes. *J. Phys. Chem. A*, **111** (2007) 858–871.
- [72] Martin Losada, Yunjie Xu. Chirality transfer through hydrogen-bonding: Experimental and ab initio analyses of vibrational circular dichroism spectra of methyl lactate in water. *Phys. Chem. Chem. Phys.*, **9** (2007) 3127–3135.
- [73] Wenqi Suna, Jian Wua, Bin Zhenga, Yongjun Zhub, Chengbu Liu. DFT study of vibrational circular dichroism spectra of (S)-glycidolwater complexes. *J. Mol. Struct. (Theochem)*, **809** (1–3) (2007) 161–169.
- [74] W.-G. Han, K.J. Jalkanen, M. Elstner, S. Suhai. Theoretical study of aqueous n-acetyl-L-alanine n'-methyleamide: Structures and raman, vcd, and roa spectra. *J. Phys. Chem. B*, **102**(14) (1998) 2587–2602.
- [75] J. Jalkanen, I. M. Degtyarenko, R. M. Nieminen, X. Cao, L. A. Nafie, F. Zhu, L. D. Barron. Role of hydration in determining the structure and

- vibrational spectra of L-alanine and N-acetyl L-alanine N'-methyleamide in aqueous solution: a combined theoretical and experimental approach. *Theor. Chem. Account.*, **119** (2008) 191–210.
- [76] Shunsuke Takenaka, Keizo Kondo, Niichiro Tokura. Induced circular dichroism. Part III. Chiroptical properties and ionpair equilibria in 2-benzoylbenzoic acidamphetamine. *J. Chem. Soc., Perkin Trans. 2*, (1975) 1520–1524.
- [77] J. Neugebauer, E. J. Baerends. Exploring the Ability of Frozen-Density Embedding to Model Induced Circular Dichroism. *J. Phys. Chem. A*, **110** (28) (2006) 8786–8796.
- [78] V. P. Nicu, J. Neugebauer, E. J. Baerends. Effects of Complex Formation on Vibrational Circular Dichroism Spectra. *J. Phys. Chem. A*, **112** (30) (2008) 6978–6991.
- [79] G. C. Pimentel, A. L. McClellan. *The Hydrogen Bond*, W. H. Freeman and Company, San Francisco and London. W. H. Freeman and Company, San Francisco and London, 1st ed., 1960.
- [80] ed. Mansel Davies. *Infra-red spectroscopy and Molecular structure*. Elsevier Publishing Company, Amsterdam - London - New York, 1st ed., 1983.
- [81] F. J. Devlin, P. J. Stephens, J. R. Cheeseman, M. J. Frisch. Prediction of vibrational circular dichroism spectra using density functional theory: Camphor and fenchone. *J. Am. Chem. Soc.*, **118** (1996) 6327–6328.
- [82] P. J. Stephens, F. J. Devlin, S. Schürch, J. Hulliger. Determination of the absolute configuration of chiral molecules via density functional theory calculations of vibrational circular dichroism and optical rotation: The chiral alkane D₃-anti-trans-anti-trans-anti-trans-perhydrotriphenylene. *Theor. Chem. Acc.*, **119** (1-3) (2008) 19–28.
- [83] V. P. Nicu, J. Neugebauer, S. K. Wolff, E. J. Baerends. A vibrational circular dichroism implementation within a Slater-type-orbital based density functional framework and its application to hexa- and hepta-helices. *Theor. Chem. Acc.*, **119** (1-3) (2008) 245–263.
- [84] Daryl A. Young, Teresa B. Freedman, Elmer D. Lipp, Laurence A. Nafie. Vibrational Circular Dichroism in Transition-Metal Complexes. 2. Ion Association, Ring Conformation, and Ring Currents of Ethylenediamine Ligands. *J. Am. Chem. Soc.*, **108** (1986) 7255–7263.

- [85] F. Wang, P.L. Polavarapu. Vibrational circular dichroism: Predominant conformations and intermolecular interactions in (r)-(-)-2-butanol. *J. Phys. Chem. A*, **104** (2000) 10683–10687.
- [86] C. Cappelli, S. Corni, B. Mennucci, R. Cammi, J. Tomasi. Vibrational circular dichroism within the polarizable continuum model: A theoretical evidence of conformation effects and hydrogen bonding for (s)-(-)-3-butyn-2-ol in ccl4 solution. *J. Phys. Chem. A*, **106** (2002) 12331–12339.
- [87] S. Shin, M. Nakata, Y. Hamada. Analysis of vibrational circular dichroism spectra of (s)-(+)-2-overlineDelta xi by rotational strengths expressed in local symmetry coordinates. *J. Phys. Chem. A*, **110** (2006) 2122–2129.
- [88] Prasad L. Polavarapu. Why is it Important to Simultaneously Use More Than One Chiroptical Spectroscopic Method for Determining the Structures of Chiral Molecules? *Chirality*, **20** (2008) 664–672.
- [89] A. Klamt, G. Schüürmann. COSMO: a new approach to dielectric screening in solvents with explicit expressions for the screening energy and its gradient. *J. Chem. Soc., Perkin Trans. 2*, 1993) 799 – 805.
- [90] P. J. Stephens, F. J. Devlin, C. F. Chabalowski, M. J. Frisch. Ab Initio Calculation of Vibrational Absorption and Circular Dichroism Spectra Using Density Functional Force Fields. *J. Phys. Chem.*, **98** (1994) 11623–11627.
- [91] C. S. Ashvar, F. J. Devlin, K. L. Bak, P. R. Taylor, P. J. Stephens. Ab Initio Calculation of Vibrational Absorption and Circular Dichroism Spectra: 6,8-Dioxabicyclo[3.2.1]octane. *J. Phys. Chem.*, **100** (1996) 9262–9270.
- [92] T. Eggimann, R. A. Shaw, H. Wieser. Measurements and model calculations of vibrational circular dichroism spectrum of 6, 8-dioxabicyclo[3.2.1]octane. *J. Phys. Chem*, **95** (1991) 591–598.
- [93] P. Bour, J. Sopkov, L. Bednrov, Petr Malonn, T. A. Keiderling. Transfer of molecular property tensors in cartesian coordinates: A new algorithm for simulation of vibrational spectra. *J. Comput. Chem.*, **18** (1997) 646–659.
- [94] K. Nakatsu, Y. Saito, H. Kuroya. Studies on crystals of metallic tris-ethylenediamine-complexes 1. The crystal structure of DL-tris-ethylenediamine-Cobalt(III) chloride trihydrate [CO EN3]CL3. 3H2O. *Bull. Chem. Soc. Jpn.*, **29** (1956) 428–434.

- [95] Y. Saito, K. Nakatsu, M. Shiro, H. Kuroya. Studies on crystals of metallic tris-ethylenediamine-complexes 3. The Determination of the absolute configuration of optically active complex ion, $[\text{Co}(\text{en})_3]^{3+}$, by means of X-rays. *Bull. Chem. Soc. Jpn.*, **30**: (1957) 795.
- [96] H. L. Smith, B. E. Douglas. Effects of electrolytes on circular dichroism curves of cationic complex ions. *Inorg. Chem.*, **5** (1966) 784.
- [97] S. F. Mason, B. J. Norman. Optical rotatory power of co-ordination compounds .6. Effects of ion-association on circular dichroism spectra of trisdi-amine complexes metal ions. *J. Chem. Soc. A - Inorg. Phys. Theo.*, **3** (1966) 307.
- [98] F.E. Jorge, J. Autschbach, T. Ziegler. On the origin of the optical activity in the d-d transition region of tris-bidentate $\text{Co}(\text{III})$ and $\text{Rh}(\text{III})$ complexes. *Inorg. Chem.*, **42**(26) (2003) 8902–8910.
- [99] F. E. Jorge, J. Autschbach, T. Ziegler. On the origin of optical activity in tris-diamine complexes of $\text{Co}(\text{III})$ and $\text{Rh}(\text{III})$: A simple model based on time-dependent density function theory. *J. Am. Chem. Soc.*, **127**(3) (2005) 975–985.
- [100] L. Jensen, M. Swart, P. T. van Duijnen, J. Autschbach. Circular dichroism spectrum of $[\text{Co}(\text{en})_3]^{3+}$ in water: A discrete solvent reaction field study. *Int. J. Quant. Chem.*, **106** (2006) 24792488.
- [101] J. L. Sudmeier, G. L. Blackmer, C. H. Bradley, F. A. L. Anet. Conformational Analysis of Trisethylenediamine and Tris-R-propylenediamine Complexes of Cobalt (III) by 25 1-MHz Proton Magnetic Resonance with Cobalt-59 Decoupling. *J. Am. Chem. Soc.*, **94** (1972) 757–761.
- [102] C. J. Hawkins, R. M. Peachey. Conformational analysis of coordination compounds .6. PMR study of diamagnetic 5-membered diamine chelate rings. *Aust J. Chem.*, **29** (1976) 33–48.
- [103] C. J. Hawkins, J. A. Palmer. Conformational Analysis of Chelate rings-systems by NMR. *Coord. Chem. Rev.*, **44** (1982) 1–60.
- [104] E. J. Corey, J. C. Bailar Jr. The Stereochemistry of Complex Inorganic Compounds. XXII. Stereospecific Effects in Complex Ions. *J. Am. Chem. Soc.*, **81** (1956) 2620–2629.

-
- [105] Clia Fonseca Guerra, Jan-Willem Handgraaf, Evert Jan Baerends, F. Matthias Bickelhaupt. Voronoi deformation density (VDD) charges: Assessment of the Mulliken, Bader, Hirshfeld, Weinhold, and VDD methods for charge analysis. *J. Comput. Chem.*, **25** (2) (2003) 189–210.
- [106] H. Sato, T. Taniguchi, K. Monde, S. I. Nishimura, A. Yamagishi. Dramatic effects of d-electron configurations on vibrational circular dichroism spectra of tris(acetylacetonato)metal(III). *Chem. Lett.*, **35**:4 (2006) 364–365.
- [107] H. Sato, T. Taniguchi, A. Nakahashi, K. Monde, A. Yamagishi. Effects of central metal ions on vibrational circular dichroism spectra of Tris-(beta-diketonato)metal(III) complexes. *Inorg. Chem.*, **46**:16 (2007) 6755–6766.

Acknowledgements

In this chapter I would like to thank all the people who were involved directly or indirectly in the development of this thesis.

First of all I would like to thank Prof. Dr. Evert Jan Baerends for giving me the opportunity to do a PhD under his supervision. Dear Evert Jan, there are so many things I have to thank you for. You have given me a lot of freedom in my research, when writing papers, or when preparing presentations and posters. This made me very independent and confident in my abilities. At the same time you have always found the time to talk with me and to think on how my results and papers can be improved. I have enjoyed very much our long discussions on Fridays that sometimes lasted till after nine o'clock in the evening. I admire your kindness, your willingness to learn new things, your curiosity, and your desire to understand how things work. I have learned from you that doing science is about understanding how things work and not about publishing as many papers as possible.

Second of all I would like to thank Dr. Johannes Neugebauer for helping me in the beginning of my PhD project. Dear Johannes, thank you very much for all the things you have taught me (too many to be mentioned here), for your friendship, and for being such a nice office mate. Although I have obtained most of the results in this thesis after you left Amsterdam, they are the fruit of what I have learned from you. Seeing you writing a "little program" for every little problem that needed to be solved inspired me to write ToolsVCD, the program I have used to obtain all the results presented in this thesis.

I am very grateful to Dr. Stephen K. Wolff for developing the second derivative (SD) program of ADF that was essential for starting the VCD project. Dear Steve, thank you very much for taking the time to answer all my emails about your SD program, for giving me your write-ups with the theory of the SD and NMR programs, and for your contribution to the *Theor. Chem. Acc.* paper. I am very proud of that paper, it was because of you we were invited to write it.

I am also grateful for the support I got from the SCM team, Dr. Erik van Lenthe, Dr. Alexei Yakovlev, Dr. Olivier Visser, and Dr. Stan van Gisbergen on

various ADF-related matters. Dear Erik, Alexei, and Olivier thank you for your technical assistance. Dear Stan, thank you for your interest in my VCD program and for intermediating various VCD collaborations.

I would like to thank Prof. Dr. Matthias Bickelhaupt for seeing in me a potential candidate for the VCD project and giving my CV to Evert Jan.

Dear Paula, you have always find the time and the patience to help me with the various administrative matters, thank you very much for this.

I would like to thank Dr. Drew McCormack for helping me with various computer-related matters. Dear Drew, thank you for all the Mac and FORTRAN tips you have given me.

I also like to thank the rest of the group for the friendly atmosphere and to acknowledge Johannes Neugebauer, Ivan Infante, Marcello Luppi, Leonardo Bernasconi, Klaas Giesbertz, Pier Philipsen, and Andreas Götz for being great friends. Special thanks to Marcello for making the very nice cover of this thesis, and to Klaas for translating the Summary of the thesis into Dutch.

Many thanks to my Romanian friends in Amsterdam Bogdan (P.), Daniel, Stan, Bebe, Ana, Radu and Marius and to my former colleagues in Bucharest who have also studied in the Netherlands, Ioana, Monica, Vera, Adi, Gabi and Luci. You have all been great friends and made home seemed much closer.

My holidays would not have been the same without my dear friends from Romania Bogdan (M.), Mita, Radu, Dorin, Pingu, Bebe, Sebi and Bogdan (keep on drumming!). I enjoy tremendously spending time with you guys and I am very grateful for having you.

My gratitude goes to my physics teachers from my home town Sibiu A. Ceusianu, Gh. Pupeză, F. Bunău and G. Negrea. I will always remember your physics classes and physics camps. Your enthusiasm and unequalled pedagogical skills have inspired me to further pursue physics. You will always have my deepest admiration.

My further development as a physicist was shaped by Prof. Dr. V. Grecu (University of Bucharest), Prof. Dr. D. Lenstra (Delft University of Technology) and Prof. Dr. H. Linnartz (Vrije Universiteit Amsterdam). I thank you all for everything you have done for me, working with you helped me to gain a better perspective on the various research areas in physics.

Last but not least I would like to thank my mother and my dear wife Elena. Dear mom, thank you very much for all the sacrifices you have done for me and for your unconditional love and support. I could not have got this far without your help, this book is dedicated to you.

My dearest Elena, it is impossible to quantify your contribution to this thesis. After you have come to Amsterdam everything got easier, not because things

suddenly became simpler—they did not, but because we were working together as a team supporting each other to overcome all the difficulties that one might encounter when doing a PhD or when living in a foreign country. This thesis is your achievement as much as it is mine, and like your thesis, is another of many beautiful things we will do together. *Draga mea, te iubesc din toata inima mea!*

Publications

Parts of this thesis have been published previously:

- [1] V. P. Nicu, J Neugebauer, S. K. Wolf, E. J. Baerends. A vibrational circular dichroism implementation within a Slater-type-orbital based density functional framework and its application to hexa- and hepta-helicenes, *Theor. Chem. Acc.* **119** (1-3), 245-263 (2008).

(Chapter 3 of this thesis is based on parts of this paper)

- [2] V. P. Nicu, J Neugebauer, E. J. Baerends. Effects of Complex Formation on Vibrational Circular Dichroism Spectra, *J. Phys. Chem. A* **112** (30), 6978–6991 (2008).

(Chapter 4 of this thesis)

- [3] V. P. Nicu, E. J. Baerends. Robust modes in Vibrational Circular Dichroism Spectra, *Phys. Chem. Chem. Phys.* (2009), in press

(Chapter 5 of this thesis)

- [4] V. P. Nicu, J Autschbach, E. J. Baerends. Enhancement of IR and VCD intensities due to charge transfer, *Phys. Chem. Chem. Phys.* (2009), in press.

(Chapter 6 of this thesis is based on parts of this paper)

Papers in preparation:

- [5] V. P. Nicu, P. Bodis, F. Brouwer, E. J. Baerends, W. J. Buma. Determination of absolute configuration of Quinidine using Vibrational Circular Dichroism.

CURRICULUM VITAE

Valentin Paul Nicu

PERSONAL DETAILS

Date of birth	7th of May, 1977
Place of birth	Sibiu, Romania
Citizenship	Romanian
Marital Status	Married

EDUCATION

since 11/2008	Post Doc at the Theoretical Chemistry Department of Vrije Universiteit Amsterdam, The Netherlands
06/2003–10/2008	PhD studies in Theoretical Chemistry at the Theoretical Chemistry Department of Vrije Universiteit Amsterdam, The Netherlands
10/2001–09/2002	Master studies at the Theoretical Physics Department of Vrije Universiteit Amsterdam, The Netherlands (Erasmus exchange program)
09/1996–06/2001	Physics studies at the University of Bucharest, Bucharest, Romania
09/1992–06/1996	Colegiul Gheorghe Lazar Sibiu (high school), Sibiu, Romania